A numerical modelling study of Port Alfred upwelling along the inshore edge of Agulhas Current

by

Sheveenah Sunnassee Taukoor

Submitted to the University of Cape Town in fulfilment of the requirements

for the degree

Doctor of Philosophy

Supervisors: Dr Pierrick Penven, Prof Isabelle J. Ansorge, co-supervisor: Dr Thulwaneng Mashifane

Department of Oceanography

Faculty of Science

UNIVERSITY OF CAPE TOWN

February 2024

Declaration

I know the meaning of plagiarism and declare that all the work in the document, save for that which is properly acknowledged, is my own. This thesis/dissertation has been submitted to the Turnitin module (or equivalent similarity and originality checking software) and I confirm that my supervisor has seen my report and any concerns revealed by such have been resolved with my supervisor.

Signature of Author: . . . . . .

Cape Town

12 February 2024

This thesis is dedicated to the majestic killer whales
who sometimes visit the Port Alfred upwelling zone.

Abstract

Port Alfred upwelling, located on the southeast African shelf, lies on the inshore edge of a western boundary current, the Agulhas Current. This study addresses the atmospheric and oceanographic forcing mechanisms responsible for these upwelling events through the daily simulations of a CROCO model of a horizontal spatial resolution of ~2.5km from 1993 to 2014. We tested several coastal upwelling indices and we identified 56 upwelling events from the residuals of sea surface temperature and 49 upwelling events through the decomposition of the vertical velocity. To assess the influence of the wind, we measured the alongshore wind stress, wind stress curl and frictional velocity at different temporal scales. Our analysis showed that upwelling during summer was primarily driven by northeasterlies inducing offshore Ekman transport and divergence. In contrast, stronger southwesterlies during winter could cause vertical mixing. To determine the Port Alfred upwelling's driving mechanism during the mean state, we computed the terms of the generalized Ekman pumping equation and found that the advection of momentum contributed to 4.22 m/day of vertical velocity while the viscous flux term contributed partially to 0.5 m/day of vertical velocity. To determine whether the upwelling was driven by oceanographic mesoscale features (Agulhas Current, Natal pulses, Durban eddies, shear edge eddies and coastal trapped waves), we measured the sea surface height, geostrophic velocity, bottom Ekman transport and identified 1.9 large meander events annually from the LACCE current tracker algorithm, 2.2 based on eddy amplitude, 1.5 based on eddy area, and 1.3 based on eddy radius from the PY eddy tracker algorithm. We found that the Agulhas Current was the primary upwelling driver during the mean state, but some individual upwelling events were influenced by cyclonic eddies and coastal trapped waves.

Finally, we conducted 2 combined Empirical Orthogonal Function analysis from (1) sea surface temperature and (2) vertical velocity and identified surface divergence as the most dominant upwelling driver in both combined EOFs while Ekman transport, the presence of cyclonic eddies, the Agulhas Current and coastal trapped waves also counted as contributing factors in stronger and weaker upwelling events. As an overall this study confirms that the Agulhas Current remains the primary upwelling driver during the mean state but through the lens of a different temporal scale (individual case studies and combined EOFs), it is likely that a combination of one or more forcing mechanisms (upwelling favourable winds, cyclonic eddy, Agulhas Current, coastal trapped waves) will trigger an upwelling event. Shedding more light on this topic and its main drivers allows oceanographers to focus more attention on this upwelling in the future and this could reinforce policymakers to consider Port Alfred upwelling region as a future Marine Protected Area.

Resumé

L'upwelling de Port Alfred, situé sur le plateau sud-est africain, se trouve à la limite côtière d'un courant bord ouest, le courant des Aiguilles. Cette étude aborde les mécanismes de forçage atmosphérique et océanographique responsables de ces événements d'upwelling à travers les simulations quotidiennes d'un modèle CROCO d'une résolution spatiale horizontale d'environ 2,5 km de 1993 à 2014. Nous avons testé plusieurs indices d'upwelling côtiers et nous avons identifié 56 événements d'upwelling du résiduels de la température de surface de mer et 49 événements d'upwelling à travers la décomposition de la vitesse verticale. Pour évaluer l'influence du vent, nous avons mesuré la tension du vent, le rotationnel de la tension de vent et la vitesse de friction à différentes échelles temporelles. Notre analyse a montré que les remontées d'eau au cours de l'été étaient principalement provoquées par les vents du nord-est emettant un transport et une divergence d'Ekman au large. En revanche, des vents plus forts du sud-ouest en hiver pourraient provoquer un mélange vertical. Pour déterminer le mécanisme d'upwelling de Port Alfred pendant l'état moyen, nous avons calculé les termes de l'équation de pompage d'Ekman généralisée et avons constaté que l'advection de momentum contribuait à 4,22 m/jour de vitesse verticale tandis que le terme de friction contribuait partiellement à 0,5 m/jour de vitesse verticale. Pour déterminer si l'upwelling était influencé par des caractéristiques océanographiques à méso-échelle (courant des Aiguilles, Natal pulses, tourbillons de Durban, tourbillons de cisaillement et ondes côtières de Kelvin), nous avons mesuré la hauteur de la surface de la mer, la vitesse géostrophique, le transport d'Ekman au fond et identifié 1,9 événements de méandres par an de l'algorithme de detection de courant LACCE, 2,2 basé sur l'amplitude des tourbillons, 1,5 basé sur la zone de tourbillon et 1,3 basé sur le rayon de tourbillon de l'algorithme de detection de tourbillons PY. Nous avons constaté que le courant des Aiguilles était le principal moteur de la remontée d'eau au cours de l'état moyen, mais que certains événements individuels étaient influencés par des tourbillons cycloniques et des ondes côtières de Kelvin.

Enfin, nous avons effectué 2 analyses de méthode décomposition orthogonale aux valeurs propres à partir de (1) la température de surface de mer et (2) la vitesse verticale et nous avons identifié la divergence de surface comme le moteur de remontée d'eau le plus dominant dans les deux EOF combinés. Cependant, le transport d'Ekman, la présence de tourbillons cycloniques, le courant des Aiguilles et les ondes côtières de Kelvin ont également contribué à des événements d'upwelling plus forts et plus faibles. Dans l'ensemble, cette étude confirme que le courant des Aiguilles reste le principal moteur de la remontée d'eau pendant l'état moyen, mais à travers le prisme d'une échelle temporelle différente (études de cas individuelles et EOF combinés), il est probable qu'une combinaison d'un ou plusieurs mécanismes de forçage (vents favorables, tourbillons cycloniques, courant des Aiguilles, ondes côtières de Kelvin) déclencheront un événement d'upwelling. Approfondir sur ce sujet et ses principaux moteurs permettra aux océanographes de concentrer

davantage leur attention sur cet upwelling à l'avenir, ce qui pourrait inciter aux politiciens à considérer la région d'upwelling de Port Alfred comme une future zone marine protégée.

Acknowledgements

ॐ Shree Ganeshaya Namaha

I am deeply thankful to my supervisors. This thesis would not exist if my supervisors were not there for me. Thank you Prof Isabelle Ansorge, I have huge admiration for your remarkable journey, from being a foreign master's student who once sent a letter to UCT, to becoming the head of the Department of Oceanography at UCT. Thanks to your guidance, I've had the opportunity to embark on SA Agulhas expeditions, participate in Seamester, gain lecturing opportunities, attend conferences, and receive funding assistance from SANAP and science faculty, all of which have helped me fulfill my dreams, as well as a massive thank you for being an extremely major strong voice to encourage me and guide me in this Phd journey.

I am immensely fortunate to have had the opportunity to work under the supervision of Dr Pierrick Penven, a true legend in his field. His expertise in numerical modelling and his ability to effortlessly write down equations have not only deepened my understanding but also fuelled my passion for this area of study. Prior to my PhD, I had no experience with numerical models or coding, yet Pierrick's support and guidance have been instrumental every step of the way. Thank you for welcoming me at LOPS, your sense of humour, your invaluable time, the zoom meetings, your help with admin issues your assistance with finding ARTS funding from IRD and EGU conference funding, and for the lunches we shared, during the French lockdown.

I am very grateful to Dr Thulwaneng Mashifane for his patience during zoom meetings and WhatsApp conversations, often in weekends, as he helped me troubleshoot Python codes. His sense of humor and strong support and encouragement have been invaluable to me throughout this journey.

I would also like to thank my CSI members for their support, time and valuable comments: Dr Jennifer Veitch, Prof Juliet Hermes, Dr Tarron Lamont, Dr Issufo Halo. Thank you Dr Serena Illig and the CROCO team for teaching me how to run a croco model, Dr Jennifer Veitch for teaching me how to use the Bakun upwelling index, Dr Juliano Ramanantsoa for helping me with the SST derived upwelling index, Dr Ashwita Chouksey for teaching me how to use the Py Eddy tracker algorithm, Ant_Simi from Github for always replying regarding the eddy tracker algo. Thank you Dr Clement Vic for troubleshooting my python codes when I was stuck in LOPS, Dr Pierre l'Hegaret for chatting to me about EOFs, Cristina Russo for showing me how to use LACCE algorithm through a zoom call, Dr Pauline Tedesco for our chats on CROCO model grids, Dr Serge Tomety for teaching me how to download big ocean datasets, as well as Dr Daneeja Mawren, Dr Laura Braby, Dr Odilon Houdegonto, Dr Moagabo Ragoasha and Dr Laique Djeutchouang for their support. I am also very thankful to the EDSML, IRD, UCT (dept of Oceanography) and French embassy officers for their assistance for my administrative paperwork.

I am very thankful to my cousins/sisters Deepa, Reena, Praveena, Linda and Sheena for always keeping in touch and to my friends Yuvna, Miguel, Dr Leana, Dr Veronique, James, Benita, Viloshna and Diane for their long term friendship.

Thank you to my papa, my mum, my late sister Shanella, my Watson (currently his head on my laptop as I write this), Biscuit, and God/the energy behind this entire multiverse, for being my main pillars in this temporary life's journey. Life is an illusion in our mind but love from parents and children is the most stable and peaceful feeling in this world for me.

And lastly, a simple thought I always remind myself before starting work is how I have evolved from a lineage of great apes and I can possess a temporary consciousness during a snapshot of this multiverse's timeline, evolved enough to form new neural patterns by visualizing currents, eddies, wind patterns in my brain for months. As I study those potential reasons behind the movement of water molecules whose very same hydrogen and oxygen atoms forming the water molecules which have journeyed from a big bang, supernova, travelling through space, reached planet earth, moving into possibly the ancient superoceans such as Mirovia or Panthalassa to finding their way into the south coast of South Africa and moving up to the surface in Port Alfred. It is simply an absolute privilege and joy of this life. I am so happy and proud that I am an oceanographer.

Contents

Acronyms

AGRIF Adaptive Grid Refinement In Fortran

BBL Bottom Boundary Layer

CMEMS Copernicus Marine Environment Monitoring Service

C3S Copernicus Climate Change Service

CCI Climate Change Initiative

CTW Coastal trapped waves

CROCO Coastal and Regional Ocean COmmunity model

EOF Empirical Orthogonal Function

ESA European Space Agency

EUMETSA European Organisation for the Exploitation of Meteorological Satellites

HadIOD Hadley Centre Integrated Ocean Database

PCA Principal Component Analysis

OSTIA Operational SST and Ice Analysis

REMSS Remote Sensing Systems

ROMS Regional Ocean Modeling System

SST Sea surface temperature

Chapter 1: Introduction

1.0 Port Alfred upwelling

The Agulhas region, located off the southeastern coast of Africa, is known for its dynamic oceanic conditions characterized by the Agulhas Current, significant oceanic eddies, and complex interactions between different water masses and diverse marine ecosystems. One of the key features of this region is the presence of significant upwelling phenomena, particularly the Port Alfred upwelling, which plays a crucial role in shaping the coastal environment and supporting marine life.

Based on *in situ* data and remote sensing datasets, the location of the Port Alfred upwelling has been suggested to occur where the continental shelf widens whereby the Agulhas Current flows from East London to Gqeberha along the eastern edges of the Agulhas Bank (Schumann and Brink, 1990). Some studies have shown that it extends up to 300 km upstream, with an average width of about 30 km and a length of 180 km along the current edge. Figure 1.0 shows the location of the Port Alfred upwelling zone (Lutjeharms et al., 2006).

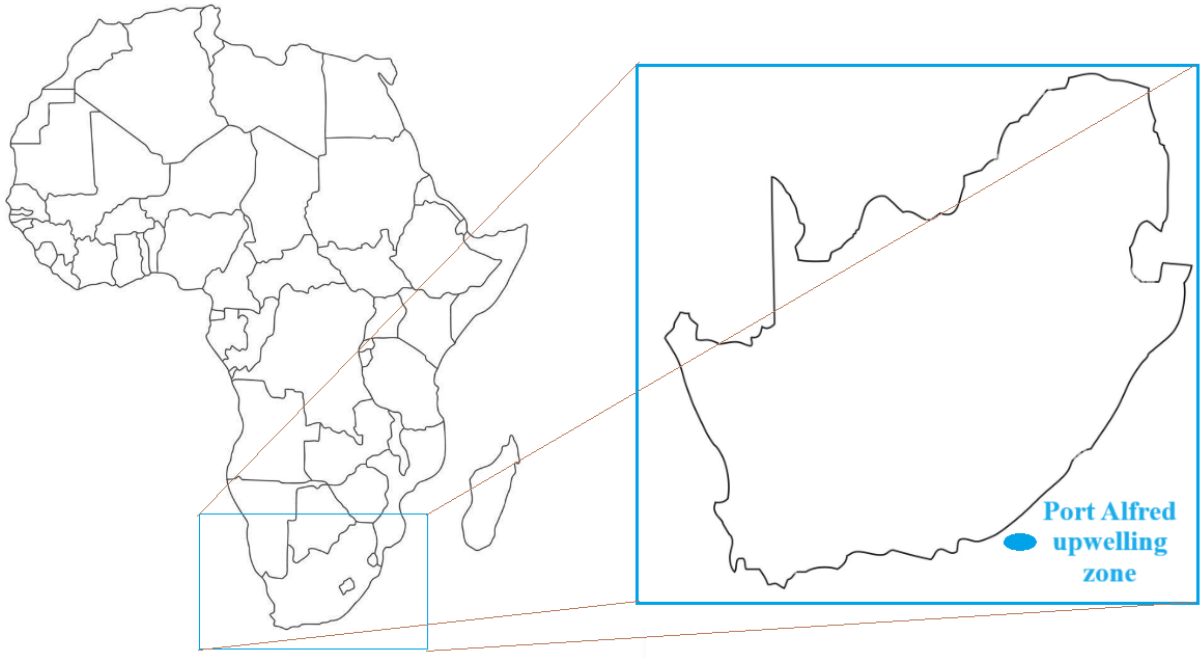

Figure 1.1: Location of Port Alfred upwelling

1.1 Characteristics of the upwelling

The upwelling's surface expression occurs approximately 45% of the time in the vicinity of Port Alfred. During fully developed outcropping events, the surface waters within the upwelling zone are consistently at least 5°C cooler than the adjacent shelf waters over the Agulhas Bank. The upwelling cell is detectable at the sea surface only on an intermittent basis, and the vertical stratification of the region follows a seasonal pattern but can be interrupted by the outcropping of upwelling water.

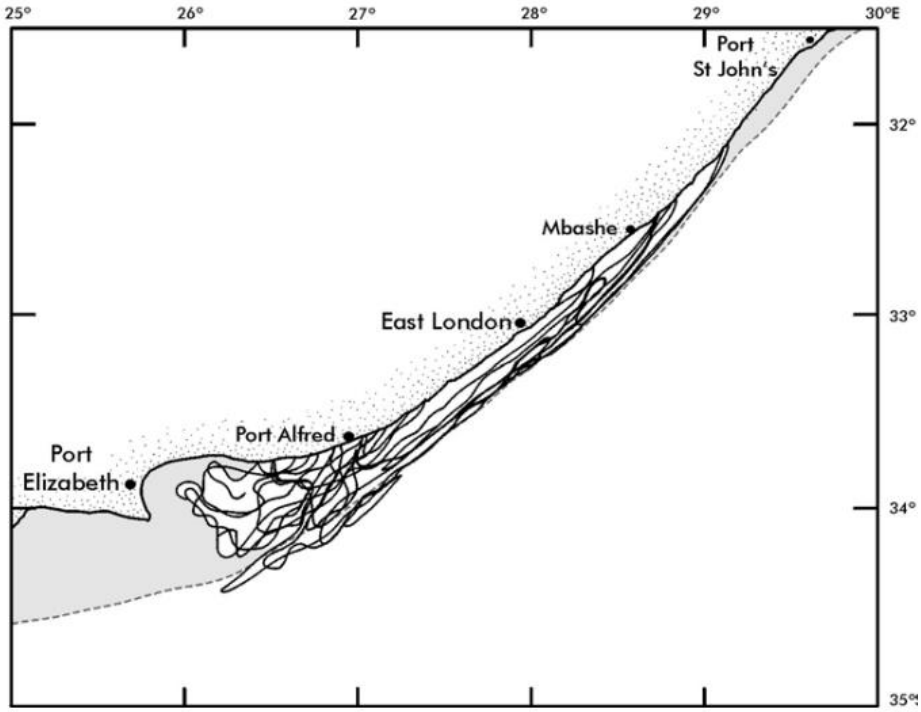

Figure 1.2: Isotherms to highlight the upwelling at Port Alfred (Lutjeharms et al., 2000b)

Lutjeharms (2006) reported that measurements of temperature in the inshore upwelling zone of Port Alfred show an average temperature between 14.3°C and 17.3°C at 80 m depth. Lutjeharms et al. (2000b) also noted that the contrast in the surface expression of upwelling, was clearly evident from satellite images taken 25 days apart in Figure 1.3. On March 30, 1991, they recorded a decrease of 11°C compared to that of the Agulhas Current, and the temperature in the upwelling zone was at least 5°C cooler than the surrounding shelf waters. Conversely, on March 5, during the absence of an upwelling event, the sea surface temperature in Port Alfred was fairly similar to the broader Agulhas Bank region.

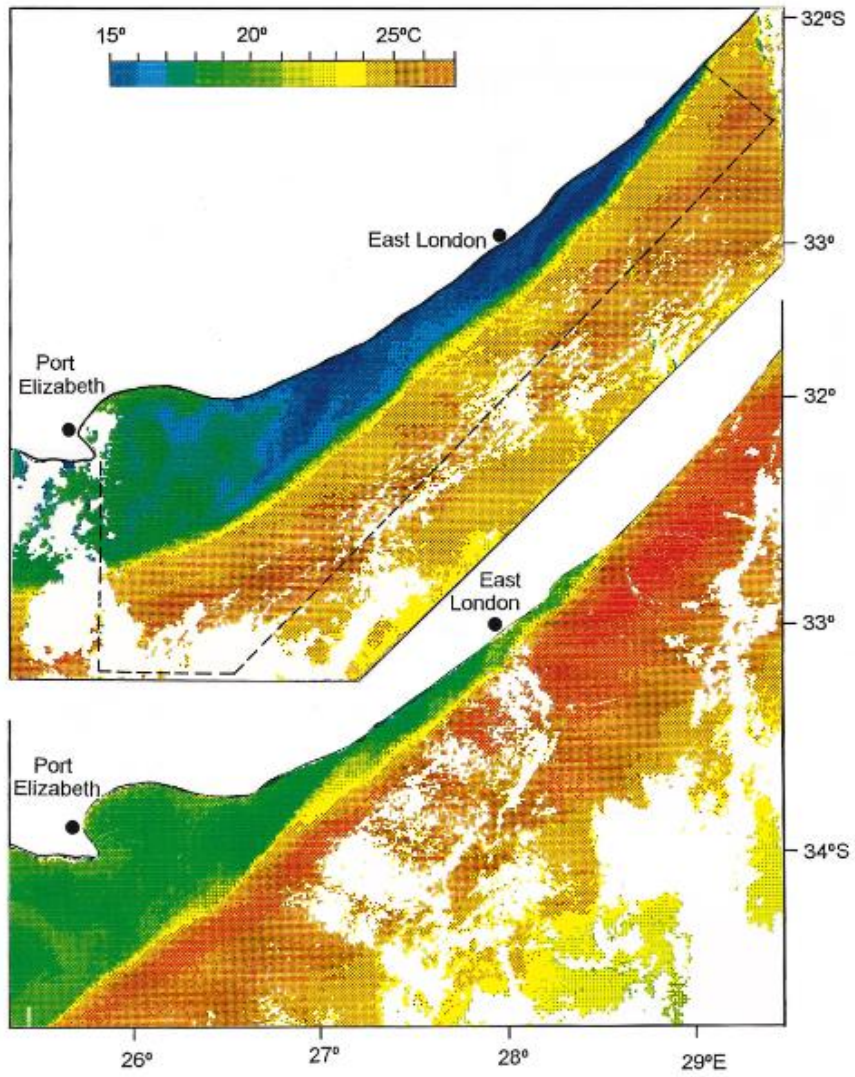

Figure 1.3: Presence of upwelling on 30 March 1991 (upper panel) and no presence of upwelling on 5th March 1991 (lower panel) (Lutjeharms et al, 2000b)

Earlier investigations of salinity measurements near Port Alfred indicate an average salinity of 35.3 PSU, which is notably lower than that of the surrounding surface waters of the Agulhas Current (Lutjeharms, 2006). The water masses from this upwelling primarily comprise of Subtropical surface water with occasional pulses of Tropical Surface Water, particularly on the landward side. Water upwelled from depths exceeding 500 meters is expected to possess significantly elevated nutrient levels compared to surface waters, thereby contributing to increased biological primary productivity within the area (Lutjeharms, 2006). Nutrient values in the upwelling cell can exceed 20 µmol/ℓ, indicating a rich source of nutrients for marine organisms (Lutjeharms, 2006).

1.2 Driving mechanisms of the Port Alfred upwelling

A summary of the literature suggests that its driving mechanism has been linked to many hypotheses.

1) While the northeasterly wind component has been identified as a potential driver, capable of inducing offshore Ekman transport and surface divergence (Goschen et al., 2012), it fails to account for the exclusive presence of upwelling solely in Port Alfred. This discrepancy becomes even more apparent when considering that other coastal sites with similar wind patterns do not consistently exhibit upwelling throughout the year.
2) In addition to wind-driven mechanisms, the influential role of the Agulhas Current cannot be overlooked. The Agulhas Current's impact on upwelling stems from several factors, including the widening of the continental shelf, which conserves potential vorticity, and the narrowing of its inertial jet (Gill and Schumann, 1982). Furthermore, an intensified Agulhas Current can increase friction against the seafloor, leading to onshore bottom Ekman transport and subsequent upwelling (Malan, 2013).
3) Eddy-induced upwelling, triggered by phenomena like Natal pulses, Durban eddies, and shear-edge eddies, has also been explored (Goschen et al., 2015), alongside the potential influence of coastal trapped waves (Malan, 2013). However, Natal pulses do not occur consistently throughout the year, unlike the observed upwelling activity in Port Alfred, and the hypothesis regarding coastal trapped waves remains unverified due to a lack of empirical studies.
4) Ultimately, it is suggested that the Port Alfred upwelling is likely the result of a combination of different mechanisms, highlighting the intricate nature of oceanic processes in this region (Goschen et al., 2015; Leber et al., 2017).

While some insights have been gained from analytical models, *in situ* data, and remote sensing, a numerical modelling approach has yet to be fully utilized. As a result, we still do not have a clear picture of the driving mechanisms of this upwelling.

1.3 What makes Port Alfred upwelling interesting?

Port Alfred upwelling has long piqued the interest of oceanographers due to its significant impact on the local ecosystem and fisheries. This upwelling has implications for the distribution and abundance of zooplankton and fish species in the area, with distinct patterns observed in relation to the upwelling activity (Hutchings et al. 1995; Bower et al. 1985). Studying this upwelling is essential for gaining a comprehensive understanding of the physical, chemical, and biological processes in the Agulhas region.

The significant temperature difference observed between the upwelling cell and the neighboring Agulhas Current make this zone an ideal natural laboratoy for investigating air-sea interaction. Findings derived from both analytical or numerical models, incorporating realistic forcing parameters, could aid in narrowing down the potential driving mechanisms for this upwelling phenomenon.

1.4 Aim and outline of this study

The main objective of this study is to gain a comprehensive understanding of the Port Alfred upwelling through a numerical modelling approach by assessing the influence of different atmospheric and oceanographic forcing on this upwelling. This section will be discussed more in detail later in section 2.5.

This study comprises of 8 chapters. Chapter 2 outlines the different types of upwelling, a review of the study area, the different hypotheses of the upwelling and the current gap in the research. In chapter 3, we discuss the datasets which are used in this study as well as the different CROCO grids. Chapter 4 provides a description of the spatial and temporal characteristics of the upwelling. In chapter 5, we assess the influence of atmospheric forcing mechanisms on the upwelling at different temporal scales. As for chapter 6, we investigate the influence of the Agulhas Current, meander events and coastal trapped waves on the upwelling. Chapter 7 provides a statistical approach to assess the possible drivers of the upwelling. Chapter 8 summarises the conclusion of this work and presents avenues for future studies.

Chapter 2: Literature review

2.0 Introduction

The current oceanographic literature consists of a vast range of upwelling studies as oceanographers have been exploring this phenomenon for more than a century. There has always been a growing interest in the upwelling research as this process is crucial for nutrient regeneration and higher productivity in the surface layer. This chapter has been divided into five sections. Firstly, we reviewed previous upwelling studies conducted on a global scale and discussed the different types of upwelling. Secondly, we identified the main atmospheric and oceanographic features which could potentially lead to upwelling in the Agulhas Current region. We also presented the different upwelling zones. We then presented a review of the major published work previously conducted on the Port Alfred upwelling during the last three decades. Lastly, we identified the current gap in the research and addressed the future research questions we aimed to solve in this study.

2.1 Upwelling research on a global scale

There are various mechanisms, which can trigger upwelling. Some of them include offshore Ekman transport, changes in seafloor's bathymetry and cyclonic eddies. In this section, we discussed some of the major upwelling drivers identified from previous studies.

2.1A Wind-driven upwelling – Upwelling due to offshore Ekman transport

Offshore Ekman transport is a process that occurs when wind-driven surface waters are deflected by the Coriolis effect, causing them to move at a 90-degree angle from the direction of the surface wind. This process causes surface waters to pile up in some areas of the ocean and removes water from other areas, producing variations in sea surface height. Figure 2.1 shows a schematic view of offshore Ekman transport driving upwelling at the coast.

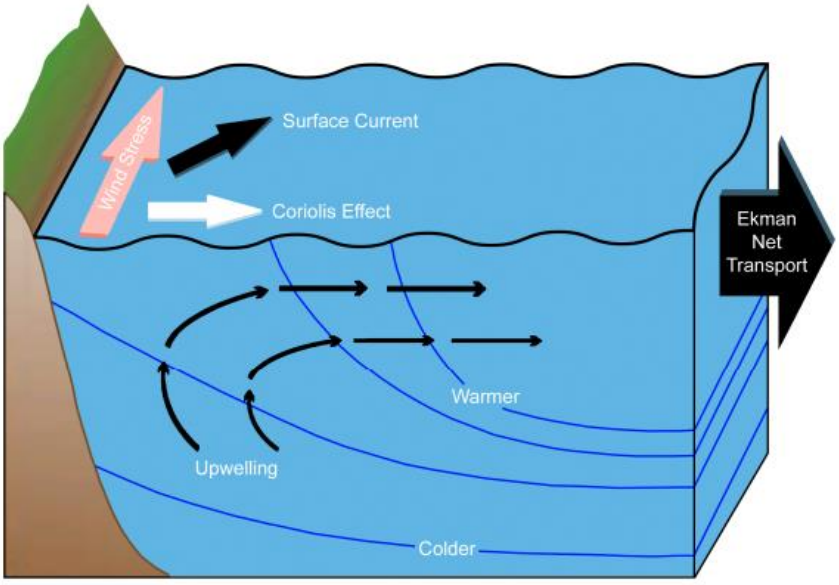

Figure 2.1: Schematic view of wind driven upwelling in the northern hemisphere. (Clemente-Colón, 2001)

The identification of coastal upwelling systems, both major and seasonal, had been facilitated by analysing surface wind maps, where the guiding principle had been that upwelling resulted from winds running parallel to the coast, driving water offshore within the surface Ekman layer. This approach had identified significant upwelling regions along the coastlines of California, Peru, Chile, northwest Africa, Namibia and Portugal (California Current, Peru-Chile Current, Canary Current, Benguela Current and Portugal Current) shown in Figure 2.2. Collectively termed major coastal upwelling regions or eastern boundary upwelling regions, these areas had exhibited consistent year-round upwelling.

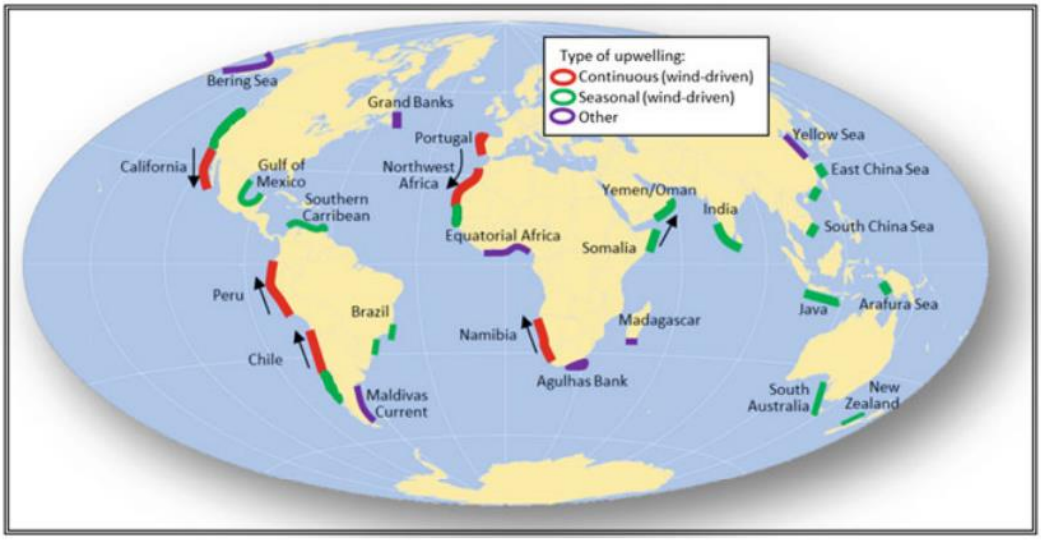

Figure 2.2: Global map of significant coastal upwelling sites (Kämpf, 2016)

Through offshore Ekman transport, we had also identified seasonal upwelling systems. These locations include the coasts of Somalia, Yemen/Oman, Sumatra, and the South China Sea. Additionally, seasonal coastal upwelling systems were observed along the southwest coast of India and the southern shelves of Australia, despite less apparent wind distribution patterns in those regions. This underscores the significance of offshore Ekman transport in driving seasonal upwelling phenomena in various coastal areas worldwide.

2.1B Wind-driven upwelling – Upwelling due to surface divergence

Sverdrup et al. (1942) had attributed wind stress curl as a contributor of upwelling through Ekman pumping. The divergence of horizontal Ekman transport led to the vertical turning of the pycnocline. While coastal upwelling allowed a cross-shelf exchange, Ekman pumping had been only triggering a vertical flow. Messié et al. (2009) had previously calculated that more than 25% of the vertical nutrient flux had been attributed to surface divergence in the main eastern boundary upwelling regimes.

Kraus and Businger (1994) emphasized that the distinction between wind stress and wind stress curl lies in the divergence induced by wind stress curl, which tends to occur significantly farther offshore, often at the continental shelf's boundary. This phenomenon facilitates a more rapid vertical transport compared to offshore Ekman transport. Consequently, it operates independently from inshore Ekman transport and can function as a secondary mechanism for upwelling.

2.1C Wind induced turbulence –Vertical mixing

Elevated wind speeds can result in a rise of frictional velocity at the ocean's surface leading to upwelling events. This increase in frictional velocity plays a pivotal role in triggering turbulence and subsequent vertical mixing. In the Gulf of Guinea, Jouanno et al (2011) reported that southerly winds would initiate a northward surface flow along the equator, actively contributing to vertical mixing and cooling. Zhang et al (2014) also reported that wind-induced turbulence in South China sea would generate near-inertial waves that propagate downward. Similar phenomena of wind-induced turbulence and vertical mixing have been investigated in various other oceanic regions, such as the northeast Pacific Ocean, the Baltic Sea, and the Scotian Shelf whereby the intricacies of vertical mixing were prompted by local high winds (Van der Lee and Umlauf. 2011, Qi et al. 1995, Cuypers et al. 2013)

2.1D Upwelling due to shelf break

Dynamic uplift, also known as shelf-break upwelling, often occurs along the inshore edge of western boundary currents such as the Agulhas Current, even during the absence of favourable upwelling winds (Kampf, 2016). These warm ocean currents are often linked with a sharp increase of the thermocline towards the shoreline due to changes in bathymetry. Generally, they are situated at a

distance from the continental shelf, and their impact does not extend deeply into the coastal region, where local wind patterns and temperature-salinity dynamics largely govern the flow.

2.1E Upwelling due to bottom Ekman veering

Upwelling driven by currents can occur from a rise in current's velocity, amplifying onshore Ekman transport within the frictional bottom boundary layer, resulting in an upslope flux (Roughan and Middleton, 2002). This phenomenon, known as bottom Ekman veering, typically does not bring water all the way to the surface but generally acts as an additional contributing upwelling factor to a primary upwelling driving mechanism (Roughan and Middleton 2002; Goschen et al. 2015). In the East Australia Current (EAC), upwelling was forced by processes occurring downstream of the EAC's separation from the coast. A significant field study conducted by Roughan (2004) revealed that upwelling in this region intensified as the axis of the EAC current jet moved closer to the shoreline. This movement resulted in increased friction between the current and the ocean bottom. Consequently, Ekman pumping onto the continental shelf within the bottom boundary layer (BBL) was forced by the enhanced bottom friction leading.

2.1F Eddy induced upwelling

Eddy induced upwelling at the inshore edge of warm currents has been explored in the Gulf stream region (Churchill et al. 1986), South Brazil Current region (Campos et al., 2000) and the Agulhas Current region (Goschen et al. 2015). In the southern hemisphere for instance, a cyclonic eddy would cause upwelling in two ways. At the leading front edge of the eddy, surface waters would converge towards the center, drawing up colder, nutrient-rich water from the bottom through Ekman transport (Campos et al., 2000). Meanwhile, at the eddy's center, surface waters would diverge, creating a low-pressure area. This low pressure would prompt deeper, cold water to rise and replace the diverging surface waters, resulting in upwelling.

2.1G Tidally induced upwelling

The map in Figure 2.2 also includes the Yellow sea and the Irish sea, whereby tidal mixing fronts are known to trigger upwelling. This type of upwelling is also known as tidal pumping. Thompson and Golding (1981) emphasized that it is a localized phenomenon characterized by the regular movement of deep and cold water across the shelf break via oscillatory tidal flows. This phenomenon is observed in various regions, such as semi-enclosed basins, estuaries, and coastal areas.

2.1H Upwelling due to coastal trapped waves

Coastally trapped waves exhibit intraseasonal variability with a periodicity ranging from 30 to 60 days. They reach their peak amplitude near the coast, generating temporary upwelling and downwelling as they interact with onshore and offshore flows along the shelf edge. While coastal winds often initiate these waves, equatorial Kelvin waves can also contribute to upwelling,

particularly on the eastern side of the equator (Shaffer et al., 1997). These waves can travel thousands of kilometres along the shoreline. Coastal trapped waves can be detected from mooring arrays, tidal gauges and sea level stations along the shoreline of Chile, Peru, and Ecuador (Shaffer et al., 1997).

2.1I Upwelling in the wake of islands

Anecdotal evidence from fishermen have suggested that there is upwelling activity occurring in the proximity of islands, as illustrated in Figure 2.1. The scientific documentation of this phenomenon, known as the island wake effect, was initially undertaken by Doty and Oguri in 1956. Notably, nutrient levels, such as nitrate, exhibited a potential tenfold increase within the wake area and they differed to the sites located upstream (Heywood et al. in 1990). Additionally, density surfaces could undergo a substantial shoaling, reaching depths as shallow as 100 meters. The mechanism driving upwelling behind islands in shallow seas could be elucidated by the 'tea cup effect,' elucidated by Wolanski and Hamner in 1988. Generally, the flow encircling an island generated a pair of counter-rotating eddies in the lee of the island. Within these eddies, rotating in opposing directions, an inward pressure gradient provided the necessary support for the centripetal acceleration of the fluid. This convergence in flow dynamics facilitated upwelling, akin to a tea cup effect, concentrating the 'tea leaves' in the central region of the cup, as elucidated by Hasegawa et al. in 2004.

2.1J Upwelling due to shelf break canyons

Upwelling may also be influenced by shelf-break submarine canyons. These submerged formations extend across the shelf break, and relying on their alignment, ocean currents at the shelf break depth can induce regional upwelling at continental shelf (Hickey, 1997). Figure 2.3 illustrates the schematic view of the process of upwelling caused by this geological formation. Allen and Hickey (2010) noted that upwelling due to shelf break canyon can be divided into three stages, firstly a starting transient response, secondly a more steady advection-driven response and finally a relaxation stage. The process of canyon-induced upwelling is generally seen as a characteristic feature of stationary topographic Rossby waves, potentially causing localized onshore flows downstream from the canyon "crests" (Kämpf, 2012).

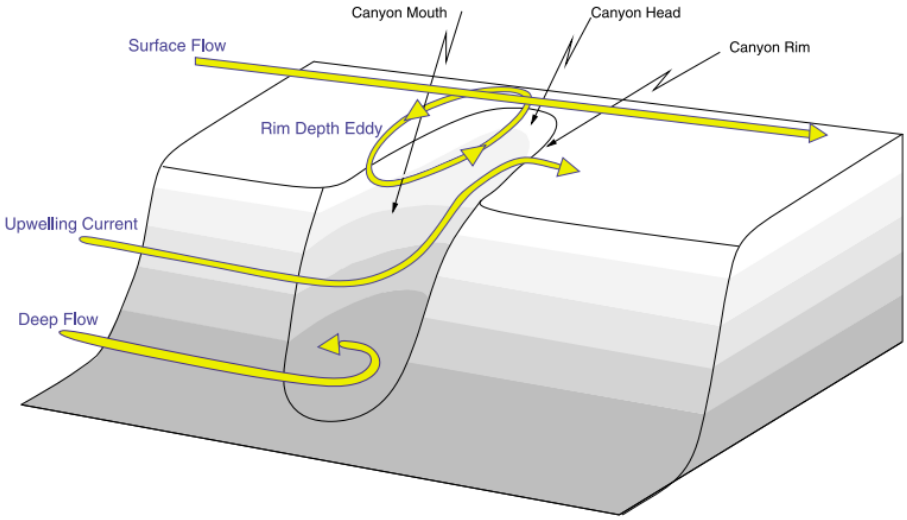

Figure 2.3: Schematic view of upwelling due to shelf break canyon (Allen and Hickey, 2010)

2.2 Reviewing upwelling activity in the coastal Agulhas system

After reviewing upwelling studies on the global scale in section 2.1, we focus on the literature of the chosen study area, the Port Alfred upwelling in section 2.2, 2.3, 2.4 and 2.5. To understand this upwelling, in section 2.2 we firstly identify the oceanographic (Agulhas Current, Durban breakaway eddies, Natal pulses, shear edge eddies and coastal trapped waves) and atmospheric processes which drive changes on the inshore circulation of the current and how some of these features can trigger upwelling activity in the Agulhas region. Section 2.3 highlights how Port Alfred upwelling is not the only upwelling site and lists the different upwelling zones (Cape Recife, Cape Padrone, Port Alfred upwelling, Natal Bight upwelling, cold ridge) in the Agulhas region. In section 2.4, we focus on the possible hypotheses behind the Port Alfred upwelling (atmospheric and oceanographic forcing mechanisms) and in section 2.5 address the current gap in the research and the key questions in this study.

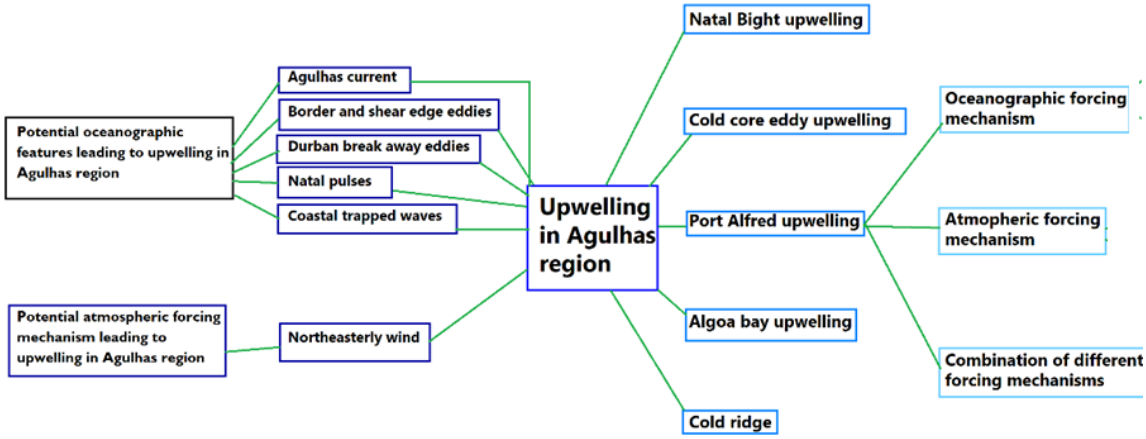

Figure 2.4 A breakdown of the potential oceanographic and atmospheric drivers of upwelling in the Agulhas region focussing on the Port Alfred upwelling which will be discussed in this chapter.

2.2A Oceanographic and atmospheric features linked to upwelling in the Agulhas region

The Agulhas Current.

The Agulhas Current is a western boundary current in the Indian Ocean which can be split into two zones, the north and south components, each with distinct set of features. The Northern side (Red box in Figure 2.5) consists of the current trajectory from 27°S to Port Alfred and the Southern side (Blue box in the Figure 2.5) is the zone, which covers from Port Alfred to 39°S. The Northern side is known to display a fairly steady path, an odd attribute for a western boundary current. However, Natal Bight is an unusually wide part of the continental shelf off southeastern Africa, along the path whereby the shelf is quite shallow. This site is known to be the epicentre of cyclogenesis, essential for triggering many different mesoscale processes such as the Natal pulses (de Ruijter et al., 1999b) and breakaway Durban Eddies (Roberts, 2010).

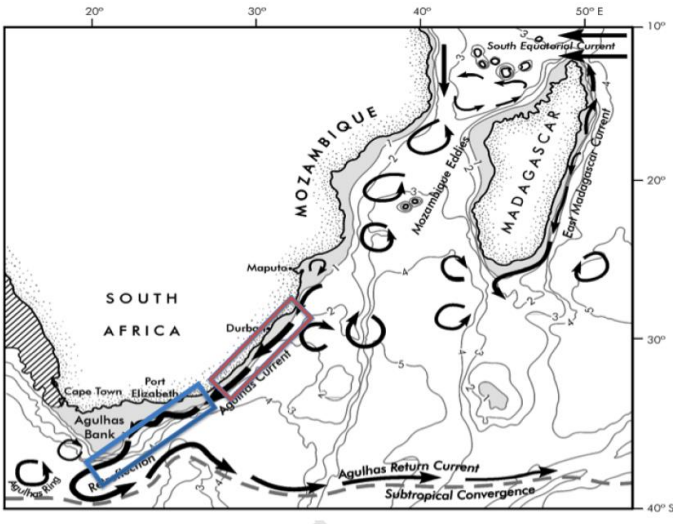

Figure 2.5: North (red) and south (blue) component of Agulhas Current (Lutjeharms, 2006)

As for the south component of the current, the trajectory tends to be more varying due to the changing nature of the topography of the seafloor of the shelf. The bathymetry of the northern part is much more narrower and deeper. But eventually the shelf broadens downstream and this leads to a rise in the formation of meanders and other mesoscale features. Shear edge eddies are also seen to occur more often due to the broadening of the shelf onto the Agulhas bank, a site which consists of a broad and shallow shelf (Largier and Swart, 1987; Lutjeharms, 2006).

Port Alfred, being located between the north and the south components of the current, tend to be influenced by the dynamic processes of both regions. In the next section, we will discuss a few mesoscale features from both regions which are possibly linked to upwelling activity.

Presence of Natal pulses

The large solitary meander, referred as the Natal Pulse remains the most prominent mesoscale feature along the Agulhas Current (Lutjeharms and Roberts, 1988). These cyclonic eddies are shaped from instabilities and initiate from the Natal Bight (de Ruijter et al., 1999b), and eventually flow further south, while their amplitude grows bigger. Rouault and Penven (2011) reported that on average there are 1.6 Natal Pulses annually which travel past Gqueberha (previously known as Port Elizabeth), however other studies have estimated 4 - 6 Natal Pulses annually. (Lutjeharms and Roberts, 1988). Recently Russo et al. (2020) applied a current tracker algorithm and reported 1.8 large meander events per year.

Presence of Durban break away eddies

The Durban break away eddies, smaller cyclonic eddy formations originating in the Natal Bight, emerge approximately every 15 days, causing the flow of the current to reverse near the coast (Roberts et al., 2010). Unlike Natal Pulses, these eddies are flattened and elongated along the coastline, facilitating the advection of warm water plumes onto the shelf. Annually, there are more Durban breakaway eddies compared to Natal pulses.

Presence of border and shear edge eddies

Lutjeharms et al. (1989) conducted a study by using *in situ* data from hydrographic surveys and remote sensing data to study shear features and boundary processes of the current and noted a shift of the current's meandering pattern near Gqueberha, whereby the meanders' amplitude grow bigger. This gave rise to the production of trailing of long warm plumes which would in turn lead to an advection onto the shelf. They also observed that these cyclonic eddies and the warm plumes were inducing upwelling. In another study conducted Lutjeharms (2006) confirmed that there was an increase in meanders and shear edge eddies. This was further verified by Rouault et al. (2010) whereby they studied these dynamic mesoscale processes in the Agulhas region.

Presence of coastal trapped waves

Influence of coastal trapped waves in the inshore region was earlier highlighted by Schumann and Brink (1990). They report that for small region along the south and the east coast, these waves have large amplitudes and would travel eastwards. It is assumed that they are triggered by westerly winds and propagate to the coast as far as Gqeberha or East London, whereby the Agulhas Current holds a strong effect on them.

Wind pattern

The primary prominent atmospherical features shaping the southeastern African shelf are the passage of coastal low pressure systems and Subtropical high pressure system (Schumann, 1981). This anticyclone, positioned from 20°S to 40°S, is characterized by counterclockwise flow (Gupta and Desa, 2001). The southeastern African shelf is situated within the varying zone bridging the northern trade wind belt and the southern westerly wind belt (Hutchings, 1995). Throughout the seasons, these high pressure systems migrate by approximately 4° in latitude (Taljaard, 1953). The westerly wind belt takes precedence during winter due to the Subtropical high pressure system's northward movement, while in summer, when the anticyclone shifts southward, the trade wind belt becomes more dominant (Hutchings, 1994).

2.3 Upwelling in the Southeast African shelf

In section 2.2, we have addressed several dynamic processes (Agulhas Current, Border and shear edge eddies, Natal pulses, Durban break away eddies and coastal trapped waves) and the atmospheric processes in the Agulhas region, as each of these features can influence the circulation and possibly enhance upwelling activity. In section 2.3, we discuss the different upwelling zones located in the Agulhas region.

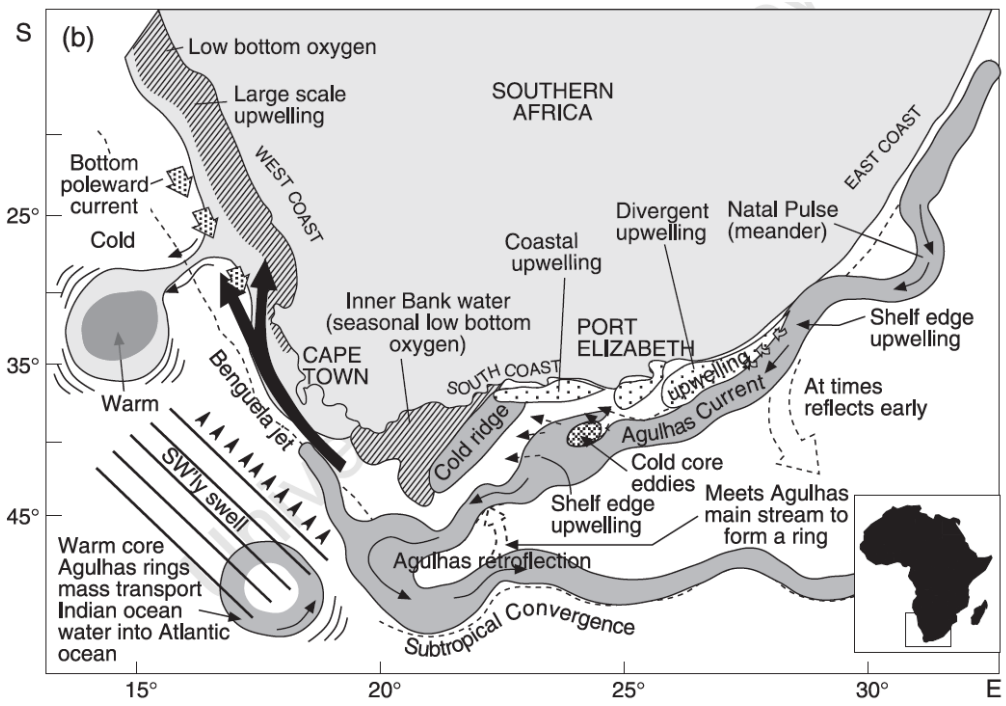

Figure 2.6: Schematic view of South Africa's mesoscale processes and upwelling zones (Roberts, 2010)

Figure 2.6 illustrates a schematic view of the different mesoscale features and different upwelling zones in this region. There is wind-driven upwelling off the capes (Cape Padrone, Cape Recife) (Schumann et al., 1982; Schumann, 1999; Goschen et al., 2012). Schumann et al (1982) suggest that coastal upwelling is triggered by persistent easterly winds at the coast and at major headlands in Algoa Bay. Beckley (1988) earlier studied the upwelling cell at Cape Recife and reported that the temperature decreased in Algoa Bay at Sundays River and suggested that the wind driven upwelling cell at Cape Padrone was moving from east to west, near Cape Recife. Schumann et al. (1988) further confirmed the upwelling by looking at remote sensing data and *in situ* data at Bird Island. They noted that the upwelled water was originating from Cape Padrone.

Other upwelling activity includes eddy core upwelling along the current (Lutjeharms et al., 1989). Strong shear-edge eddies influenced by the Agulhas Current trigger upwelling activity on the inshore side of the current on the shelf. (Lutjeharms et al., 1989a; Goschen and Schumann, 1990). There is also shelf edge upwelling in Natal Bight and Port Alfred. Upwelling at these 2 sites is known to be influenced by the current (Lutjeharms et al., 2000b; Lutjeharms, 2006).

As for Port Alfred, due to its location, is often not studied in depth as most studies are either focused on the north or south component of the Agulhas region. Hence it can be complex to draw conclusions from the literature on this site. Due to the lack of studies conducted at Port Alfred, there is still a cloud of uncertainty on how these mesoscale processes can exactly trigger upwelling and there is a strong need to investigate these links.

2.4 Revisiting possible hypotheses triggering upwelling in Port Alfred

Many studies have suggested different driving mechanisms which would trigger upwelling in Port Alfred. So far, all these studies have relied on *in situ* data, analytical models and remote sensing datasets, but none of them have used simulations of a numerical model. Some of the studies have identified it as current-driven upwelling, while others have recognised that there is a strong influence of atmospheric forcing on the upwelling. There are also studies which pointed that this upwelling could be caused by a combination of several different mechanisms.

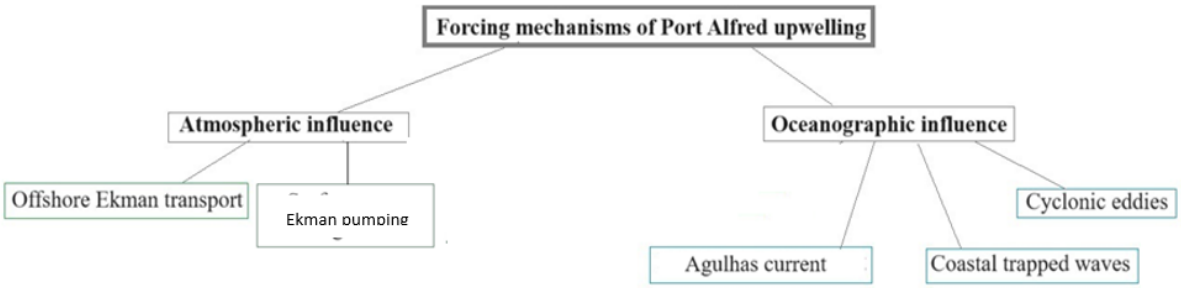

Figure 2.7: Different forcing mechanisms of the Port Alfred upwelling identified in section 2.4

2.4A Wind-driven upwelling hypothesis

Wind could also be a potential driver in the Port Alfred upwelling. Easterly and north-easterly winds often occurred in summer and were noted as highly upwelling favourable (Schumann et al., 1982). Gill (1982) noted that these winds can induce Ekman pumping or Ekman transport and this can in turn trigger coastal upwelling. In the Agulhas Current system, negative wind stress curl would strengthen the divergence at the surface, while the negative wind stress would lead to offshore Ekman transport. The layer which moved offshore by the Ekman transport is then replaced by the deeper one (Smith 1995). Goschen et al., (2012) referred to the upwelling in Port Alfred as a "cell" and used coastal mooring data over a time period of 100 days to conclude that the upwelling cell was less responsive to the wind compared to other upwelling zones in Algoa bay. They also reported that an upwelling cell could last from 19 hours to 2.5 days after the occurrence of a strong easterly wind component.

However if this hypothesis was the only one explaining this upwelling, then it would not explain why Port Alfred upwelling would be more pronounced than the other sites along the coast exposed to similar wind patterns.

2.4B Current driven upwelling hypothesis through shelf break upwelling

Agulhas Current is known to trigger upwelling at different sites in the Agulhas region. In the case of Port Alfred, this link has also been explored using theoretical models, *in situ* data and remote sensing datasets. According to Gill and Schumann (1979), a western boundary current streaming from a

narrow steep continental shelf to a broader and less deeper one could lead to upwelled water at the shelf edge of the current.

They claimed that fluctuations in the potential vorticity would cause variations in the development of an inertial jet current, leading to a movement of upwelled water at the region where the Agulhas Current shifts from a narrower shelf to a larger shelf domain. They reported that this process would lead to upwelling even if there was no wind nor any mesoscale features. However, according to their analytical model, they suggested that this type of upwelling would only happen at a site with the appropriate shelf configuration, such as Port Alfred and the upwelling will rely on the current's strength and direction.

2.4C Current driven upwelling hypothesis through Ekman veering in bottom boundary layer

Bottom Ekman veering is a potential upwelling forcing mechanism which can occur along western boundary currents. Roughan and Middleton (2002) reported that this phenomenon has been recorded along the inshore edge of the East Australian current. Malan (2013) also reported that upwelling in Port Alfred driven by bottom Ekman veering was a continuous process. However Roughan and Middleton (2002) and Goschen et al. (2015) found that this process did not always cause the upwelled water to reach the surface but would instead act as an "accomplice" to cause upwelling when another upwelling-favourable forcing mechanism is also present. Recently, Leber et al (2017) also could not find upwelled water linked to a negative geostrophic velocity and hence could not attribute strong upwelling events to bottom Ekman veering.

2.4D Cyclonic eddy induced upwelling hypothesis

As identified in the previous section, cyclonic features such as the Natal pulses, border and shear edge eddies could trigger upwelling, and in the case of Port Alfred upwelling, there are a few studies which have explored this link. Lutjeharms et al. (2001) demonstrated that within a cyclonic eddy, water particles were advected along tilted isopycnal lines, showing an increasing vertical velocity (i.e an upwelling) at the front edge of the meander. Rouault et al. (2010) found that the extensive meandering and shear edge eddies were triggering upwelled waters, as well as intensifying the thermocline on the Agulhas bank from the intake of the warm water in the upper level. In another study, Goschen et al. (2015) used coastal moorings to explore the effect of six different meander events on the Port Alfred upwelling and reported that the upwelling would persist between 1 to 3 weeks during a meander event. They also found that sometimes the upwelled water would not reach the surface during two meander events. This study was focused solely on meander effect on upwelling and did not take into account other external factors. From the findings of Lutjeharms et al. (2001), Pivan et al. (2016) examined a Natal pulse event occurring in June/July 1998 and illustrated that the highest vertical velocity within the cyclonic core are linked to colder water masses and the phenomenon of upwelling at the leading edge of the cyclonic eddy. Border eddy processes have also been known to contribute to

upwelling activity in other western boundary currents, such as the Gulf stream (Churchill et al.,1986) and the South Brazil current (Campos et al., 2000). In these cases, these eddies have led to the occurrence of upwelled waters on the leading edge of the meander, a cold dome in the middle and a warm plume on the trailing edge.

However, it must be noted that the hypothesis of Natal pulses triggering upwelling activity in Port Alfred is problematic. As mentioned earlier in section 2.2A, Natal pulses would not occur frequently throughout the year and hence this would not justify the semi permanent upwelling activity in the region.

2.4E Upwelling due to coastal trapped waves hypothesis

It is likely that coastal trapped waves could be linked to the Port Alfred upwelling. Coastal low-pressure systems, impacting the southeastern African shelf's coastal environment, initiate along South Africa's western coast and progress eastward, tracing the southern African coastline (Schumann, 1981). These coastal low-pressure systems' progression aligns with the movement of sea level perturbations identified as coastal-trapped waves (Roberts et al., 2010). Schumann and Brink (1990) observed that when coastal low-pressure systems and coastal trapped waves coincide, temporary reversals in barotropic currents occur at the coast.

This hypothesis has not been tested yet in Port Alfred however, in their study, Goschen et al. (2012) examined upwelling at a site further south of Port Alfred, known as Woody Cape. Over a span of 400 days, they detected 55 instances of upwelling at that site. The majority of these upwelling incidents were correlated with coastally trapped waves and prevailing alongshore winds that promote upwelling. They defined upwelling events as instances where the temperature at a depth of 30 meters experienced a temperature decrease of 18 degrees Celsius or more within a 24-hour timeframe.

2.4F Influence of a combination of oceanographic and atmospheric forcing mechanism

Each of these forcing mechanism mentioned above has been possibly linked to upwelling activity in Port Alfred. However, these previous studies have used datasets which were limited to a short time period, had a coarse spatial resolution and they only looked at one forcing mechanism. In other western boundary current systems such as the Brazil current system, it has been observed that a combination of different forcing mechanisms was responsible for upwelling on its inshore edge. Brandini (1990) found that a high nutrient concentration would be observed on the inshore edge of the Brazil current during a meander event. Campos et al. (2000) used simulations from MICOM (Miami Isopycnic Coordinate Ocean), a numerical model to study the upwelling on the shelf edge of the Brazil current and identified it as a seasonal upwelling. They found that it was triggered by a combination of different upwelling drivers which included the current, the meanders and wind-driven upwelling. As a follow up study, Castelao and Barth (2006) noted that the addition of upwelling favourable wind stress needed to be present for the upwelled water to reach the surface. They also

highlighted that wind stress curl could also be a key contributor to this upwelling, just like the alongshore winds. In the Gulf stream, upwelling has also been observed to be caused by shelf break upwelling and meanders (Flierl and Davis 1993; Lee et al. 1981).

In the case of Port Alfred, it is possible that a combination of different forcing mechanisms was responsible for this upwelling and this theory has been presented in a few studies (Lutjeharms et al. 2000; Malan 2013; Leber et al, 2017). However, this area has been poorly sampled, and there has been only one study which has recently investigated the effect of different forcing mechanisms. Leber et al (2017) made use of hydrographic and satellite data as well as CCMP wind datasets and explored the link between the cold water events in Port Alfred upwelling and wind stress, wind stress curl, sea surface height and current strength. They worked with a dataset from 2003 to 2013 and conducted correlation studies between the sea surface temperature and each forcing mechanism. Leber et al. (2017) reported that the two variables, sea level anomaly and geostrophic current, showed a relatively stronger correlation with sea surface temperature. They also conducted a combined principal component analysis and explored the EOFs of stronger and weaker cold events. They found that a combination of cyclonic meanders and upwelling-favourable winds were necessary for the stronger cold events while only upwelling-favourable winds, with Ekman veering as an "accomplice" would force the weaker cold events. They also highlighted that the frontal curvature of the cyclonic meander coupled with the atmosphere and allowed the wind stress curl anomalies to strengthen the upwelling.

However, it must be noted that they were restricted to a 10-year period dataset and explored only 4 variables (sea level, wind stress, wind stress curl and geostrophic velocity). While they attempted to explore the link between the meandering effect and the upwelling, their methodology for identifying a meander was not robust enough as they simply used sea level anomaly. They were also limited to sea surface temperature data as they only relied on *in situ* and satellite datasets and could not investigate the subsurface upwelled waters.

2.5 Current gap in Port Alfred upwelling research

An analysis of the literature, it must be highlighted that most studies were either focused on the Northern or Southern regions of the Agulhas Current and both zones were very distinct from each other. Since Port Alfred is located at the midpoint between the two zones, it could also be argued that Port Alfred might be influenced mildly by a combination of the mesoscale features occurring in the Northern and Southern Agulhas Current.

Hence with the current literature available, it could be challenging to draw straight-forward conclusions on Port Alfred upwelling. Some studies have pointed out the strong influence of oceanographic forcing mechanisms such as the current or the meanders. Other studies have also highlighted that the atmosphere (wind stress, wind stress curl etc) also held an influence on this type of upwelling. While there are some hypotheses which have been tested, these tests have only been

done at specific time periods or by only making use of situ observations and remote sensing datasets. Recently, researchers seemed to agree that this upwelling could be triggered by a combination of different drivers. For instance, Leber et al (2017) tested a combination of different forcing mechanisms in the Port Alfred region through the use of *in situ* and satellite data, however, as mentioned in the last section, their study was limited to many restrictions.

Currently, oceanographers have still not made use of any simulations from numerical models to investigate all the forcing mechanisms behind the Port Alfred upwelling system. And there are still several untested hypotheses (either oceanographic or atmospheric forcing mechanism) which could lead to this upwelling and ought to be explored.

2.5A Aim

Hence, we set a main objective for this study:

Understanding the Port Alfred upwelling through a numerical modelling approach by assessing the influence of different atmospheric and oceanographic forcing mechanisms

Through this aim, we dissect this study into 4 main research questions.

2.5B Question 1: What is the spatial and temporal characteristics of the Port Alfred upwelling?

We aim to investigate the oceanographic properties such as temperature, salinity, and vertical velocity at different temporal scales. We test two upwelling indices to identify upwelling events. We also explore the link between sea surface temperature and vertical velocity. The last part is focused on the conditions during upwelling events where we focused on the mean state during selected upwelling events as well as an analysis of four case studies.

2.5C Question 2: What is the influence of atmospheric forcing on the Port Alfred upwelling?

We examine its alongshore wind stress, wind stress curl, wind direction, and frictional velocity. Firstly, we explore the impact of Ekman transport, Ekman pumping and turbulence induced winds within the Port Alfred upwelling zone at different temporal scales. We also delve into their correlation with sea surface temperature and vertical velocity. Additionally, we conduct detailed examinations of individual case studies and the overall upwelling state during upwelling events.

2.5D Question 3: What is the influence of oceanographic forcing on the Port Alfred upwelling?

We investigate the influence of the Agulhas Current, cyclonic eddies and coastal trapped waves on the upwelling across different temporal scales. Firstly, the impact of the Agulhas Current is analysed through its geostrophic velocity, surface and bottom ocean velocities, bottom Ekman transport, and sea surface height. Secondly, the role of meanders is explored using oceanic data and tracking methods like the LACCE algorithm and PY eddy tracker across different time scales. Lastly, the

potential influence of coastal trapped waves is investigated through sea surface height analysis and the application of the LACCE algorithm.

2.5E Question 4: Which oceanographic/atmospheric forcing variables are the most dominant during Port Alfred upwelling events?

Here our approach centre on employing a combined empirical orthogonal function (EOF) analysis to assess and compare various forcing mechanisms contributing to the upwelling phenomenon. The primary objective is to determine the dominant factor driving this upwelling process.

2.6 Highlights

As an overall, we highlighted some of the main findings of this literature review:

- On the global scale, there are different types of upwelling (e.g wind driven, shelf break, eddy induced upwelling, tidal induced upwelling)
- The northeasterly wind component could trigger offshore Ekman transport and surface divergence in the Port Alfred region (Goschen et al. 2012) however it would not justify why upwelling would occur only in Port Alfred when other sites along the coast are also exposed to similar wind patterns and do not always exhibit upwelling throughout the whole year.
- The Agulhas Current could induce upwelling due to the widening of the continental shelf due to the conservation of potential vorticity and the narrowing of its inertial jet (Gill and Schumann, 1982). An intensification of the Agulhas Current could also lead to stronger friction against the seafloor, inducing an onshore bottom Ekman transport leading to upwelling (Malan, 2013).
- Eddy induced upwelling due to Natal pulses, Durban eddies and shear-edge eddies has been explored (Goschen et al. 2015) and coastal trapped waves were also seen as a potential forcing mechanism (Malan, 2013). However Natal pulses do not occur throughout the whole year compared to the Port Alfred upwelling activity. As for coastal trapped waves, there has not been any studies to test this hypothesis yet.
- It is likely that the Port Alfred upwelling is driven by a combination of different mechanisms (Goschen et al. 2015; Leber et al. 2017).

Chapter 3: Materials and methods

3.0 Availability of data in Port Alfred

Port Alfred upwelling region has been poorly sampled and there were not sufficient studies to understand which mechanism/ combination of mechanisms were responsible for the upwelling. It must be noted that there are regular yearly hydrographic research cruises in this region (Agulhas Climate System Array cruise). However the data from these cruises cannot be used to analyse the upwelling in depth due to its size (15-100km). Despite the existing literature, the picture painted on the mechanisms behind the Port Alfred upwelling was only from analytical models, *in situ* data, hydrographic research cruises and remote sensing datasets while numerical modelling has not yet been utilized to investigate this upwelling thoroughly.

From the literature, conclusions could be drawn that Port Alfred upwelling could be influenced by oceanographic features such as the current, the meanders or by the atmosphere, such as the wind stress and wind stress curl. Furthermore, even if some studies pointed out that Port Alfred upwelling was triggered by a combination of different mechanisms, these researchers have only investigated a few drivers at the surface but did not explore all the possible drivers thoroughly and did not consider the vertical velocity. All these criteria were simply not sufficient to explain this type of upwelling. Hence alternative options needed to be explored to address the research questions on the Port Alfred upwelling.

3.1Choice of datasets

3.1A Observational datasets: CARS09

We used temperature and salinity data extracted from the CSIRO Atlas of Regional Seas 2009 (CARS09) dataset and calculated an interannual average for the purpose of comparison with other datasets. This dataset served as a digital climatology, compiling historical subsurface measurements and offering various data sets, including temperature and salinity [Ridgway et al., 2002]. It primarily relied on *in situ* measurements and autonomous profiling buoys, with additional data derived from the interpolation and averaging of oceanographic profile data. A locally weighted least square (LOESS) filter was applied to fit the data onto a uniform grid, simultaneously incorporating annual and semi-annual harmonics into the dataset [Ridgway et al., 2002]. Covering the global ocean at a spatial resolution of 0.5◦, the temperature and salinity fields in this dataset were based on multiple sources available up to 2008, including the World Ocean Database 2005 (WOD05), the World Ocean Circulation Experiment (WOCE) Program, and surface-pressure corrected Argo datasets.

3.1B Observational datasets: WOA18

The World Ocean Atlas 2018 (WOA18) provided comprehensive climatological data for various oceanographic variables including temperature, salinity, dissolved oxygen, nitrate, and phosphate. This data underwent objective analysis and was managed by the National Oceanic and Atmospheric Administration (NOAA). These climatologies were interpolated onto standard vertical levels and featured a global spatial resolution of 0.25◦. To derive the long-term mean temperature and salinity fields, an averaging process was performed across six decadal climatologies spanning from 1955 to 2018.

3.1C Observational datasets: OSTIA

The CMEMS (Copernicus Marine Environment Monitoring Service) OSTIA (Operational SST and Ice Analysis) reprocessed analysis product was a result of combining remote sensing and *in-situ* data to generate a sea surface temperature (SST) analysis. It was generated by the OSTIA system, utilizing re-processed data from ESA (European Space Agency) SST CCI (Climate Change Initiative), C3S (Copernicus Climate Change Service), EUMETSAT (European Organisation for the Exploitation of Meteorological Satellites), and REMSS (Remote Sensing Systems) remote sensing data, as well as *in situ* data sourced from the HadIOD (Hadley Centre Integrated Ocean Database). This product offered SST information starting from October 1st, 1981, covering the globe on a regular grid with a resolution of 0.05°. Updates were provided twice a year in the first and seventh month of the year. The primary feature of the CMEMS OSTIA reprocessed product was its ability to estimate foundation SST, which represented SST values without diurnal variability.

3.1D Numerical model: CROCO

We used the CROCO (Coastal and Regional Ocean COmmunity) model which was a type of oceanic modelling system that was established on ROMS (Regional Ocean Modeling System). It was able to solve the Naviers Stokes equations through a split-explicit, free surface and topographic following coordinate model to replicate the physical oceanographic processes at coastal and local scale (Shchepetkin and McWilliams, 2005). The Naviers Stokes equations were the primitive equations dictating the flow of water in three dimensions fChorin 1968). Through the AGRIF (Adaptive Grid Refinement In Fortran) tool, it was possible to have higher resolution through grid nesting and their 2-ways communication within a lower computational cost (Debreu and Blayo, 2008; Debreu et al., 2012).

3.2 CROCO simulations

This section was focused on the numerical simulations which were used to analyse the Port Alfred upwelling region. Firstly, we discussed the main features of the numerical model. We then focussed

on the chosen numerical options which contributed to the configuration of the model, such as the choice of the number of nested grids, the resolution and time period.

3.2A Equations of motion

Here below are the primitive equations of motion (Shchepetkin & McWilliams 2005), solved in CROCO in Cartesian coordinates:

$$\frac{\partial u}{\partial t} + \vec{v}.\nabla u - fv = -\frac{\partial \phi}{\partial x} + F_u + D_u \quad \text{(A.1)}$$

$$\frac{\partial v}{\partial t} + \vec{v}.\nabla v + fu = -\frac{\partial \phi}{\partial y} + F_v + D_v \quad \text{(A.2)}$$

$$\frac{\partial T}{\partial t} + \vec{v}.\nabla T = F_T + D_T \quad \text{(A.3)}$$

$$\frac{\partial S}{\partial t} + \vec{v}.\nabla S = F_S + D_S \quad \text{(A.4)}$$

$$\frac{\partial \phi}{\partial z} = -\frac{\rho g}{\rho_o} \quad \text{(A.5)}$$

$$\frac{\partial u}{\partial x} + \frac{\partial v}{\partial y} + \frac{\partial w}{\partial z} = 0 \quad \text{(A.6)}$$

$$\rho = \rho(T,S,P) \quad \text{(A.7)}$$

- Equation A.1 and A.4: the horizontal momentum equations.

- Equation A.3 and A.4: the advection-diffusion governing the potential temperature. *T* and salinity *S*.

- Equation A.5: the hydrostatic ad mass balance.

- Equation A.6: the continuity equation for an incompressible fluid.

- Equation A.7: the equation of state for seawater (Shchepetkin & McWilliams 2005).

Symbols in the equations:

- x,y,z - are the zonal, meridional and vertical directions (m) in the Cartesian coordinate system.
- u,v,w - are the components of the vector velocity ~v (m s^{-1}) in x,y,z respectively.
- t - is the time in seconds (s).
- f - is the Coriolis parameter (s^{-1}).
- φ - is the dynamic pressure ($m^2 s^{-2}$).
- F_u, F_v, F_T, F_S - are the possible forcings terms.
- D_u, D_v, D_T, D_S - are the dissipative terms.
- T - is the potential temperature (°C).
- S - is the salinity (psu)
- ~g - is the acceleration of gravity (m s^2).
- ρ - is the seawater density (kg m^{-3}).
- ρ_o - is the mean seawater density (kg m^{-3}).
- P - is the total pressure (N m^{-2} or Kg m^{-2}).

These equations included 3 assumptions namely the Boussinesq approximation, the hydrostatic approximation and the incompressibility of the fluid (Shchepetkin and McWilliams, 2003, 2005).

1. The Boussinesq approximation took into account that density fluctuations were minimal and could be ignored in the Navier Stokes equations except for the gravitational force. This assumption was derived from the idea that the horizontal acceleration of fluid motions was relatively minor compared to gravity.
2. The Hydrostatic approximation meant that the ocean was a thin coat of liquid with horizontal scales leading over vertical scales. This implied that the vertical fluctuations of pressure occurred due to variations in density and not inertial motions. Hence, the pressure gradient on the vertical was balanced by gravity.
3. Incompressibility of seawater depended on the notion that the mass of a particle did not change with pressure. The continuity equation could then be simplified to a non-divergence condition of the ocean's velocity. Hence the vertical velocity, *w*, could be derived from horizontal velocity (*u*, *v*) through the non divergence equations.

These assumptions and approximations proved to be useful in providing a simpler mathematical display of oceanic fluid dynamics, hence allowing it to be modelled and understood more easily. The primitive equations were made of the conservation of horizontal momentum, hydrostatic balance,

incompressibility of fluid, an equation of state for seawater linking temperature and salinity to density at a given depth and transport equations for tracers. The model relied on primitive equations to calculate time-averaged variables, incorporating turbulent processes through the Reynolds stress term at the sub-grid level. This term was parameterized using both vertical mixing and horizontal dissipation components. Bottom conditions were determined by bottom friction, while surface conditions were influenced by wind stress. Horizontal dissipation could be explicitly specified or implicitly affected by the horizontal advective scheme.

The CROCO grid utilized a curvilinear horizontal coordinate system while employing vertical stretching conforming to topographical contours. This adaptable framework accommodated varying land and topographical shapes, providing an accurate representation of the domain. The strategy of stretching at both surface and bottom levels, introduced by Haidvogel and Beckmann (1999) and Shchepetkin and McWilliams (2009), was instrumental in capturing the model's boundary layers. However, this vertical grid system could introduce inaccuracies when calculating pressure horizontal derivatives in regions with steep slopes (McCalpin, 1994). To mitigate these inaccuracies, pressure horizontal derivatives were computed based on seawater density (Shchepetkin and McWilliams, 2003), and high-order schemes were employed to minimize truncation errors during discretization (McCalpin, 1994; Shchepetkin and McWilliams, 2003). Specific criteria for topography smoothing and vertical grid stretching further controlled errors, ensuring a more accurate domain representation while minimizing unwanted numerical artifacts.

The CROCO model operated as a free surface model, necessitating the use of a split-explicit time-stepping technique to address the hydrostatic primitive equations governing momentum. This approach involved two modes: the slower barotropic mode and the faster baroclinic mode, as described by Shchepetkin and McWilliams in 2005. The barotropic mode encompassed barotropic momentum and continuity equations, while the baroclinic mode included baroclinic momentum and tracer equations. The model advanced free-surface and vertically integrated momentum equations by executing a finite number of barotropic time steps within each baroclinic step. This strategy mitigated errors arising from frequency aliasing between barotropic and baroclinic steps. To comply with the 3D continuity equation, the barotropic model employed a specialized two-way time-averaging technique. For baroclinic mode discretization, a third-order predictor Leap Frog step combined with an Adams-Molton corrector time-stepping algorithm was implemented, allowing for larger time-step sizes (Shchepetkin and McWilliams, 2005).

On the horizontal plane, the model adopted the Arakawa-C grid introduced by Arakawa and Lamb in 1977 to discretize motion equations. This grid had a unique variable-placement arrangement, making it suitable for scenarios requiring finer horizontal resolutions than the first Rossby radius of

deformation, as discussed by Hedstrom in 1997. Variables such as ρ, h, f, and ω were defined at the center of the grid cell, while u and v were defined at the southern/northern and eastern/western cell boundaries, positioned half a grid cell away from the center. Tracer properties, including temperature and salinity, along with sea surface height γ, were defined at ρ points.

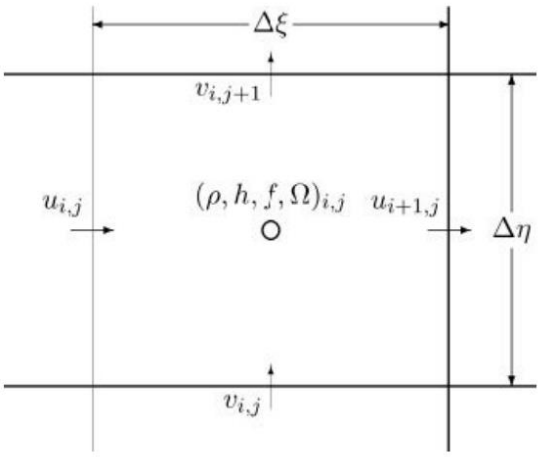

Figure 3.2: Variable points on the horizontal plane on a staggered Arakawa C-grid [From Hedstrom [1997]

3.2B Regional nested grids

There were three grids which were constructed from the ROMS TOOLS (Penven et al.,2008), namely the parent grid (Dx~22.5km), the first child grid (dx~7.5km) and the second child grid (dx~2.5km) running from 1993 to 2014. In this section, we provided a description of the selected configurations of these 3 numerical simulations such as the 2-way embedding procedure, the momentum and tracers advection scheme, the turbulent closure, the bathymetry and vertical grid, and the surface and boundary forcings. The purpose of these nested grids was to understand the dynamics of the Agulhas Current from a modelling approach, as well as different mesoscale and submesoscale features occurring in the region.

Parent grid (Dx ~ 22.5km)

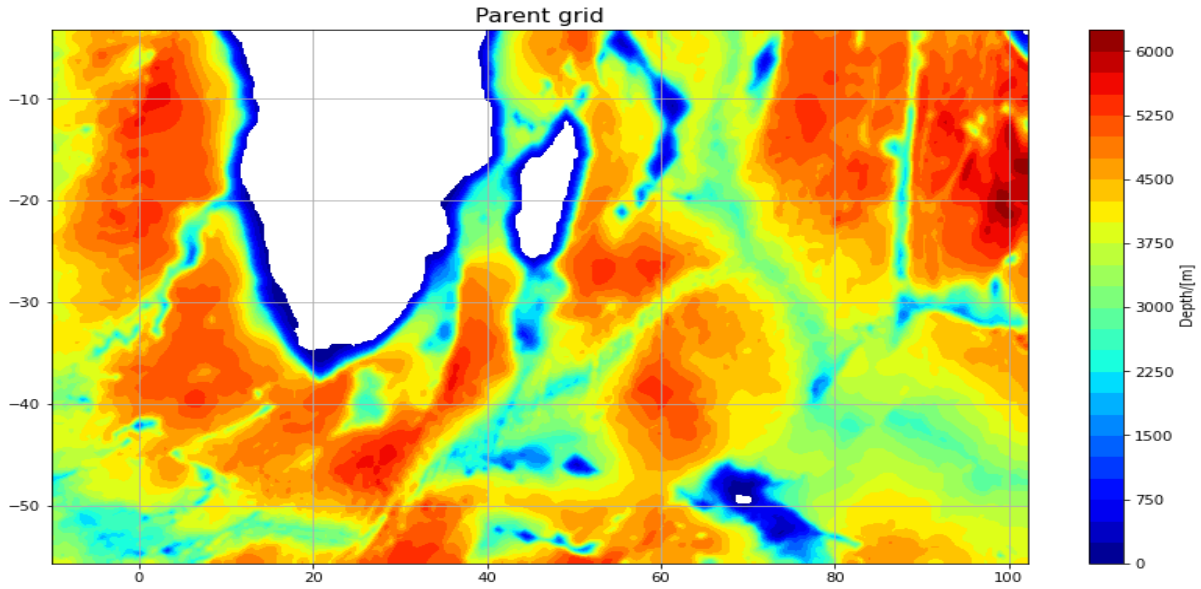

Figure 3.3: Parent grid's bathymetry

The parent grid was a rectangular domain which covered the zone from 3.18◦S to 55.7◦S, and from the South East Atlantic ocean (10°W) to the South Equatorial Indian ocean (102.25'E). This geographical domain produced a simulation of the Benguela and the Agulhas Current at a horizontal spatial resolution of ~22.5 km (1/4°) and consisted of 60 vertical levels. Despite having a coarse resolution, simulations from this parent grid were able to reproduce the Agulhas Current linking the Indian to the South Atlantic ocean through the Agulhas leakage (Beal et al., 2011) and the connection between the Antarctic and Indian ocean through the Agulhas Return Current (Lutjeharms, 2006).

First child grid (Dx ~ 7.5km)

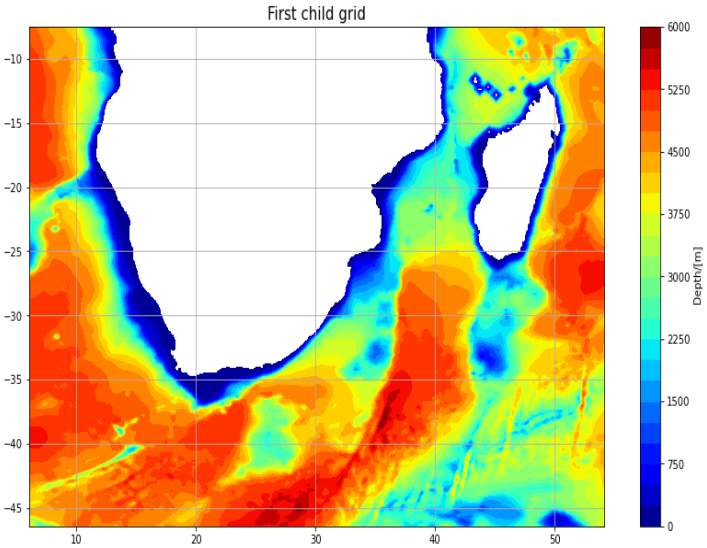

Figure 3.4: First child grid's bathymetry

The grid with a spacing of approximately 7.5 km was positioned at the southern tip of the African continent, spanning from 6◦E to 55◦E longitude and covering a broad region from the Equatorial (-7◦S) to the subpolar (-46◦S) latitudes. This grid was designed to replicate the behavior of the Agulhas Current within the South Indian Ocean subtropical gyre. It encompassed various source flows contributing to the Agulhas Current, including those originating from the Mozambique Channel, the eastern part of Madagascar, and the sub-gyre of the South-West Indian Ocean (Lutjeharms, 2006).

Second child grid (Dx ~ 2.5km)

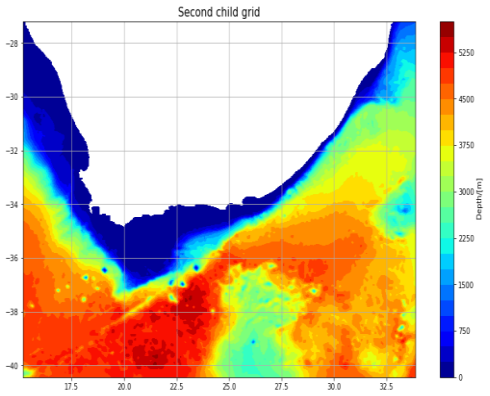

Figure 3.5: Second child grid's bathymetry

The grid with a spacing of approximately 2.5 km was centred on the highly dynamic Agulhas Current, recognized as one of the most intense western boundary currents in the Southern Hemisphere (Beal et al., 2015). It covered the entire trajectory of the Agulhas Current, starting from its source north of Durban (34° E ; -27° S) and extending to its Retroflection point (15° E ; -40°S), where it transformed into the Agulhas Return Current, denoted by purple features. With an effective resolution of approximately 10 times the grid spacing (10dx ~ 25 km) as indicated by Soufflet et al. (2016), this grid was well-suited for capturing the upwelling and the other mesoscale features in the Agulhas Current region.

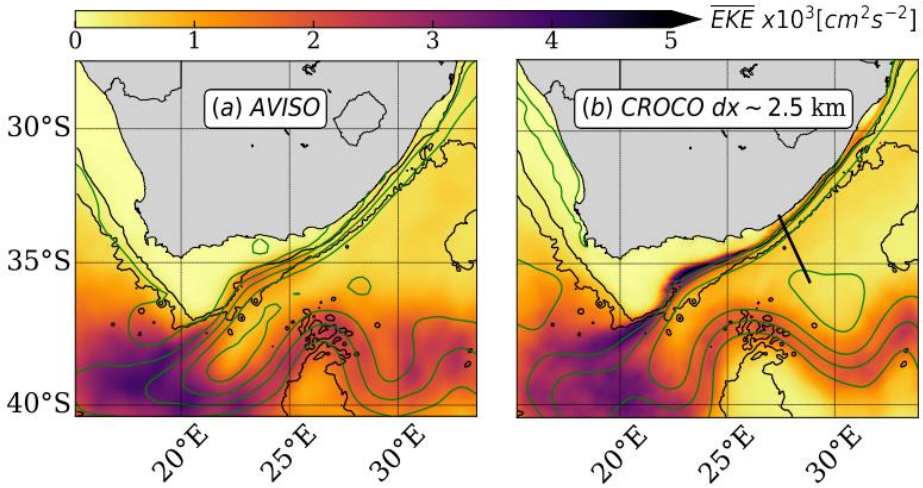

Figure 3.6: Comparison between mean Eddy Kinetic energy from AVISO (left) and 1/36 CROCO grid (right) (Tedesco et al, 2019)

The 1/36° CROCO grid has previously been used in other studies to resolve the dynamics in the Agulhas region. Tedesco et al (2019) compared the mean state of surface eddy kinetic energy of this grid with the one derived from remote sensing datasets of absolute dynamic topography gridded at a coarser resolution (1/4°) from AVISO. Tedesco et al (2019) noted that the observed and modelled EKE values did not show much similarity mostly upstream of 23°E, around the Agulhas Bank eastern margin whereby the 1/36° CROCO grid showed a higher EKE compared to AVISO.

3.2C Nesting procedure

In the case of the parent grid, first child grid, and second child grid, these simulations were run from an online 2-way embedded nesting process procedure (Debreu and Blayo, 2008; Debreu et al., 2012). The AGRIF tool of the model allowed different nesting levels to be set up through an online 2-way nesting process and proved to be useful for domains of high spatial resolution as it was able to resolve fine scale features within a low computational cost. The standard nesting procedure involved a full intersection between a child grid (dx ~ 7.5, 2.5km) embedded in the parent grid (dx ~ 22.5, 7.5km grids). Data was transmitted from the parent grid to the child grid as boundary conditions while data was also fed back to the parent grid as an update for the coarse resolution domain.

3.2D Momentum tracers numerical schemes and turbulent closures

Numerical methods for advection were employed based on finite differences, striking a balance between accuracy, typically associated with higher discretization orders, and computational efficiency. For the 3 nested grids, momentum advection was discretized using a third-order upwind biased advection scheme horizontally. Vertically, a semi-implicit scheme was utilized with adjustments made between explicit and implicit formulations to ensure model stability.

Regarding tracer advection in the same grids, a split and rotated third-order upwind-biased scheme on the horizontal plane was applied, along with a fourth-order compact scheme vertically. Separating the diffusive and advective components of the numerical scheme allowed for the reduction of diapycnal mixing by introducing dissipation along isopycnals, preserving water mass properties and enhancing simulation realism.

For the three nested grids, the K-profile parameterization (Large et al., 1994) played a role in the turbulent closure of the primitive equations. This parameterization determined the "eddy" (subgrid scale) viscosity parameter (KM) in surface and bottom boundary layers and in the ocean interior. The thickness of both boundary layers was computed based on an Ekman depth estimate and a Richardson number criterion, employing Lemarié et al. (2012)'s adaptation of the critical Richardson number

value (Ricr=0.15). In the bottom boundary layer, the K-profile exhibited a parabolic shape proportional to the boundary layer thickness, using Durski et al. (2004)'s adjustment.

3.2E Bathymetry and vertical grid

The bathymetric data for the 3 nested grids was derived from the General Bathymetric Chart of the Oceans with a 30-second resolution (Weatherall et al., 2015). The vertical grid structure comprised 60 σ levels, which followed the distribution method outlined by Haidvogel and Beckmann (1999). These levels underwent stretching at the surface (θs=5) and at the bottom (θb=0), with a transition depth occurring at hcline=10 m. However, it was worth noting that the terrain-following vertical coordinate system had a drawback in the form of pressure gradient errors. To mitigate these numerical errors, local smoothing of the topography was implemented whenever the steepness parameter ($r = \nabla H \, H$) exceeded a threshold of 0.2 (Beckmann and Haidvogel, 1993).

3.2F Surface boundary forcing

The four nested simulations were primarily forced at the surface using the Fairall et al. (1996) bulk formula, which relied on daily variables (such as temperature at 2 m, wind velocity components at 10 m, specific humidity, thermal and solar radiations, precipitation rate, and surface stress components) obtained from the global atmospheric re-analysis of ERA-Interim by ECMFW (Dee et al., 2011). This re-analysis, which was generated using a data assimilation system based on the 2006 version of the Integrated Forecasting System (IFS), provided a time series of daily atmospheric variables spanning from 1979 to 2019 at a spatial resolution of approximately 80 km. The wind forcing used relative winds, considering the current's impact on wind velocities, instead of absolute winds. This approach contributed to more realistic numerical simulations, particularly in terms of mesoscale eddies. Renault et al. (2017) demonstrated that using relative winds resulted in a weaker modelled mesoscale eddies energy reservoir compared to absolute winds, but it showed much similarity with observations. The effect on this energy reservoir was also linked to the stability of the current, reducing the number of premature retroflections.

At the grid's boundaries, the dynamical and state variables of the nested simulations (with grid spacings of approximately 7.5 and 2.5 km) were forced at every time step using data from the nearest parent grids (with grid spacings of approximately 22.5 and 7.5 km). The parent grid (with a grid spacing of approximately 22.5 km) was forced using oceanic re-analysis data from GLORYS (Ferry et al., 2012), obtained from the ORCA025 configuration of the NEMO model of a spatial resolution of 0.25°. To minimize discontinuities at grid interfaces, a sponge layer was implemented at the boundaries of the nested simulations. This sponge layer applied explicit horizontal dissipation and nudging conditions (Marchesiello et al., 2001). Following their initializations, the simulations having the lower resolution (with grid spacings of approximately 22.5 and 7.5 km) underwent a spin-up period of 3 years, while the simulation with a grid spacing of approximately 2.5 km underwent a 1-

year spin-up. After completing their spin-up phases, all three grids were run for a period of 2 decades (from 1993 to 2014).

3.2G Generalized Ekman pumping equation

We also computed the terms of the generalized Ekman pumping equations offline to compute the linear and non linear terms in chapter 6. This allows us to assess which term (planetary vorticity, advection of momentum, wind stress curl or viscous flux) is triggering more Ekman pumping. To derive this equation, we start with the momentum equations describing the dynamics of the ocean currents and continuity equations.

$$\frac{\partial \mathbf{u}}{\partial t} + \mathbf{u} \cdot \nabla \mathbf{u} + f\mathbf{k} \times \mathbf{u} = -\nabla \frac{P}{\rho_1} + \frac{\partial}{\partial z}\left(K_v \frac{\partial \mathbf{u}}{\partial z}\right) + A_h \nabla^2 \mathbf{u}$$
$$\frac{\partial u}{\partial x} + \frac{\partial v}{\partial y} + \frac{\partial w}{\partial z} = 0$$

whereby

$\frac{\partial \mathbf{u}}{\partial t}$ is the rate of change of velocity,

$\mathbf{u} \cdot \nabla \mathbf{u}$ is the advection term, representing the nonlinear advection of velocity

$f\mathbf{k} \times \mathbf{u}$ is the Coriolis term where f is the Coriolis parameter

$-\nabla \frac{P}{\rho_1}$ is the pressure gradient term divided by a reference density ρ_1

$\frac{\partial}{\partial z}\left(K_v \frac{\partial \mathbf{u}}{\partial z}\right)$ represents the vertical diffusion term due to viscosity K_v

$A_h \nabla^2 \mathbf{u}$ is the horizontal diffusion term and

$\frac{\partial u}{\partial x} + \frac{\partial v}{\partial y} + \frac{\partial w}{\partial z} = 0$ is the Continuity equation ensuring mass conservation.

These equations are then vertically integrated from the depth where we want to compute w (z = z0) to the surface (z = 0). The resulting equations for vertically integrated velocities, U and V, and the vertical velocity w(z0) at the specified depth z0 are obtained.

$$\overbrace{\frac{\partial U}{\partial t}}^{RATE} = \overbrace{fV}^{COR} \overbrace{- \int_{z_0}^{0} \vec{u}.\nabla u \, dz}^{ADV} \overbrace{- \int_{z_0}^{0} \frac{1}{\rho_0}\frac{\partial P}{\partial x} dz}^{PRSG} \overbrace{+ \frac{\tau_x}{\rho_0} - K_v \frac{\partial u}{\partial z}\Big|_{z_0}}^{VMIX} \overbrace{+ \int_{z_0}^{0} hdiff_u \, dz}^{HMIX}$$
$$\frac{\partial V}{\partial t} = -fU - \int_{z_0}^{0} \vec{u}.\nabla v \, dz - \int_{z_0}^{0} \frac{1}{\rho_0}\frac{\partial P}{\partial y} dz + \frac{\tau_y}{\rho_0} - K_v \frac{\partial v}{\partial z}\Big|_{z_0} + \int_{z_0}^{0} hdiff_v \, dz$$

whereby

$\frac{\partial U}{\partial t}$ represents the change in the vertically integrated eastward velocity over time

$\frac{\partial V}{\partial t}$ represents the change in the vertically integrated northward velocity over time

f represents the Coriolis parameter, which is a function of latitude and the Earth's angular velocity.

U represents the zonal (eastward) velocity component.

V represents the meridional (northward) velocity component.

$-\int_{z_0}^{0} \mathbf{u} \cdot \nabla u \, dz$ represents the advection of eastward momentum integrated over the water column

$-\int_{z_0}^{0} \mathbf{u} \cdot \nabla v \, dz$ represents the advection of northward momentum integrated over the water column

$-\int_{z_0}^{0} \frac{1}{\rho_0} \frac{\partial P}{\partial x} \, dz$ accounts for the pressure gradients in the eastward direction integrated over the water column

$-\int_{z_0}^{0} \frac{1}{\rho_0} \frac{\partial P}{\partial y} \, dz$ accounts for the pressure gradients in the northward direction integrated over the water column

$\frac{\tau_x}{\rho_0}$ represents the zonal component of surface wind stress.

$\frac{\tau_y}{\rho_0}$ represents the meridional component of surface wind stress

$K_v \frac{\partial u}{\partial z}$ represents the vertical diffusion of eastward momentum

$K_v \frac{\partial v}{\partial z}$ represents the vertical diffusion of northward momentum

$\int_{z_0}^{0} hdiff_u \, dz$ represents the vertical integral of horizontal diffusion coefficient for the u-component of velocity.

$\int_{z_0}^{0} hdiff_v \, dz$ represents the vertical integral of horizontal diffusion coefficient for the v-component of velocity.

By taking the curl of these equations and dividing by the Coriolis parameter (f), the following equations are established.

$$w(z_0) = \overbrace{-\frac{1}{f}\frac{\partial}{\partial t}\nabla \times U}^{-\frac{\nabla \times RATE}{f}} - \frac{\beta V}{f} \overbrace{-\frac{\nabla}{f} \times \int_{z_0}^{0} \vec{u}.\nabla\vec{u}\, dz}^{\frac{\nabla \times ADV}{f}} + \frac{\nabla \times \tau}{\rho_0 f} + \frac{\nabla \times KFLX}{f} + \frac{\nabla \times HMIX}{f}$$

$-\nabla f \times \int_{z_0}^{0} \mathbf{u} \cdot \nabla \mathbf{u}\, dz$ represents the advection of vorticity by the horizontal velocity field

$-\frac{\beta V}{f}$ accounts for the contribution of the Earth's rotation to vorticity

$-\frac{\nabla}{f} \times \int_{z_0}^{0} \vec{u}.\nabla\vec{u}\, dz$ represents the curl of the advection of momentum

$\frac{\nabla \times \tau}{\rho_0 f}$ represents the wind stress curl,

$\frac{\nabla \times (K_{fLX})}{f}$ denotes the contribution of horizontal mixing of momentum, to the vorticity in the ocean, normalized by the Coriolis parameter f.

$\frac{\nabla \times (HMIX)}{f}$ represents the vorticity generated by horizontal mixing of momentum, HMIX, in the ocean, cross product with the Coriolis parameter.

Upon neglecting the horizontal mixing (HMIX) and rate of strain (RATE) terms, the final equation for generalized Ekman pumping is obtained:

$$\underbrace{w(z_0)}_{Pumping} = -\underbrace{\frac{\beta V}{f}}_{Planetary} + \underbrace{\frac{\nabla \times \tau}{\rho_0 f}}_{WindCurl} + \underbrace{\frac{\nabla \times ADV}{f}}_{Inertia} + \underbrace{\frac{\nabla \times KFLX}{f}}_{ViscousFlux}$$

This equation represents the dominant terms influencing vertical pumping at the specified depth z0, whereby

the planetary vorticity term $-\frac{\beta V}{f}$ accounts for the contribution of the Earth's rotation to vorticity,

$\frac{\nabla \times \tau}{\rho_0 f}$ represents the wind stress curl,

$\frac{\nabla \times ADV}{f}$ accounts for the advection of momentum (inertia) contributing to vorticity

$\frac{\nabla \times KFLX}{f}$ describes the curl of the vertical viscosity multiplied by the northward velocity. This term represents the contribution of the viscous flux (associated with friction) to vorticity

3.3 Highlights

As an overall, we described the different datasets and methods which were adopted in this study. Some of the main highlights of this chapter included:

- We used the temperature and salinity data from observational datasets such as CARS09, WOA2018 and OSTIA.
- We used 3 different grids from CROCO simulations (22.5km, 7.5 and 2.5 km spatial resolution and 60 vertical levels) and the time period is from 1993 to 2014.
- We also computed the generalized Ekman pumping equation to assess the linear and non linear terms in chapter 6.

3.6

Chapter 4: Spatial and temporal characteristics of Port Alfred upwelling

In this chapter, we address the 1st research question:

What are the spatial and temporal characteristics of the Port Alfred upwelling?

4.0 Revisiting Port Alfred upwelling

There have been many challenges why it has taken so long to explore this upwelling in depth. Most research in this area has focused on either the northern or southern components of the Agulhas region. Consequently, the Port Alfred upwelling, located between these boundaries, has often not been explored in depth in the literature. This upwelling zone ranged from 15 to 100km and required high resolution datasets to be understood thoroughly. Most of the research cruises were not always sampling at a high resolution. There has also been a lack of high resolution numerical models.

Despite the existing literature, the picture painted on the mechanisms behind the Port Alfred upwelling was only from analytical models, *in situ* data and remote sensing datasets while numerical modelling has not yet been utilized to investigate this upwelling thoroughly. Exploring several ocean properties generated from the numerical model through the lens of varying temporal scales could contribute to a better understanding of the spatial and temporal characteristics of an upwelling like Port Alfred. For instance, computing its average sea surface temperature would allow us to see whether there was a strong upwelling signature during the mean state. This would also provide a baseline against which we could compare variations in upwelling intensity and assess whether the upwelling was anomalously strong or weak. Its seasonal state would allow us to determine the seasonal variability of the upwelling, which would be crucial for understanding its annual patterns and how the upwelling was responding to changes in seasonal wind patterns. A climatological monthly mean would also prove to be useful to understand the upwelling conditions on a month-to-month basis. We could also investigate its interannual mean state to explore whether the upwelling showed a long-term variability. This would help us detect any trends or anomalies. For example if other phenomenon such as climate change, El Niño or the Benguela Niño was weakening the Agulhas Current, this would be revealed in the possible weakening of the upwelling. Focusing only on events when the upwelling was most pronounced would also allow us to understand the dynamics and characteristics of these events more precisely as in this case the non-favourable upwelling conditions would be filtered.

Hence assessing the signature of the upwelling through these different temporal scales would provide a better description of the characteristics of this upwelling.

4.1 Aims of study

In this chapter, we aimed at providing a more detailed description of the spatial and temporal characteristics of the Port Alfred upwelling through its temperature, salinity and vertical velocity from a numerical modelling approach by answering 4 research questions:

4.1A Does the Port Alfred upwelling influence the mean state?

We computed the mean state of temperature, salinity and vertical velocity from varying resolutions to detect whether it would capture any signature of the upwelling.

4.1B Does the upwelling display a strong seasonal signal?

We computed the seasonal state of temperature, salinity and vertical velocity using the second child grid to observe whether it displayed a strong seasonal signal.

4.1C When do these upwelling events occur?

We used two upwelling indices derived from the sea surface temperature to locate upwelling events. We also used the vertical velocity as an upwelling indicator.

4.1D Focussing on upwelling events only, what deductions can be made?

We explored the upwelling from a different temporal scales. We computed the average conditions of the temperature, salinity and vertical velocity from the selected upwelling events only. We also chose to focus on 4 case studies based on the different hypotheses.

4.2 Data and methods

In this chapter, we used the model generated temperature, salinity and vertical velocity for each grid (spatial resolution 22.5km, 9km, 2.5km). Additionally, we also used the temperature and salinity fields from other observational datasets such the CARS09 (spatial resolution 50km), WOA2018 (spatial resolution 25km) and remote sensing dataset OSTIA (spatial resolution 4km).

For the mean state, the average from 1993 to 2014 was calculated for each model grid as well as for the OSTIA dataset. For the WOA2018 dataset, an average of 6 decadal climatologies (1955-2018) for the temperature and salinity field are calculated. These averages were also computed for the CARS09 dataset. We looked at its seasonality and monthly average as well. Summer is defined as an average of January, February and March and winter as July, August and September. To inspect its seasonal signal even further we performed a classical additive decomposition of the sea surface temperature from each dataset by decomposing the daily temperature into its trend, seasonal and residual component to assess whether it had a regular seasonal pattern and any irregular influences.

We also explored possible methods to detect upwelling events in the second child grid. We used 2 sea surface temperature derived upwelling indices, the adapted Demarq's coastal upwelling index and the residuals of sea surface temperature. We assessed the relationship between sea surface temperature and vertical velocity to see if model-derived vertical velocity was a good indicator of upwelling. We measured the correlation between these two fields and compared the residuals for each field to see if they both could detect upwelling events.

After the detection of upwelling events, we could assess the sea surface temperature, vertical section of temperature, sea surface salinity and vertical velocity at different temporal scales such as the average conditions during upwelling events only and singular upwelling events. Using the cold events detected from the residuals of temperature, we computed the mean state of all the upwelling events. We also chose 4 upwelling events to explore more in depth, whereby each upwelling event was linked to a different potential driving mechanism.

4.3 Mean state

4.3A Temperature properties

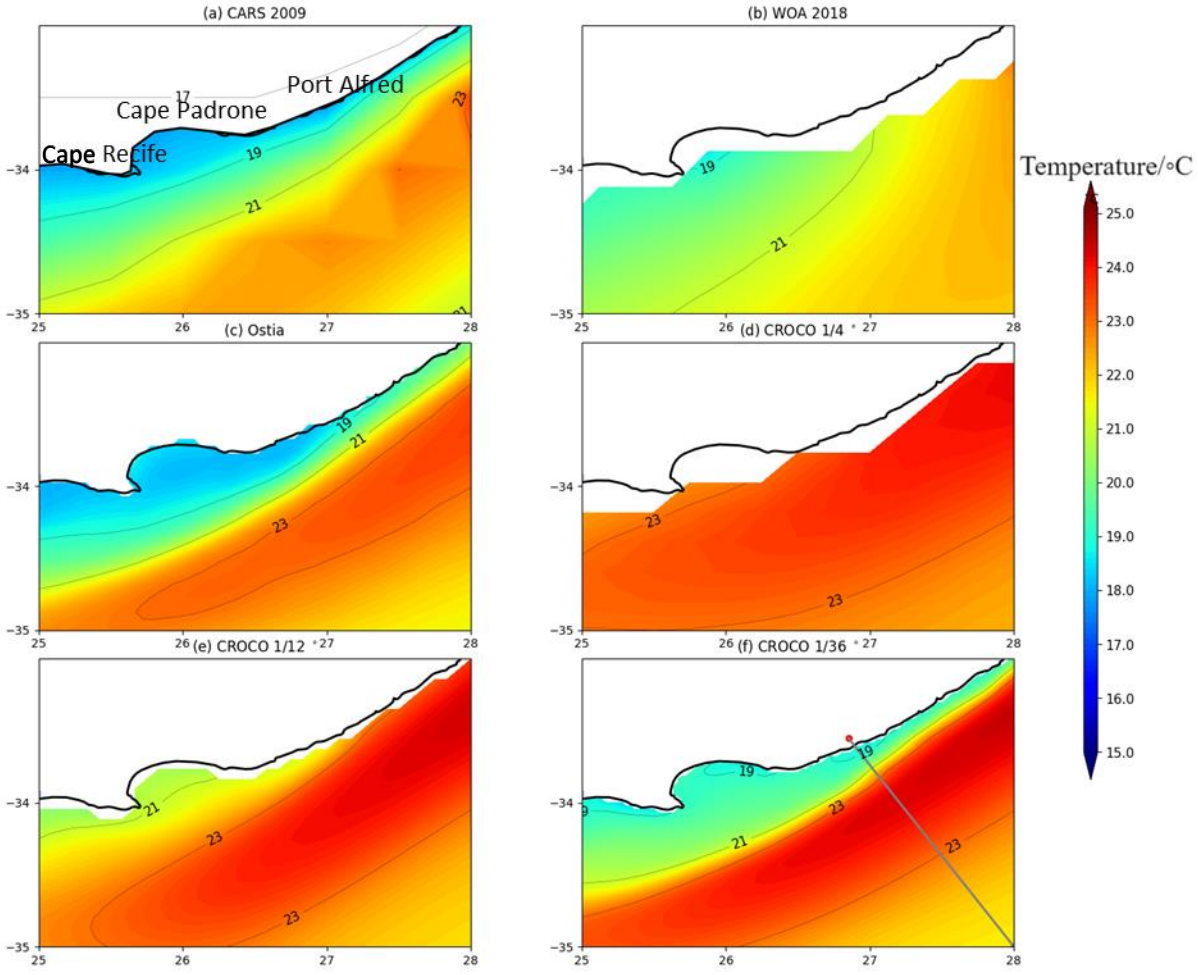

Figure 4.1: Mean sea surface temperature of (a) CARS09 dataset, (b) WOA2018 dataset, (c) OSTIA dataset, (d) Parent grid (CROCO 1/4°), (e) First child grid (CROCO 1/12°) and (f) Second child grid (CROCO 1/36°). The black line in 4.1 (f) is the zone along which the transect was chosen.

Horizontal spatial resolution

To test the representation of the upwelling from different spatial resolutions, we plotted the mean sea surface temperature from the observational datasets CARS09, WOA2018 and OSTIA as well as the CROCO simulations 1/4°, 1/12° and 1/36° in Figure 4.1. This region is known to have a strong temperature signature, due to the current's position which is close to its core (Krug and Tournadre, 2012), hence making the sea surface temperature a suitable field to evaluate the model simulations compared to the reliable and well observed datasets. We also displayed some isotherms on the maps to provide points of reference. The water temperature for the CARS09 dataset was about 19°C near the coastline and the Agulhas Current was delineated by an isotherm of 21°C with a warmer temperature of 23°C in its core. The WOA2018 also showed a colder temperature of 19°C near the coastline and a gradual increase towards the region of the current. Due to the coarse resolution of these datasets (50km and 25km), a smoothing was applied near the coastline. The OSTIA dataset, having a higher resolution of 4km, showed a sharper delineation of the boundary of the current from 19°C along the coastline to 21°C. The isotherm 23°C highlighted the demarcation of the warmer core from the colder and more dispersed current. The core of the current for OSTIA extended south but is recorded to be much colder compared to the CROCO simulations. The numerical model outputs displayed a much warmer sea surface temperature compared to the observational datasets, with a warmer core of the current extending further south. The CROCO 1/4° grid showed a more dominant warmer temperature and the coarse resolution failed to capture the upwelling signal and was clearly unable to resolve the upwelling dynamics along the coastline. In the 1/12° CROCO grid, even if the Agulhas front was well defined, it was hard to find an upwelling signature with a spatial resolution of 7.5km as it was marked by warmer temperature at the coast recording 23°C at Port Alfred and 21°C at Cape Padrone and Cape Recife. As for the 1/36° CROCO grid, it was in agreement with the OSTIA, CARS09 and WOA2018 datasets with a temperature of 19°C along the coastline, allowing us to capture a strong upwelling signal during the mean state at Port Alfred as well as Cape Padrone and Cape Recife. The front was much warmer compared to the observational datasets and characterized by a temperature of 21°C at its edges and 23°C at its core.

.

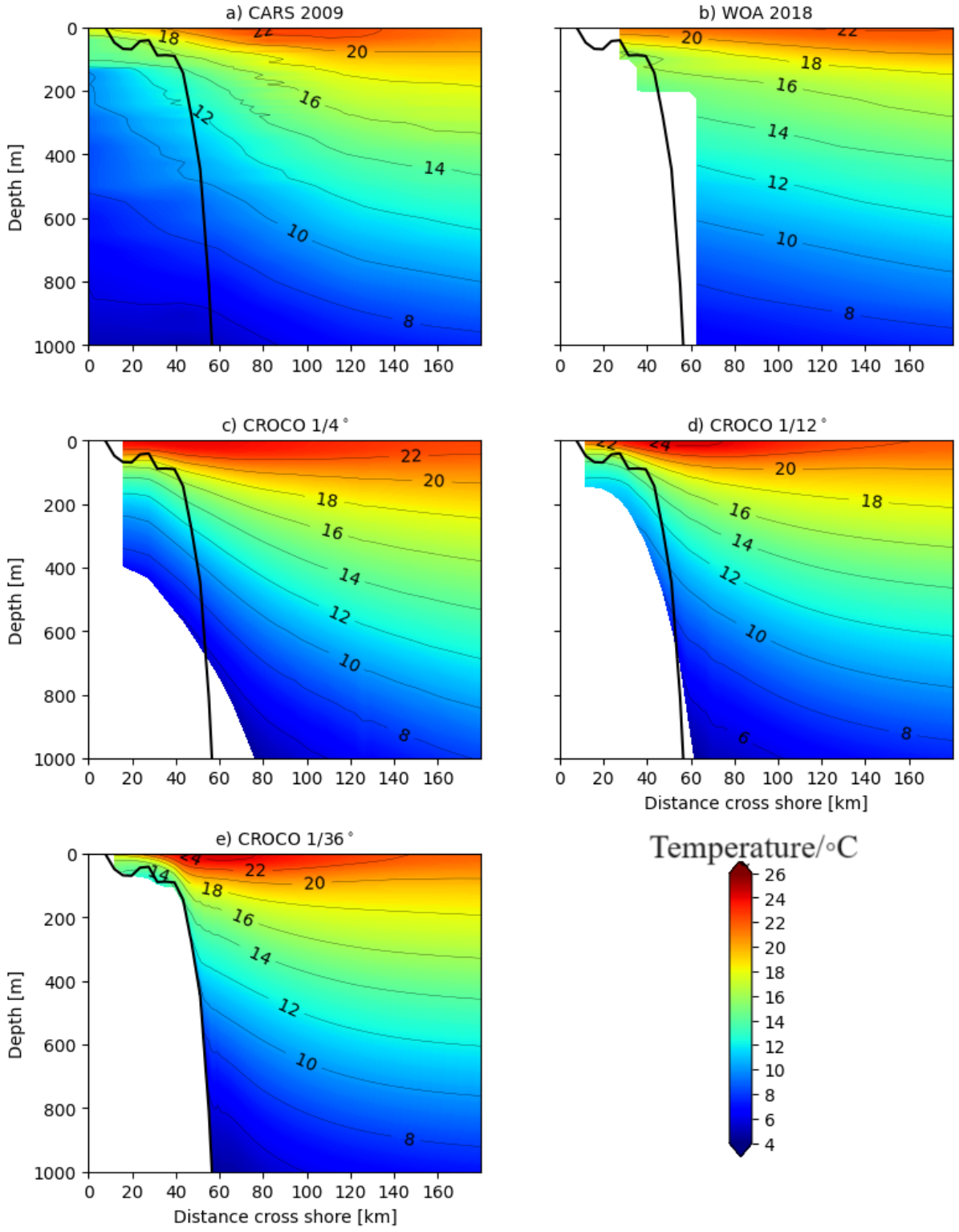

Figure 4.2: Mean vertical temperature of (a) CARS09 dataset, (b) WOA2018 dataset, (c) Parent grid (CROCO 1/4°), (d) First child grid (CROCO 1/12°) and (e) Second child grid (CROCO 1/36°).

In Figure 4.2, we test the influence of horizontal resolution on the representation of the upwelling, by plotting the 3 CROCO model grid as well as the CARS09 and WOA2018 dataset during the mean state of the vertical temperature distribution along a transect from Figure 4.1(f). CARS09 and

WOA2018 showed a presence of the Agulhas Current and recorded a temperature ranging from 20 to 22°C in the first 100m. However both these datasets included much smoothing and failed to delineate the seafloor due to their coarse resolution. The CROCO grids showed a much warmer temperature in the first 100m compared to the observational datasets. The Agulhas Current was marked by a temperature of 22°C in the three CROCO grids in the surface layer, but only extended till 160km in the 1/4° CROCO grid. A higher temperature of 24°C was more defined in the 1/36° CROCO grid and extended only till 80m from Port Alfred. Isotherms of 14°C could be observed on the shelf in the 1/12° and 1/36° CROCO grid. These two CROCO grids were able to capture the upwelling signature during the mean state although the presence of the current and the upwelling was more pronounced in the 1/36° CROCO grid.

4.3B Salinity properties

Influence of spatial resolution

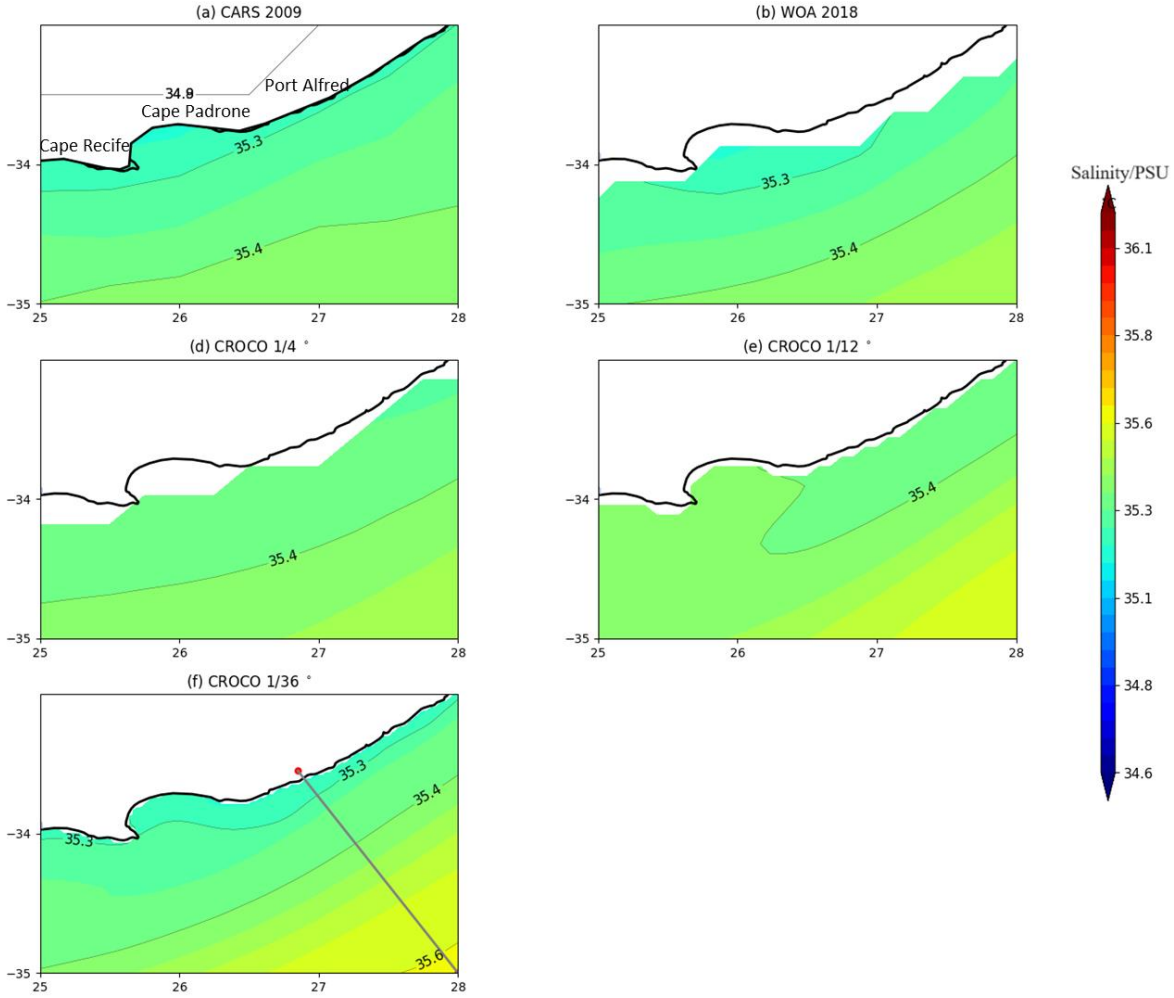

Figure 4.3: Mean sea surface salinity of (a) CARS09 dataset, (b) WOA2018 dataset (c) Parent grid (CROCO 1/4°), (d) First child grid (CROCO 1/12°) and (e) Second child grid (CROCO 1/36°). The black line in 4.3 (e) is the zone along which the transect was chosen.

Figure 4.3 illustrates the daily mean sea surface salinity for the years 1993-2014 for the CARS09, WOA2018 dataset and 1/4°, 1/12° and 1/36° CROCO grids. Closer to the coast, lower sea surface salinity was observed in all the datasets, but the variation was more pronounced in the CARS09, WOA2018 datasets and the 1/36° CROCO grid recording a salinity of 35.3 PSU in the upwelling region. Much saltier waters were observed offshore in the 1/12° and 1/36° CROCO grid, reaching a peak of 35.6 PSU at the offshore region. While the 1/36° CROCO grid had the highest resolution, it did not delineate the current through its salinity and instead it showed a gradual increase in salinity from the coast to the offshore region. The coarser spatial resolution of the 1/4° CROCO grid was not reliable to resolve the mesoscale variability and the Port Alfred upwelling. As for observational datasets, the resolution close to the coast was too coarse to resolve the current and the upwelling. On the overall, the CROCO grids recorded a higher salinity compared to the observation datasets. This is probably due to the absence of river discharge in the CROCO simulations which can be a factor to prevent the model from resolving the surface salinity.

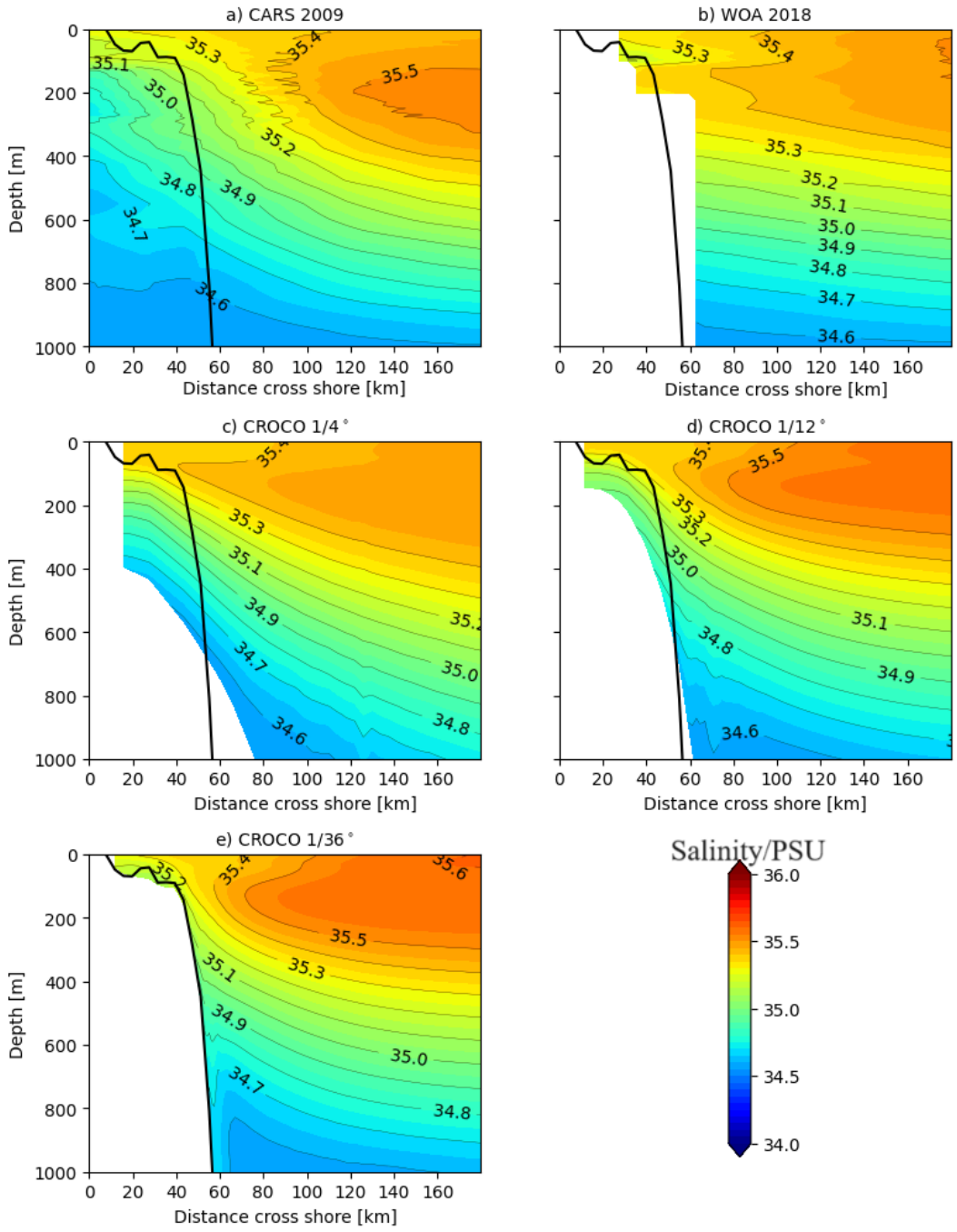

Figure 4.4: Mean vertical salinity of (a) CARS09 dataset, (b) WOA2018 dataset, (c) Parent grid (CROCO 1/4°), (d) First child grid (CROCO 1/12°) and (e) Second child grid (CROCO 1/36°).

In order to test the influence of horizontal resolution on the representation of the upwelling, Figure 4.4 shows the 3 CROCO model grid as well as the CARS09 and WOA2018 dataset during the mean state of the vertical salinity distribution along a transect from Figure 4.3 (e). CARS09 and WOA2018 showed fresher waters on the shelf and a higher salinity ranging from 35.3 to 35.5 PSU from the surface to a depth of 400m despite their coarse resolution and high smoothing. In the first 200m, the water masses which dominated these regions were generally the Tropical Indian Surface Water

(TSW) and South Indian Subtropical Surface Water (STSW). The 1/4° CROCO grid, having a coarse resolution, showed the presence of the current from its higher salinity from a depth of 400m to the surface. An increase in the resolution improved the representation of the current as well as the upwelling in the vertical structure. The shelf waters were marked by a salinity of 35.3 PSU in the 1/12° CROCO grid and 35.2 PSU in the 1/36 CROCO grid. In the deeper layers, the salinity was marked 34.7 PSU to 35.1 PSU was generally known to be the South Indian Central Water (SICW) (Lutjeharms, 2006). As an overall, the 1/36° CROCO grid seemed to be in agreement with the CARS09 and WOA2018 datasets. Each dataset was able to capture the strong presence of the Agulhas Current from its high salinity content. A strong signature of the upwelling could also be observed by the low salinity of the shelf waters in the 1/36° CROCO grid and CARS09 datasets.

4.3C Vertical velocity properties

Influence of horizontal spatial resolution

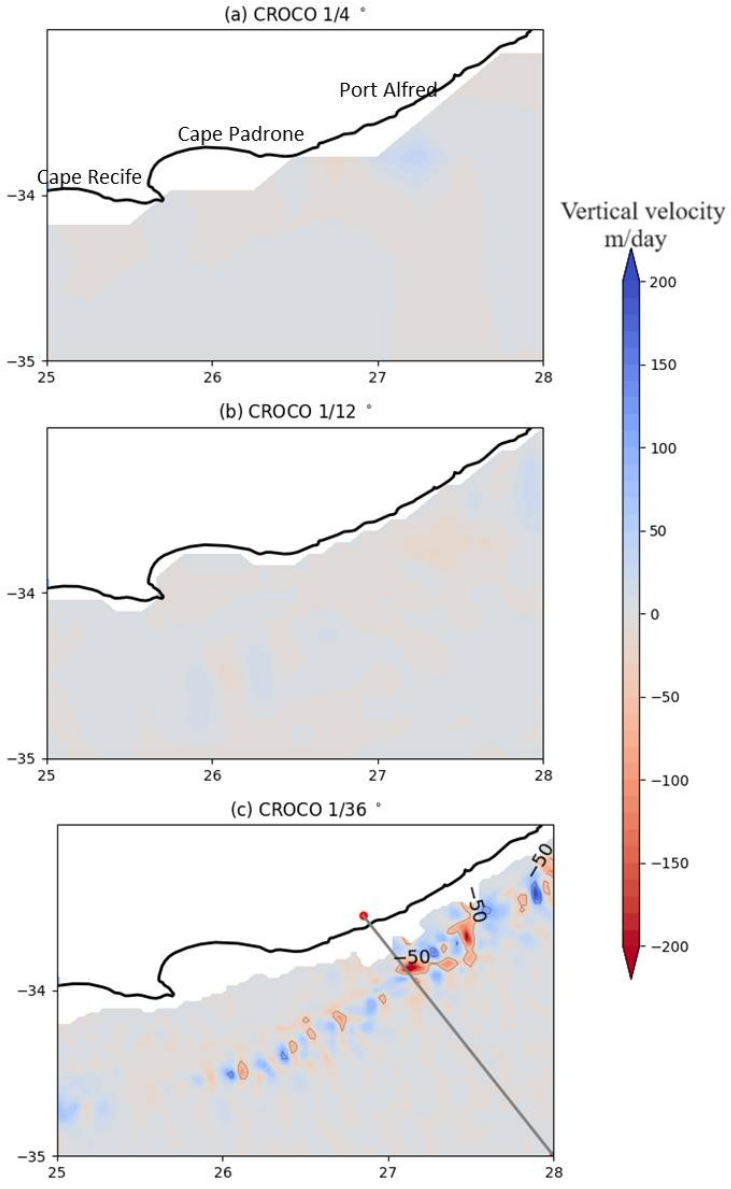

Figure 4.5: Mean vertical velocity at a depth of 75m of (a) Parent grid (CROCO 1/4°), (b) First child grid (CROCO 1/12°) and (c) Second child grid (CROCO 1/36°). The black line in 4.5 (c) is the zone along which the transect was chosen.

In Figure 4.5, we tested the influence of spatial resolution during the mean state of the vertical velocity from the 1/4°, 1/12° and 1/36° CROCO simulations at a depth of 75m to detect whether it could capture the representation of the upwelling. The vertical velocity signal exhibited a significant amount of noise at that depth in each CROCO simulation. The 1/4° and 1/12° CROCO grids failed to delineate the changes in bathymetry at 100m and did not show much variation in the vertical velocity. Hence it could not resolve the upwelling dynamics at this depth. The 1/36° CROCO grid could outline the seafloor on the continental shelf. Closer to Port Alfred, it had small pockets with a high variation of vertical velocity ranging between -50 and 50 m/day in the region of current. There was a much lower variability of vertical velocity further south at Cape Recife.

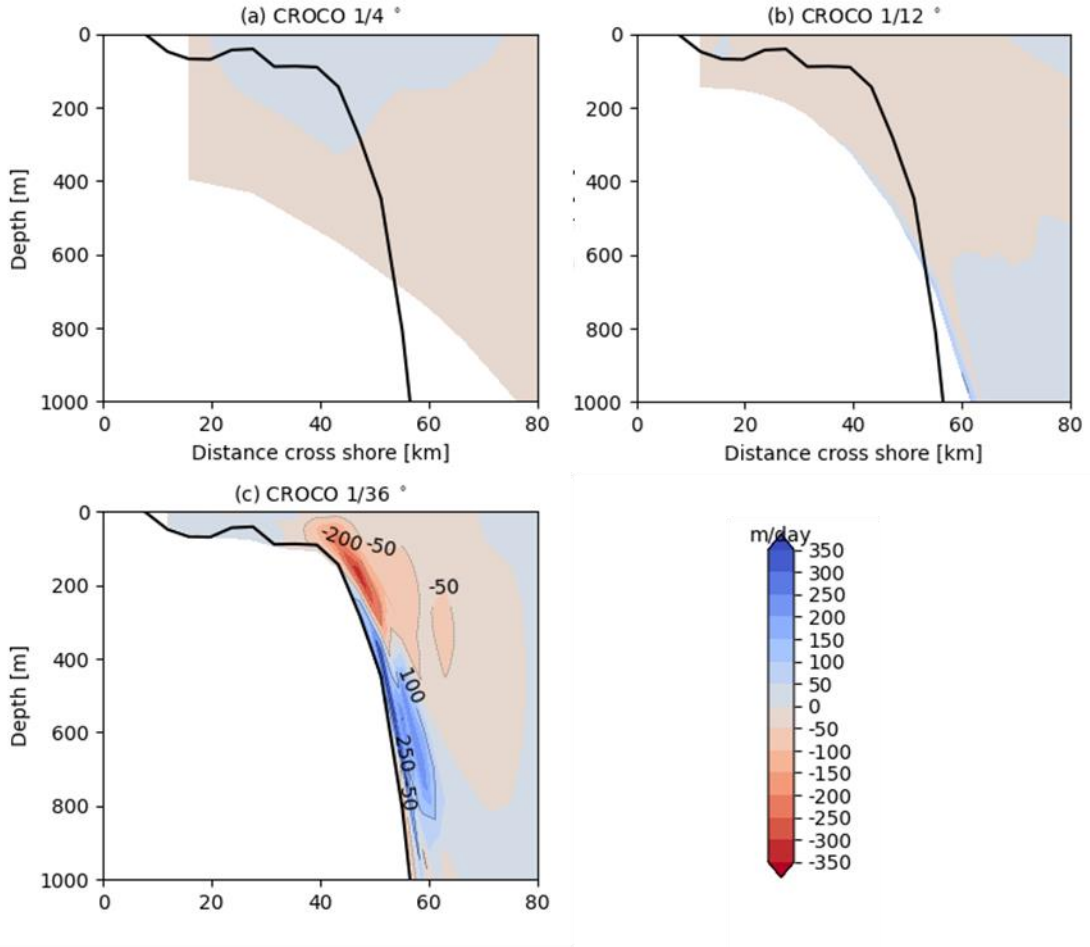

Figure 4.6: Mean vertical velocity of (a) Parent grid (CROCO 1/4°), (b) First child grid (CROCO 1/12°) and (c) Second child grid (CROCO 1/36°).

In Figure 4.6, we tested the influence of horizontal resolution of the vertical velocity during the mean state from the 1/4°, 1/12° and 1/36° CROCO simulations to detect whether it could capture the representation of the upwelling. An increase in resolution showed a major difference in the vertical distribution of the velocity. Using the bathymetry line from GEBCO as a baseline, the 1/4° CROCO grid could not resolve the vertical velocity closer to the coast. The 1/12° CROCO grid captured a slight negative vertical velocity from the surface to a depth of 600m in the Agulhas Current zone. The negative velocity is due to the presence of the Agulhas Current which is associated with convergence. The remaining areas had a positive vertical velocity ranging from 0 to 50m/day. The 1/36° CROCO grid was characterized by a much sharper negative velocity from 100m to 300m in the Agulhas Current zone along the continental slope, reaching a minimum of -200 m/day. From a depth of 400m to 800m, we are able to capture the strong positive vertical velocity along the continental slope, peaking till 250m/day. This implies that the upwelling due to the detachment of the current and bottom Ekman veering in the bottom boundary layer is strongly captured at a depth from 400 to 800m during its mean state.

4.4 Seasonality of Port Alfred upwelling region

After computing the mean state, we noted that the 1/36° CROCO grid was able to resolve the current better than the other grids and datasets. In this section, we focused on a different temporal scale and explored the seasonality of the temperature, salinity and vertical velocity of the 1/36° CROCO grid in order to understand whether the upwelling had a strong seasonal signal.

4.4A Temperature

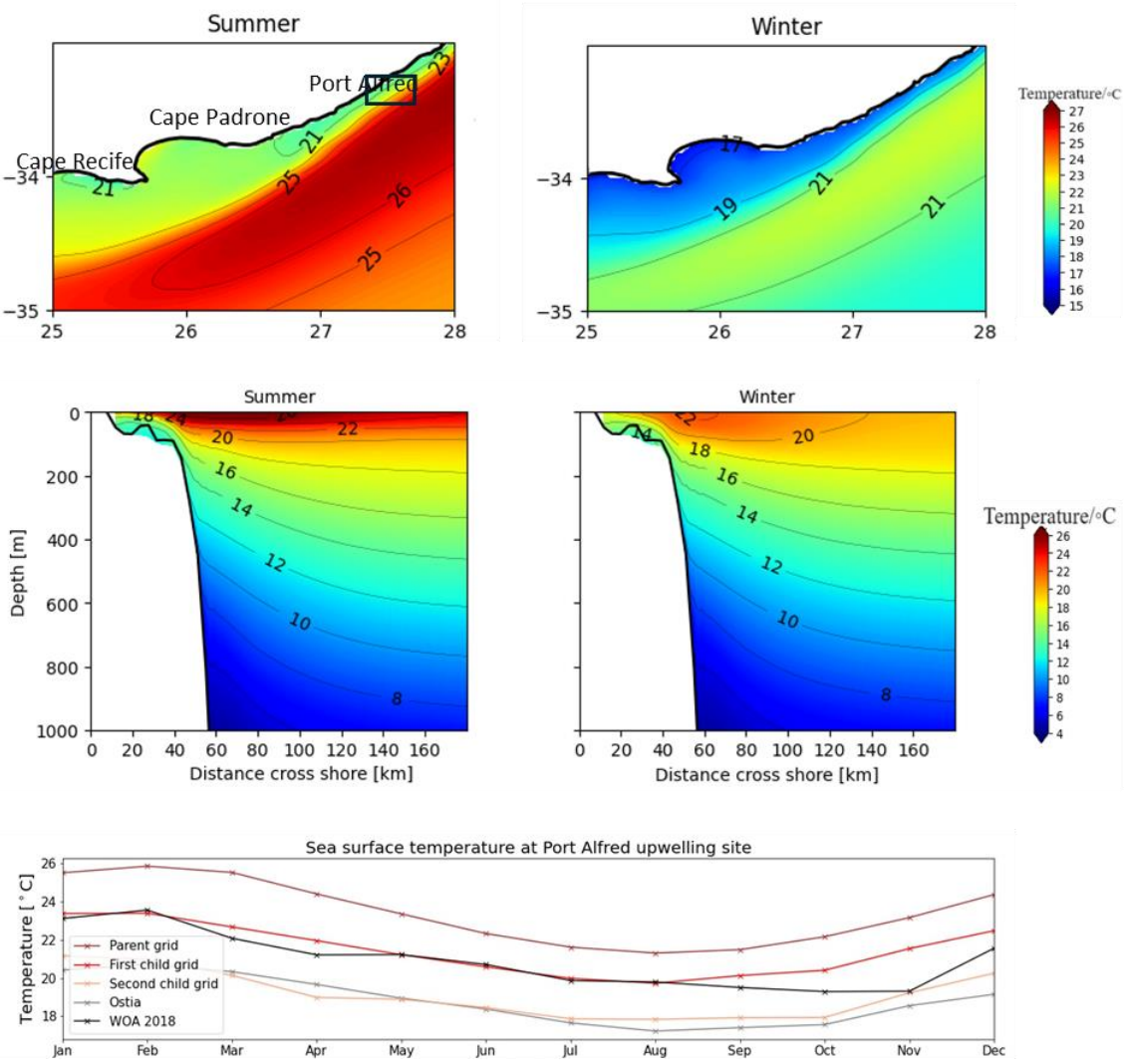

Figure 4.7: 1st row (left to right) - summer and winter sea surface temperature, 2nd row (left to right) – vertical temperature for summer and winter, 3rd row – monthly mean of sea surface temperature. The box represents the Port Alfred upwelling zone which is averaged for the time series.

Figure 4.7 illustrates the sea surface temperature and vertical distribution for summer and winter. It also shows the climatological monthly mean of temperature in the Port Alfred upwelling zone from the observational datasets of WOA2018 and OSTIA dataset as well as the 1/4°, 1/12° and 1/36° CROCO grids. In summer, a strong presence of the current was characterized by a temperature of 27°C at the core, and ranging from 25°C to 27°C while the current had weakened in winter, ranging from 21°C to 23°C. In the Port Alfred upwelling zone, the temperatures are much lower at the coast ranging from 17°C to 19°C in winter compared to temperatures ranging from 19°C to 21°C in summer. The vertical temperature also showed that summer displayed a strong presence of the current. From a depth of 100m to the surface, the temperature ranged between 22°C to 26°C in summer while it ranged from 20°C to 22°C in winter. We could observe an isotherm of 10°C on the

shelf during summer compared to an isotherm of 14°C in winter. This would indicate a stronger upwelling in summer, possibly due to the current. The climatological monthly mean of each dataset was also computed. Each dataset identified February as the hottest month and August as the coldest one. The maximum difference between the second child grid and OSTIA was less than 1°C and for most months they displayed relatively the same temperature values, ranging from 17° to 21°C. The WOA2018 and the 1/12° CROCO grid also displayed similar temperature most of the times, but both were at least 2°C hotter than the 1/36° CROCO grid and OSTIA. As for the 1/4° CROCO grid, it was likely that it was overestimating the Port Alfred upwelling region with temperatures ranging approximately from 22° to 26°C. On a seasonal scale, while the temperature was colder at the surface in the upwelling zone in winter, this would not necessarily imply that the upwelling had a seasonal signal. Since the vertical structure of the temperature revealed a colder temperature in summer, it was likely that the upwelling triggered by the current was more pronounced in summer. However, the seasonality of other atmospheric and oceanographic properties would need to be investigated thoroughly in order to have a better understanding.

Decomposition of sea surface temperature

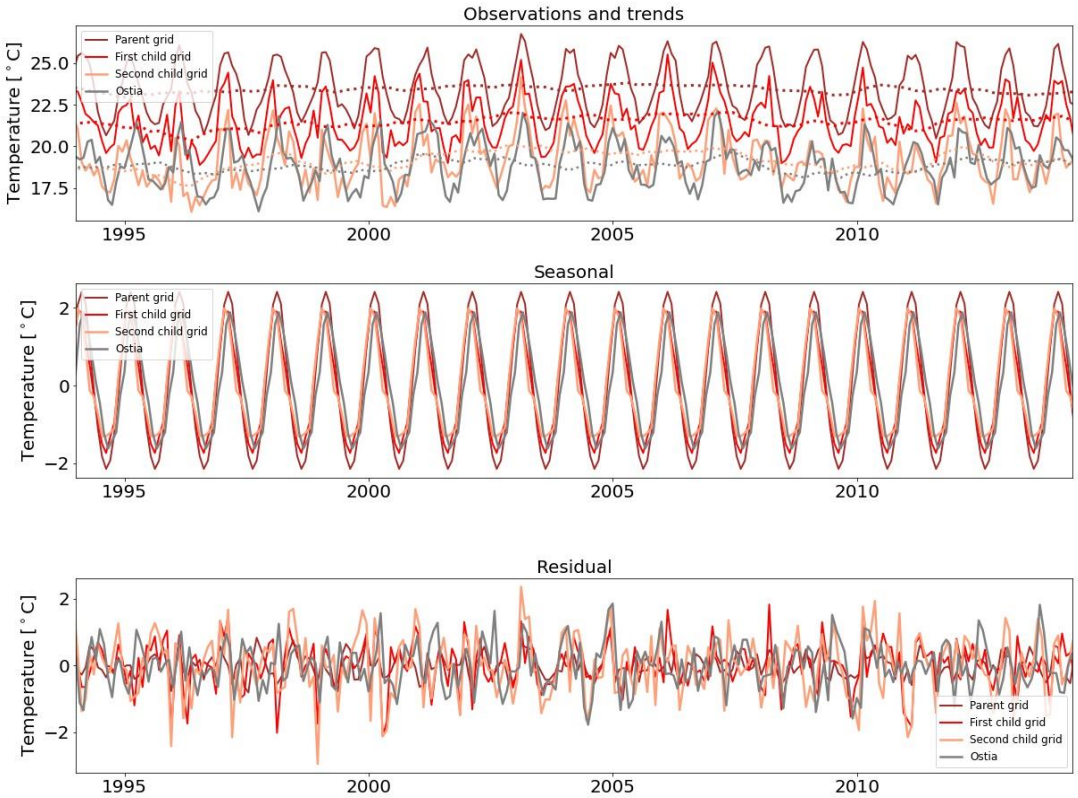

Figure 4.8: Decomposition of sea surface temperature of parent, first child, second child grid and OSTIA dataset. First row: Observations and trends. Second row: Seasonality. Third row: residuals of temperature.

Figure 4.8 shows a classical decomposition of the sea surface temperature from the parent, first child, second child grid and the OSTIA dataset from 1994 to 2014 into its observations, trend, seasonal and residual components. This method is used in time series analysis to break down a series into its fundamental components: (1) Trend: Long-term progression of the series. (2) Seasonal: Regular pattern repeating over fixed periods. (3) Residual: Random variation that cannot be attributed to trend or seasonality. In the case of sea surface temperature, this approach can be particularly useful to identify underlying patterns.

The parent grid ranged from 21°C to 26°C, the first child grid ranged from 19°C to 23°C, the second child and the OSTIA dataset ranged from 16°C to 22°C. For each dataset, the presence of a relatively straight line around 23 °C (parent grid), 21 °C (first child grid), 19.5°C (second child grid) and 18.5°C (OSTIA) in the trend component indicated a bias. While on the overall, an overestimation of the temperature was found in the parent and first child grid, the second child grid and the OSTIA dataset displayed relatively similar values.

As for the seasons graph, the seasonal component captured the regular, periodic fluctuations in the data that occur over shorter time intervals, often associated with the changing seasons. The oscillation ranged between -2°C and 2°C for the parent grid and ranged between -1.8°C to 1.8°C for the first child, second child and OSTIA dataset. This suggested a consistent repeated seasonal pattern in temperature.

The residual component represented the variability in the data that encompassed everything except the seasonal cycle, thus capturing the influence of intraseasonal and (sub)mesoscale activity on sea surface temperature. These variations are not inherently unpredictable; for example, they could be influenced by wind variability. In this graph, the residuals for the parent grid and the first child grid varied from -1°C to 1°C, while the second child grid and the OSTIA dataset showed higher variations, peaking at 2°C and sometimes decreasing to -2.5°C. The residuals for each dataset did not follow a constant pattern. This suggested that there were unpredictable fluctuations in SST that were not accounted for by the trend or the seasonal variations. These fluctuations could be due to various factors such as strong upwelling events, marine heat wave events or other irregular influences.

4.4B Salinity

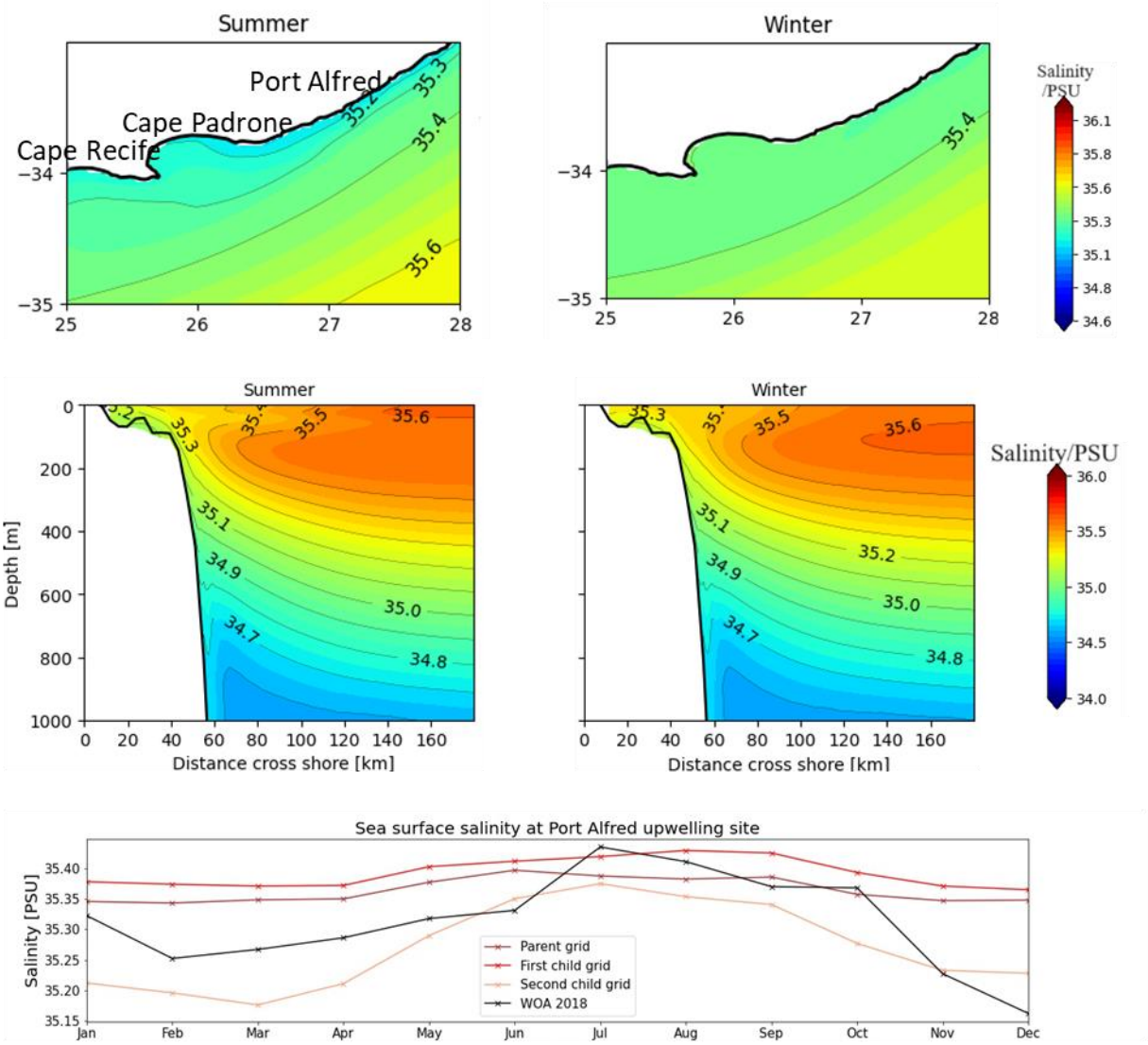

Figure 4.9: 1st row (left to right) - summer and winter sea surface salinity, 2nd row (left to right) – monthly mean of sea surface salinity

Figure 4.9 illustrates the sea surface salinity and vertical distribution of salinity for summer and winter. It also shows the climatological monthly mean of salinity in the Port Alfred upwelling zone from the WOA2018 dataset, 1/4°, 1/12° and 1/36° CROCO grids. In summer, we noted a higher salinity in the region of the current, ranging from 35.4 PSU to 35.6 PSU and more fresher waters at the coast ranging from 35.2 PSU to 35.3 PSU, while winter was characterized by a salinity ranging from 35.4 PSU to 35.5 PSU in the current zone and a salinity of 35.3 in the upwelling zone. We observed fresher waters with a salinity of 35.2 PSU on the shelf compared to a salinity of 35.3 PSU in winter. The climatological monthly mean of sea surface salinity was plotted for each dataset in the region of the upwelling. Each dataset identified a high salinity in winter and low salinity in summer.

The vertical structure of the Since the upwelling was characterized by a lower salinity, this indicated more upwelling in summer possibly linked to the strong presence of the Agulhas Current compared to winter. It must also be noted that there was more rainfall during the summer months in this region, hence leading to a lower salinity from an input of freshwater from rivers in the region. The second child grid varied approximately from 35.15 to 35.35 PSU while the coarser resolution grids of the model overestimated the salinity levels, ranging from 35.35 to 35.45 PSU. Even if the numerical model did not include the river discharge in the configurations, there was not a big difference between the observations and model outputs. The maximum difference between the highest resolution model output and WOA2018 was less than 0.20 PSU.

4.4C Vertical velocity

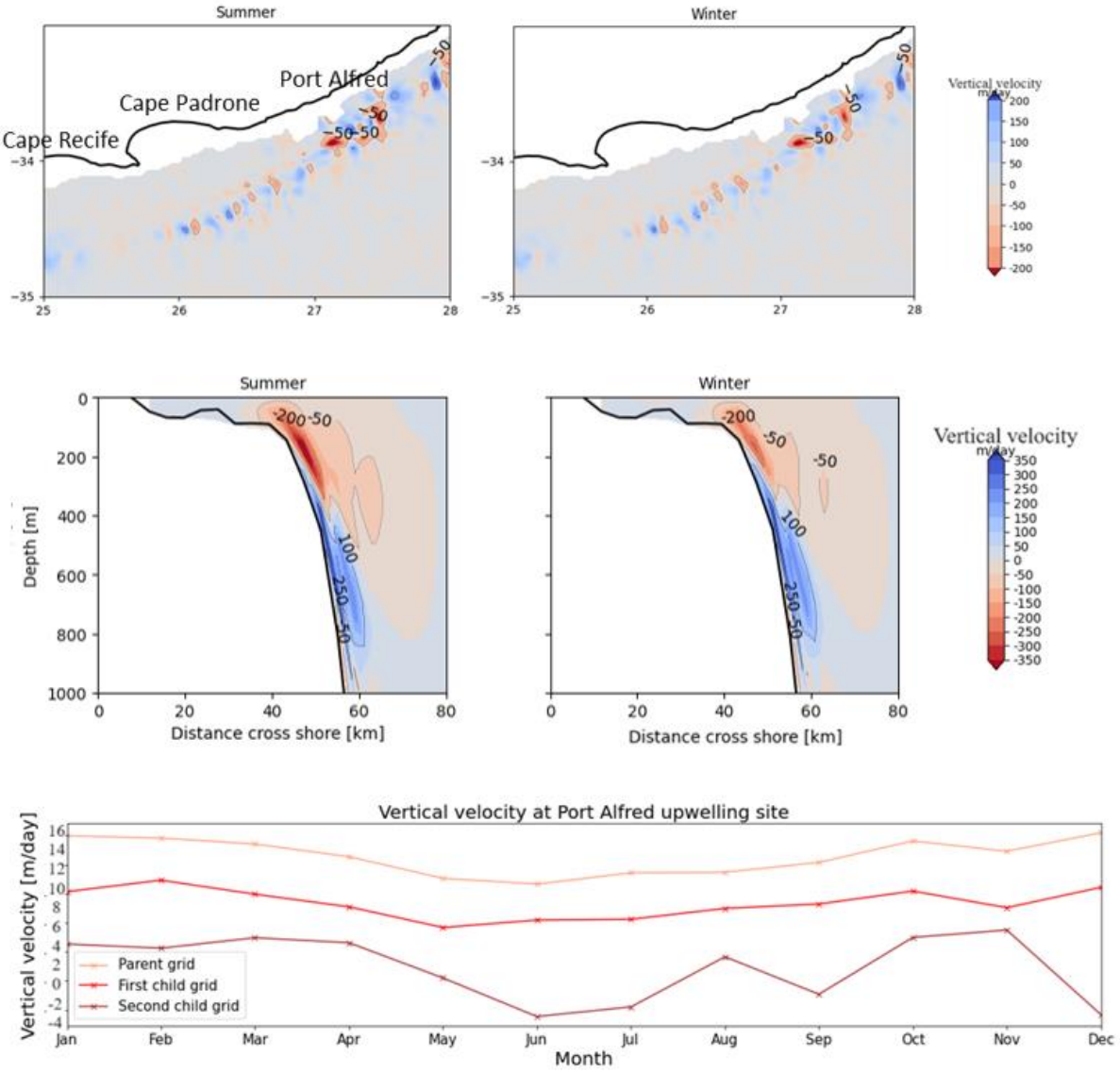

Figure 4.10: 1st row (left to right) – vertical velocity for summer and winter, 2nd row (left to right) – monthly mean of vertical velocity at 100m

In Figure 4.10, we plotted the vertical velocity at 100m and the vertical distribution of the vertical velocity for summer and winter. We also plotted the climatological monthly mean of vertical velocity computed at a depth of 100m from the 1/4°, 1/12° and 1/36° CROCO grid in the Port Alfred upwelling zone. It was previously observed that the vertical velocity during the mean state did exhibit a considerable noise signal. At a depth of 75m, the signal at the Port Alfred region was marked by high variability upwelling and downwelling zones ranging from -50 to 50 m/day. On the overall, summer was characterised by stronger upwelling and downwelling compared to winter despite a noisy signal. More distinct downwelling was observed from a depth of 100 to 300m along the continental slope in summer, whereby it reached -200 m/day due to a stronger presence of the current in summer. The presence of upwelling was observed along the continental slope from a depth of 400m to 900m. We can observe a slightly stronger upwelling in summer compared to winter. At the continental shelf in the upwelling zone, the variation of the vertical velocity was much smaller whereby the output from 1/36° CROCO grid showed a peak of vertical velocity of 4 m/day in summer and a drop of -4 m/day in winter. The 1/4 and 1/12 CROCO grid showed mostly a positive vertical velocity. However, the 1/4° and 1/12° CROCO grid possibly overestimated the vertical velocity in the upwelling region whereby16 m/day was recorded by the 1/4° CROCO grid and 10 m/day in the 1/12° CROCO grid.

4.5 Identification of upwelling events

4.5A Testing 2 different SST derived upwelling indices

After the revolution of satellite-derived ocean temperature, there were a few upwelling indices derived from these measurements. For instance, the difference between the inshore zone of upwelling and an offshore site at the same latitude has been calculated to detect upwelling events in a few studies (Wooster et al., 1976; Speth et al., 1978; Santos et al., 2005). Demarq and Faure (2000) formulated a new upwelling index by relying on the minimum and maximum temperature of the West African coastal upwelling. Ramanantsoa (2018) computed an adapted version of this upwelling index in the south coast of Madagascar region. Jhung and Cho (2021) also formulated an adapted version of the Demarq and Faure°s method by including the temperature at the seafloor in the upwelling zone.

Some of these upwelling indices (Ramanantsoa, 2018; Wooster et al., 1976; Santos et al., 2005, Jhung and Cho, 2022) included a comparison to an offshore site at the same latitude in their equation. This approach could thus be problematic as other oceanographic or atmospheric forcing mechanism which would not be linked to the upwelling event, would be influencing this offshore zone. These upwelling indices were also unable to detect upwelling in the subsurface zone as they only relied on the surface temperatures.

In the case of Port Alfred upwelling, we detected the upwelling events based on 2 upwelling indices. The first method was an adapted Demarq and Faure (2000)'s coastal upwelling index and was defined as:

$$CUI = \frac{Temp_{offshoresurface} - Temp_{coastalsurface}}{Temp_{offshoresurface} - Temp_{coastalbottom}}$$

The coastal surface/bottom temperature was an average temperature at the site of the Port Alfred upwelling zone and the offshore surface temperature was the average temperature of a site along the same latitude but 500km away from the upwelling zone to ensure that this temperature was not influenced by the warm current's meanders. The upwelling event was defined as CUI > 0.25

The second upwelling index was the 30-day high pass filtered average sea surface temperature data at the site of the upwelling zone from the CROCO model. In this case, the upwelling event was defined as SST (residuals) < -1°C.

Since the adapted Demarq and Faure (2000) upwelling index did include 2 additional variables other than the surface temperature at the upwelling zone, this could lead to errors. But relying on both upwelling indices ensured more robust results.

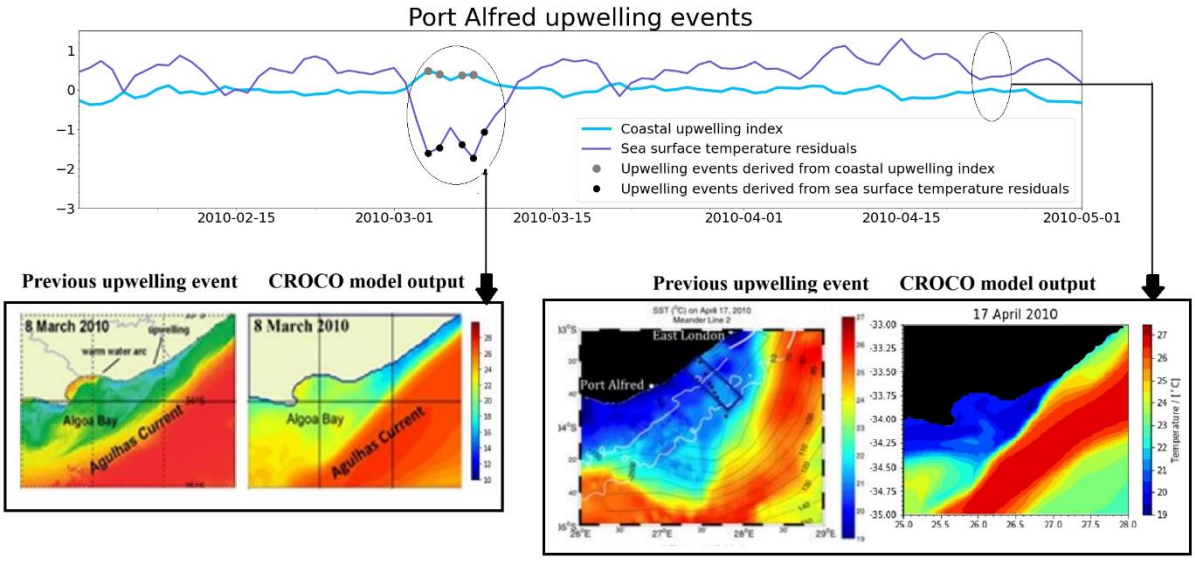

Figure 4.11: 1st row: Coastal upwelling index and sea surface temperature residuals with upwelling events recorded as grey and black dots. 2nd row (left to right): sea surface temperature showing upwelling event recorded on 8th March 2010 from Goschen et al. 2015, sea surface temperature from simulation from second child grid on 8th March 2010, sea surface temperature from upwelling event recorded on 17th April 2010 from Leber et al. (2017) and sea surface temperature from second child grid on 17th April, 2010.

We also made use of 2 previous upwelling events which have been recorded in the literature as benchmarks. This helped us to see whether the upwelling events detected from both upwelling indices are matching with the same dates as the ones recorded in previous studies. Goschen et al (2012) identified an upwelling event on the 8th March 2010 from MODIS satellite images and found that

there was a strong link to the northeasterly winds. Interestingly, both upwelling indices detected a strong upwelling event on the 8th March 2010. Leber et al (2017) also recorded a strong upwelling event linked to a meander on the 17th April 2010. However, both upwelling indices failed to detect any presence of cold water on the 17th April 2010 in the model output. We noted that the GHRSST satellite image from their study displayed a meander event. And yet, in the model outputs, there was no eddy activity during that week. Hence it was possible that the numerical model could not resolve cyclonic eddies on the inshore edge of the current.

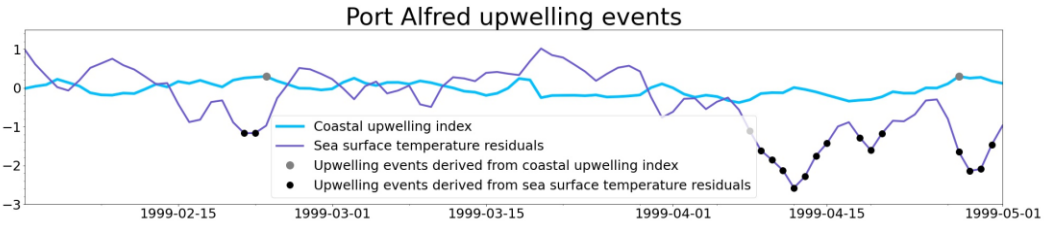

Figure 4.12: Coastal upwelling index and sea surface temperature residuals with upwelling events recorded as grey and black dots.

However, upon further investigation, through the 2 upwelling indices, we detected other upwelling events which correlated strongly with meander events (e.g 27 April 1999) in figure 4.11. Hence it was high likely that during strong meander events in the model, upwelling events did get detected, even if these meander events were not actually occurring according to the observation datasets. The model was not able to reproduce the meanders at the same dates as the observations, because the former were produced by model intrinsic variability inherent to the model nonlinearities unrelated to those in the real ocean.

4.5B Sea surface temperature and vertical velocity as upwelling indicators

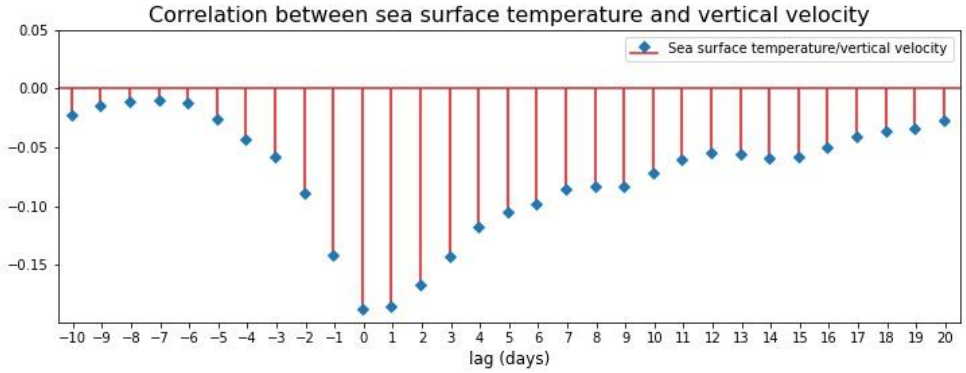

Figure 4.13: Correlation between sea surface temperature and vertical velocity in the Port Alfred region.

Sea surface temperature was not the only indicator which could be tested in this upwelling. During an upwelling event, the vertical velocity at a depth of 100m increased at Port Alfred, and a negative

correlation between surface temperature and vertical velocity was recorded. The correlation would vary over a timeline. On average, the negative correlation was relatively low a week before the sea surface temperature was at its coldest. Gradually, this negative correlation progressed in 5 days, and the vertical velocity was the highest on the day when the drop in temperature was at its peak, reaching a negative correlation of 0.2. During the following week, there was still a negative correlation, but it got weaker over the next 10 days.

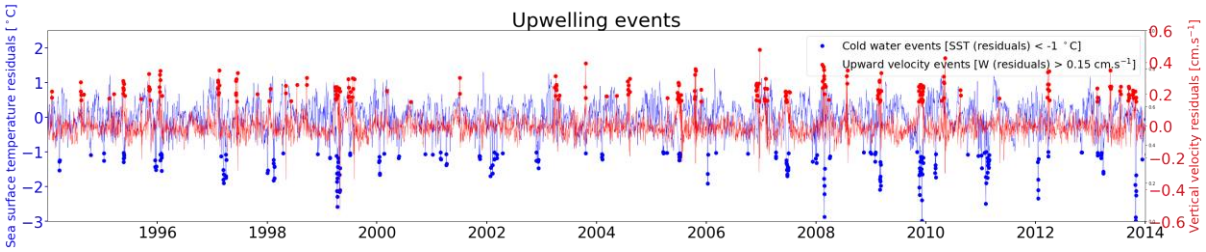

Figure 4.14: Daily sea surface temperature residuals (blue) with cold water events recorded as blue dots and daily vertical velocity residuals at a depth of 100m (red) with upward velocity events recorded as red dots.

Using both fields as upwelling indicators, we located individual upwelling events throughout the whole timeline. Here we rely on the residuals after a classical decomposition of the sea surface temperature and vertical velocity in the Port Alfred upwelling region to compare whether the upwelling events detected from temperature are matching with those from vertical velocity. We had set a threshold for identifying upwelling events by considering only those where the residual temperature was below -1°C and the residual vertical velocity exceeded 0.15cm/s. These two criteria were quite extreme, but this was to ensure we truly captured the strong upwelling events. In Figure 4.14, we could observe all the upwelling events from 1994 to 2014, and there were 56 cold water events detected from the temperature, and 49 upward velocity events detected from the vertical velocity. While not all of them matched each other, there were still a few distinct events which did show that there was a strong link between the vertical velocity and the temperature.

4.6 Average conditions during upwelling events

After exploring the upwelling through the lens of the mean and seasonal state, we selected only the 56 cold water events detected from the sea surface temperature residuals (SST residuals < -1°C) and calculated a mean state of the conditions during the upwelling. Figure 4.13 illustrates the average conditions of sea surface temperature, sea surface salinity, vertical velocity at a depth of 75m, a cross section of the temperature, salinity and vertical velocity during the 56 upwelling events. The surface temperature recorded in the upwelling zone ranged from 17°C to 19°C while the Agulhas Current ranged from 21°C to 24°C. A strong upwelling signal could be observed along the coastline in the regions of Port Alfred as well as Cape Recife extending to the bays. The cross section of temperature

showed that there was a strong presence of warm water ranging from 20°C to 24°C at the surface extending to 160km along the transect from a depth of 100m to the surface.

The upwelling was marked by a salinity of 35.2 PSU at the coast and varied between 35.3 PSU to 35.5 PSU in the current region. On the vertical structure of salinity, the current region was strongly characterized by a salinity ranging from 35.3 PSU to 35.5 PSU from the surface to a depth of 300m, while a salinity of 35.2 PSU was recorded at the inshore edge. At a depth of 75m, we also noted a strong upwelling near Port Alfred. The vertical velocity varied from -50 to 100 m/day. The cross section of the vertical velocity also showed a strong upwelling of 100 m/day occurring in its bottom boundary layer. Focussing only at this specific temporal scale, it was clear that the average position of the current did not display any meander and there was a strong link between the presence of the strong current and the upwelling. However these 56 cold water events were a sum of upwelling events generated from different mechanisms and it could offer a muddied picture, as some upwelling events could have occurred during a shear edge eddy, a Natal pulse event, under the influence of a strong north easterly wind component, during the presence of a strong current or coastal trapped waves. For a deeper investigation, we would still need to explore cases individually.

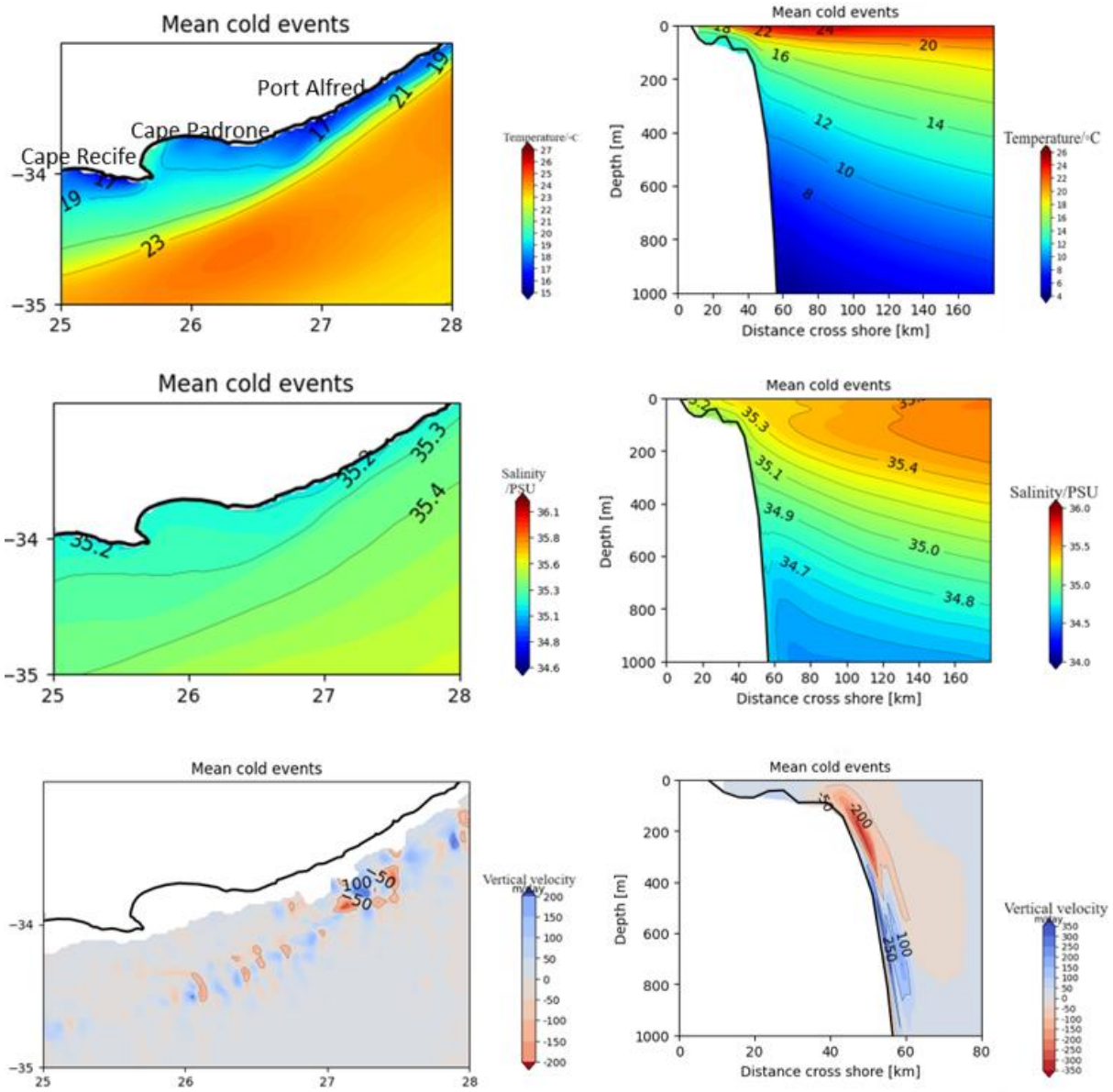

Figure 4.15: Average conditions during 56 selected upwelling events. 1st row (from left to right): sea surface temperature, sea surface salinity, 2nd row (from left to right): vertical temperature and vertical velocity.

4.7 Choice of 4 Case studies

Based on the different hypotheses behind the mechanisms of the upwelling, we chose to focus on 4 upwelling events detected from the 2 sea surface temperature-derived upwelling indices mentioned above (Adapted Demarq°s coastal upwelling index and residuals of sea surface temperature). As identified from the literature, many hypotheses could theoretically justify partially or entirely the Port Alfred upwelling.

- Presence of Agulhas Current – 22nd February 1999

Since the current could induce upwelling through Ekman veering in the bottom layer, we chose the upwelling event of 22nd February 1999 whereby the current was noted to be very strong.

- Presence of meander - 27th April 1999

Leber et al (2017) and Goschen et al. (2012) had also identified that the upwelling could be meander induced, so we chose to explore the upwelling event of 27th April 1999 whereby a strong cyclonic eddy was flowing on the inshore edge.

- Presence of northeasterly winds – 8th March 2010

It could also be wind-driven by offshore Ekman transport or driven by surface divergence, and we chose the upwelling event during the 8th March 2010 which was highly influenced by upwelling favourable winds, as previously identified by Goschen et al. (2015).

- Presence of coastal trapped waves – 19th September 2014

And lastly, from the hypothesis of coastal trapped waves as a potential mechanism behind the Port Alfred upwelling, we also explored the upwelling event of 19th September 2014 which had a strong presence of coastal trapped waves as previously identified by Bailey et al. (2022).

4.7A Case studies

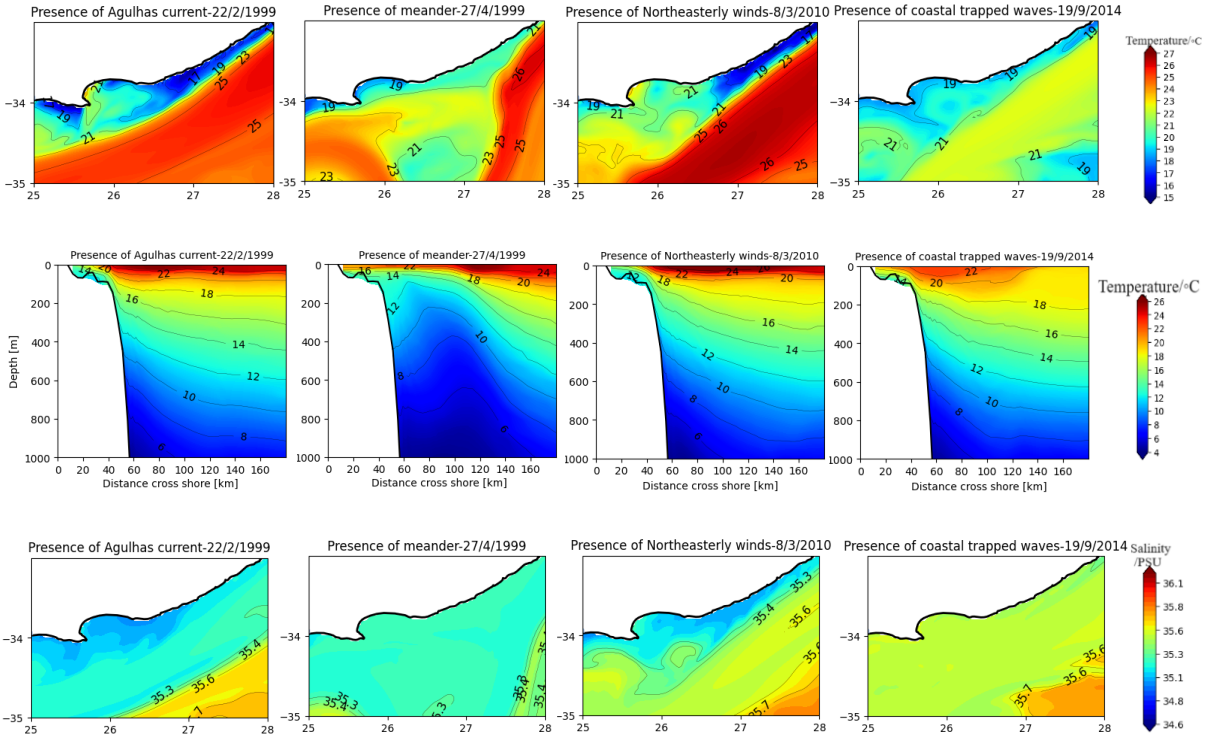

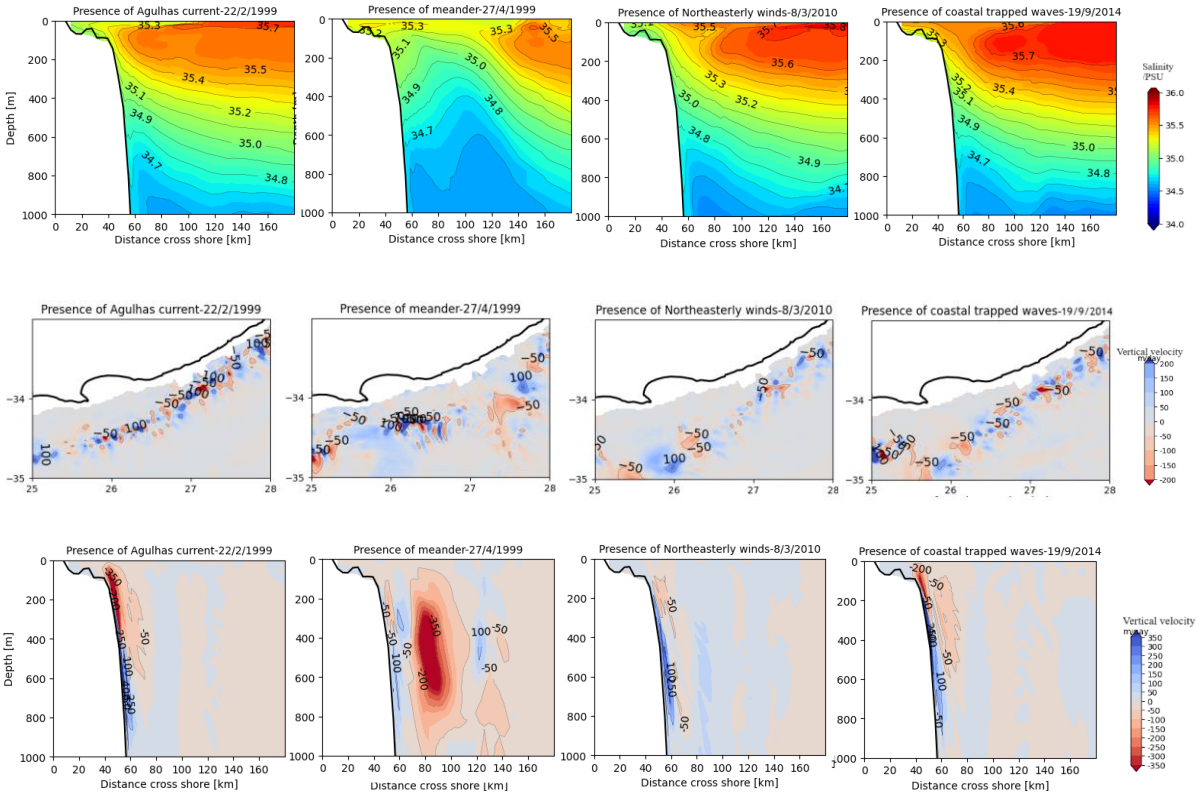

Figure 4.16: 1st row (from left to right) sea surface temperature on the 22nd February 1999, 27th April 1999, 8th March 2010 and 19th September 2014. 2nd row (from left to right) vertical temperature on the 22nd February 1999, 27th April 1999, 8th March 2010 and 19th September 2014. 3rd row (from left to right) sea surface salinity on the 22nd February 1999, 27th April 1999, 8th March 2010 and 19th September 2014. 4th row (from left to right) vertical salinity on the 22nd February 1999, 27th April 1999, 8th March 2010 and 19th September 2014. 5th row (from left to right) vertical velocity at a depth of 75m on the 22nd February 1999, 27th April 1999, 8th March 2010 and 19th September 2014. 6th row (from left to right) vertical velocity on the 22nd February 1999, 27th April 1999, 8th March 2010 and 19th September 2014.

These 4 case studies displayed a strong presence of cold water in the Port Alfred upwelling zone, and yet the conditions for the temperature, salinity and vertical velocity were completely different in each case. Figure 4.14 illustrates the sea surface temperature, vertical section of temperature, sea surface salinity, vertical section of salinity, vertical velocity from a depth of 75m and the vertical velocity of the 4 case studies.

Case study: 22nd February 1999

Upwelling detected on the 22nd February 1999, was possibly linked to Ekman veering in the bottom layer as it showed the presence of a strong Agulhas Current. In this case, the sea surface water displayed a temperature between 14°C to 16°C in the upwelling zone, and it reached about 25°C in the core of the current. Through the vertical temperature, the strong presence of the current could be

seen with a warm temperature of 25°C at the surface and 19°C extending to a depth of 200m. The salinity in the overall region was about 35 PSU. The vertical velocity showed a strong pronounced downwelling event in the current region where it dropped to -500 m/day. The sea surface temperature, vertical temperature and vertical velocity showed a strong presence of the Agulhas Current on that day except for the sea surface salinity. Considering it was summer, the fresher waters were possibly linked to the rainfall.

Case study: 27th April 1999

During the upwelling event of 27th April 1999, we noted the presence of a meander event. The temperature ranged between 20°C and 22°C in the upwelling region on that day. At the leading edge, we also noted a small plume of warm water from the current which was influencing the region with a warmer temperature. As for the vertical temperature, we could see the temperature ranged from 15°C to 25°C from the surface to a depth of 50m in the upwelling region. A higher salinity of 35.5 PSU was recorded at the core while fresher waters of 35.2 PSU was recorded close to the coast. Through the salinity, we could note the plume, showing a slightly higher salinity. From the surface to a depth of 200m, a positive vertical velocity was recorded ranging from 0 to 100 m/day showing a clear presence of downwelling extending much further south, aligned with the current°s meander. Generally, the presence of a meander would induce a stronger upwelling at the leading edge and at the centre of the eddy. Since this upwelling event was detected towards the end of the passage of the eddy, it was possible that additional factors were also playing an active role in this upwelling event along with the cyclonic eddy.

Case study: 8th March 2010

The case study on the 8th March 2010 showed a relatively stronger upwelling event compared to the other cases whereby the sea surface temperature was 14°C in the upwelling region. It showed the presence of the current whereby the temperature at the core was 27°C. The vertical section of the temperature also showed a much colder temperature from a depth of 200m to the surface ranging between 10°C to 15°C. The salinity also delineated the presence of the current, recording between 35.45 PSU to 35.75 PSU in the zone of the current and a lower salinity of 35.15 PSU in the upwelling region. As for the vertical velocity, we noted a strong upwelling activity with a peak of 100 m/day at 33.6° S latitude and a depth of 200m. In the vertical section, the current did not seem to have a strong downwelling from the depth of 300m to 1000m and only recorded a vertical velocity ranging from 0 to -200 m/day. In this case, Goschen et al. (2015) had previously linked this upwelling to a strong presence of northeasterly winds. While the temperature and salinity fields did capture the presence of the current, the vertical velocity revealed that the current was possibly not as strong compared to the other case studies. It was still possible that that the presence of the current was linked as an additional

forcing mechanism. Further exploration of its wind stress and wind stress curl would provide a better understanding of this case study.

Case study: 19th September 2014

The case study on the 19th September 2014 detected cold water ranging from 16°C to 20°C in the upwelling region. The core of the current recorded a temperature of 23°C which seemed relatively weaker compared to the other case studies. But, the cross section of the temperature showed that the temperature ranged from 16°C to 23°C from a depth of 400m to the surface, showing that the current was not weak. An overall of 35.60 PSU of salinity was recorded on that day. The vertical velocity also showed some strong downwelling along the continental slope ranging from -100 m/day to -400 m/day. Since this case study was associated with the presence of coastal trapped waves from the study of Dylan et al (2020), we would need to investigate other oceanographic fields such as the sea surface height and atmospheric fields to have a better understanding of this case study.

4.8 Summary and discussion

Investigating the temperature, salinity and vertical velocity through different temporal lens such as its mean state, seasonal state, mean state only during upwelling events and isolated case studies revealed that this upwelling was much more complex and there were many forcing mechanisms possibly driving this upwelling. The mean state of the temperature, salinity and vertical velocity showed that the higher resolution of 1/36° CROCO grid could resolve the current better compared to the others. The 1/4° and 1/12° CROCO grid would often overestimate the temperature, salinity and vertical velocity fields near the coast. During the mean state, we could not link the upwelling to other drivers such as a meander event, but we observed that the upwelling linked to the presence of the current was well captured. This implied that this mechanism was triggering the upwelling throughout the whole year.

The seasonal state of sea surface temperature showed that the Agulhas Current was generally weaker in winter with a lower temperature of the current's core recorded in winter. We also conducted a decomposition of the sea surface temperature into its trend, seasonal and residual components for each dataset. Assessing these components separately allowed us to depict any underlying pattern and sources of variability in temperature. We noted a constant regular seasonal variations from each dataset and unpredictable fluctuations for the residuals whereby the high negative values were cold water events possibly linked to upwelling. Again, we noted an overestimation of temperature in the upwelling region for the 1/4° and 1/12° CROCO grid.

Inspecting the seasonal state through the salinity and vertical velocity, winter was characterized with higher salinity and less downwelling in the Agulhas region compared to summer. Even if the model recorded a lower salinity in summer, this was likely due to more rainfall in summer. On the overall,

the upwelling did not capture a strong seasonal signal from the temperature, salinity and vertical velocity and we would still require to explore the seasonality of other atmospheric and oceanographic fields in this region.

Focusing on the upwelling events, we relied on the adapted Demarq's coastal upwelling index as well as the residuals of the sea surface temperature to detect the upwelling events in the model. Since we were able to detect the same upwelling event which was recorded in the study of Goschen et al. (2015), these two upwelling indices proved to be a more robust method. Even if the 2 upwelling indices failed to identify the meander induced upwelling from the study of Leber et al. (2017), it was because the current in the model did not meander on that date. However, on further inspection, when the current did meander at another timestep, upwelling was also present. We also explored the link between vertical velocity and sea surface temperature and computed the correlation plot. The sea surface temperature showed a correlation of -0.15 with vertical velocity, which showed that on average as the sea surface temperature decreased, the vertical velocity increased. We then used the residuals of the vertical velocity as an upwelling indicator and identified 49 upwelling events from 1994 to 2014 compared to the 56 upwelling events which was identified from the sea surface temperature residuals. The number of upwelling events recorded was much lower compared to Leber et al. (2017)'s study whereby they also filtered the sea surface temperature from a higher resolution dataset (GHRSST) and identified 47 upwelling events from 2003 to 2011.

Using only these 56 upwelling events, we explored the mean conditions of the temperature, salinity and vertical velocity. The upwelling conditions ranged from a temperature of 16°C to 19°C and a salinity from 35 PSU to 35.30 PSU. The presence of the current was well detected whereby the vertical velocity ranged from 0 to -350 m/day from a depth of 100m to 1000m. However, since these composites were an average of merged contributing factors of the upwelling, and it was likely that some forcing mechanisms had a stronger influence while others were less dominant. Hence it was necessary to assess isolated cases of upwelling to obtain more insights.

Since we wanted to target several hypotheses (Current-driven upwelling through bottom Ekman veering, meander induced upwelling, wind-driven upwelling, upwelling by vertical mixing and upwelling due to coastal trapped waves), we carefully selected 4 case studies and explored the fields of temperature, salinity and vertical velocity. While the temperature and vertical velocity were able to confirm the presence of the meander and the current at the surface and from the cross section, this was not enough to conclude whether the upwelling was current driven or meander induced. We would still need to explore the conditions of other atmospheric and oceanographic fields during each case study to see the bigger picture.

4.9 Highlights

As an overall, the main findings from this investigation highlighting this study's unique contributions included:

1) The 1/12° and 1/36° CROCO grids successfully captured the temperature signature of the upwelling during the mean state, with the 1/36° grid displaying a more pronounced presence of the current and upwelling, averaging 19°C in the upwelling region and 23°C in the core of the current.
2) The CROCO grids recorded higher salinity compared to the observational datasets, particularly noticeable in the CARS09 and WOA2018 datasets, with the 1/36° CROCO grid registering a salinity of 35.3 PSU in the upwelling region.
3) The vertical velocity signal exhibited significant noise at that depth in each CROCO simulation. While the 1/4° and 1/12° CROCO grids struggled to delineate changes in bathymetry at 100m and showed minimal variation in vertical velocity, the 1/36° CROCO grid was able to outline the seafloor on the continental shelf. Near Port Alfred, it depicted small pockets with a high variation of vertical velocity ranging between -50 and 50 m/day in the current region.
4) We decomposed the sea surface temperature and the vertical velocity to filter the seasonal influence and noted a strong seasonal influence. The 1/36° CROCO grid was in agreement with the OSTIA dataset showing a range between 16°C to 22°C while the coarser resolution grid overestimated the sea surface temperature.
5) We tested 2 upwelling indices (adapted Demarq's upwelling index and residuals of sea surface temperature) to identify upwelling events.
6) There is a negative correlation of 0.2 between vertical velocity and sea surface temperature. 56 upwelling events were identified from the residuals of the sea surface temperature and 49 upwelling events were found from the residuals of the vertical velocity. We also identified 4 case studies which had different temperature, salinity and vertical velocity conditions.

Chapter 5: Influence of atmospheric forcing on Port Alfred upwelling

5.0 Introduction

After exploring the spatial and temporal characteristics of the upwelling, we could now address the second research question in this chapter:

What is the influence of atmospheric forcing mechanisms on the Port Alfred upwelling?

As identified from the literature review chapter, strong northeasterly winds have been known to induce coastal upwelling in Port Alfred (Gill, 1982) through offshore Ekman transport and Ekman pumping. Vertical mixing through turbulence could also lead to coastal upwelling. And to test whether Port Alfred upwelling was influenced by the atmosphere, we could measure its wind properties and parameters.

5.1 Wind properties and parameters to determine atmospheric influence

5.1A Wind stress

Analysing the wind stress would give a good indication of Ekman transport. Upwelling caused by wind stress has been well documented in Cabo Frio upwelling located on the inshore edge of Brazil current (Castelao and Barth, 2005). As these winds blew, they imparted force upon the sea surface, setting surface waters into motion away from the coast. The Coriolis effect, arising from the Earth's rotation, induced these moving waters to veer to the left, resulting in a net transport of water away from the shore. This offshore movement of surface waters would create a void near the coast, prompting the rise of nutrient-rich subsurface waters to replace the displaced surface waters, initiating the upwelling process (Huyer 1983; Smith 1995).

5.1B Wind speed and direction

The orientation of wind and its speed would also influence the resultant water movement, influencing the direction and magnitude of Ekman transport and suction. Leber et al. (2017) and Goschen et al. (2012) have previously used wind speed and wind direction to investigate whether the Port Alfred upwelling is wind-driven and identified strong wind speeds of a northeasterly could lead to enhanced offshore Ekman transport (Goschen et al, 2012).

5.1C Wind stress curl

An assessment of the wind stress curl provides a good understanding of the Ekman pumping in many coastal upwelling zones (Castelao and Barth, 2005). Ekman pumping would lead to divergence of

Ekman currents and would prompt subsurface waters to move from the subsurface zone in order to replace the diverging surface waters. In the Agulhas region, when the wind stress curl is negative, it leads to divergence and allows for Ekman pumping to occur (Gill 1982; Pickett and Paduan 2003).

5.1D Frictional velocity

Vertical mixing induced by turbulence is another upwelling mechanism. Frictional velocity, representing the intensity of shear stress, influences the strength of turbulence and, consequently, the efficiency of vertical mixing (Kampf, 2016). When higher values of frictional velocity (u*) are recorded, it indicates more energetic shear stress, promoting turbulence and facilitating the exchange of water masses between different vertical layers in the ocean. Kampf (2016) used a nonhydrostatic numerical model and was able to link onshore winds to vigorous vertical mixing leading to upwelling in shallow water.

5.1E Wind-driven upwelling indices

Figure 5.1 Vagn Walfrid Ekman measuring the velocity from a current meter (Kampf, 2012)

Aside from these wind properties and parameters, we could also rely on wind-driven upwelling indices to investigate the influence of atmospheric forcing mechanisms. Bakun (1973) firstly investigated the North American west coast upwelling zone and formulated monthly, quarterly and annual upwelling indices from 1946 to 1971 by using coastal wind data.

In recent studies, the Bakun upwelling index could detect upwelling events by assessing the Ekman transport velocities computed from wind stress (Bakun and Parrish, 1997). The Bakun and Parrish upwelling index combined wind stress and sea level pressure data to quantify the strength of winds that facilitate upwelling (Bakun and Parrish, 1997).

As a summary, assessing these wind properties, parameters and wind driven upwelling indices in Port Alfred would provide better insight on the atmospheric influence in the region. Offshore Ekman transport, driven by wind stress, results in horizontal movement and upwelling by displacing surface waters. Ekman pumping is closely linked to Ekman transport, reinforcing upwelling by creating a divergence that induces the vertical movement of nutrient-rich waters from below and frictional

velocity causing upwelling through vertical mixing involves chaotic and random movements within the water column, leading to the upward transport of deeper waters.

5.2 Aims and objectives

Hence this chapter was aimed at providing a detailed description of this upwelling by investigating its alongshore wind stress, wind stress curl, wind direction and frictional velocity. This chapter involved 3 key questions:

5.2A What is the influence of Ekman transport in the Port Alfred upwelling zone?

We investigated the alongshore wind stress during summer and winter and explored whether there was any correlation to upwelling. We also looked at individual case studies as well as its mean state during upwelling events.

5.2B What is the influence of Ekman pumping in the Port Alfred upwelling zone??

We investigated the wind stress curl at different temporal scales and explored whether there was any correlation to upwelling.

5.2C What is the influence of vertical mixing in the Port Alfred upwelling zone??

We investigated frictional velocity at different temporal scales and explored whether there was any correlation to upwelling.

5.3 Methods

To address these key questions, we computed the alongshore windstress, the windstress curl and the frictional velocity. The horizontal and vertical wind stress are obtained from the ERA Interim atmospheric reanalysis (Dee et al. 2011), sourced from the European Centre for Medium-Range Weather Forecasts (ECMWF). This dataset had a spatial resolution of 25 km. (Collins et al., 2012).

Since the coastline was closely oriented in an east-west direction, we computed the alongshore wind stress as:

$$\tau_{\text{alongshore}} = \tau_x$$

whereby τ_x is the zonal wind stress component and its unit was N/m^2.

The wind stress curl was denoted as $\nabla \times \tau$, whereby

$$\nabla \times \boldsymbol{\tau} = \left(\frac{\partial \tau_y}{\partial x}\right) - \left(\frac{\partial \tau_x}{\partial y}\right)$$

$(\partial\tau_y/\partial x)$ represents the partial derivative of the meridional (north-south) wind stress component (τ_y) with respect to the east-west (x) direction. $(\partial\tau_x/\partial y)$ represented the partial derivative of the zonal (east-

west) wind stress component (τ_x) with respect to the north-south (y) direction. The unit for wind stress curl was N/m^3.

The frictional velocity, u_* is calculated as:

$$u_* = \sqrt{\frac{\sqrt{(\tau_x)^2+(\tau_y)^2}}{\rho}}$$

whereby τ_x is the zonal component of the wind stress, τ_y is meridional component of the wind stress, ρ is the density and its unit was cm/s.

We also computed the Bakun upwelling index (1973) as:

$$Ek = \frac{\tau_{\text{alongshore}}}{L_u \rho_0 f}$$

whereby E_k is the upwelling velocity measured in m/day. L_u is the width of Ekman divergence. In this case, we used the value of the internal Rossby radius number (30km) as L_u (Malan et al, 2018). ρ_0 is the seawater density and f is the Coriolis parameter, which is a function of latitude and represents the effect of the Earth's rotation on ocean currents.

The monthly means of the Bakun upwelling index and model derived vertical velocity were first plotted so that we could assess whether upwelling in the model was occurring at the same as in the wind driven upwelling index. We then computed the atmospheric fields at different temporal scales. We calculated the seasonal state of wind stress, wind stress curl and frictional velocity. We also computed the climatological monthly mean of these fields. We also used the model generated fields sea surface temperature and vertical velocity to compare their climatological monthly mean and computed the correlation between these atmospheric fields and sea surface temperature/vertical velocity. Then we assessed the mean state of the wind stress and the wind stress curl during the 56 selected upwelling events chosen from chapter 4. And lastly, we explored the conditions of the wind stress and wind stress curl during the 4 case studies which were selected in chapter 4.

5.4 Results

5.4A Influence of atmospheric forcing

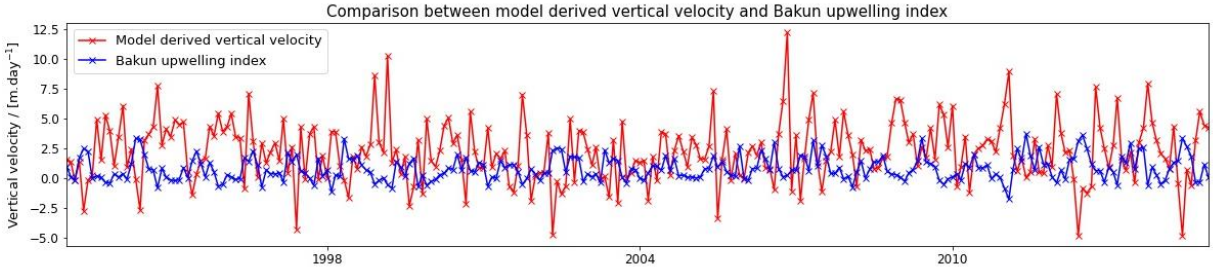

Figure 5.2: Monthly mean of model derived vertical velocity at 100m (red line) and Bakun upwelling index (blue line) at Port Alfred.

Monthly means of both the Bakun upwelling index and the model derived vertical velocity were computed from 1993 to 2014. An increase/decrease in the Bakun upwelling index and the vertical velocity would indicate upwelling/downwelling. The Bakun upwelling index ranged from -1 m/day to 2.5 m/day while the model derived vertical velocity ranged from -2.5 m/day to 5 m/day. This comparison clearly showed that wind-driven upwelling could not entirely explain all the upwelling events recorded from the simulations of the model. In general, the predominant winds in Port Alfred are southwesterlies and these winds would induce onshore Ekman transport and downwelling (Malan, 2013). It was also interesting to highlight that on many occasions, while the Bakun upwelling index was indicating an upwelling had occurred and the model also confirmed that the vertical velocity was much higher during this period (Dec 99, May 2004, Nov 2012). Hence this could potentially suggest that the drivers of these upwelling events were a combination of wind and additional factors. The low values of the Bakun upwelling indices could also be indicative of the wind stress' coarse resolution (25km) and smoothing technique closer to the coast compared to high resolution of the model derived vertical velocity (2.5km). This overall comparison of their monthly mean values did show that offshore Ekman transport played a role in the upwelling, but further investigation through the lens of different temporal scales would provide a better picture of its influence.

5.4B Wind stress

Seasonality of wind stress

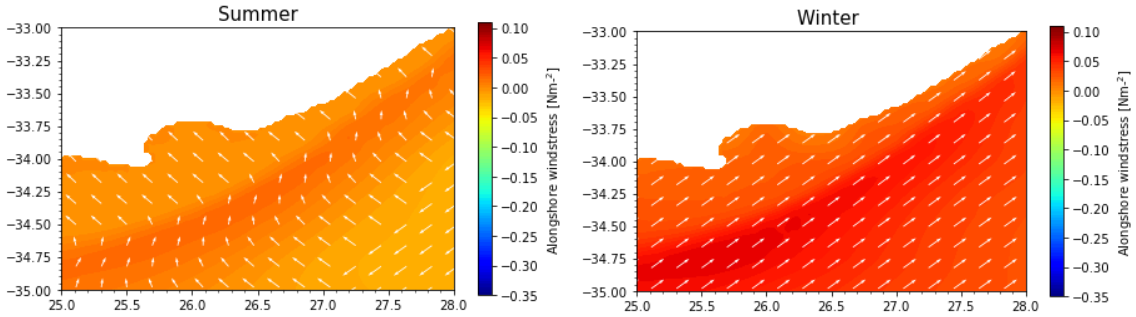

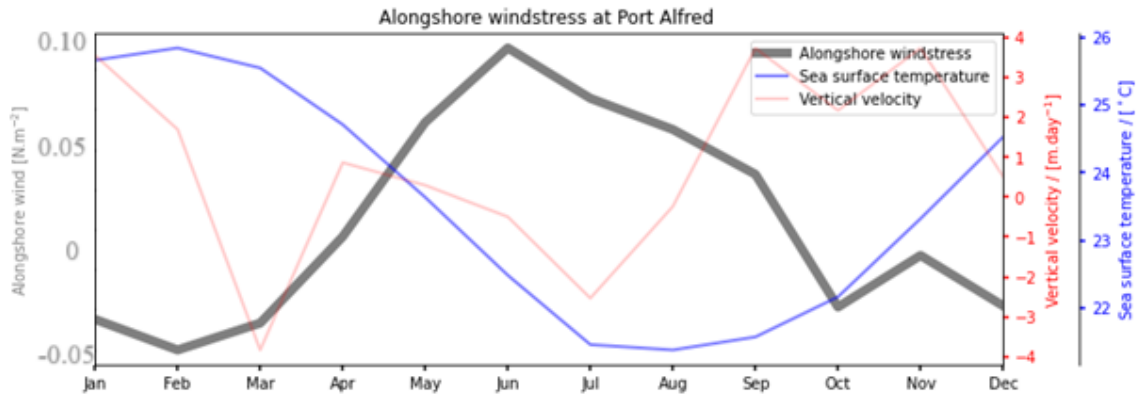

Figure 5.3: 1st row (left to right) - summer and winter wind stress, 2nd row – monthly mean of alongshore wind stress (grey line), sea surface temperature (blue line) and vertical velocity (red line)

The alongshore wind stress in summer displayed a southeasterly wind component closer to the shoreline and a northeasterly wind component along the Agulhas Current. In this region, the presence of southeasterly winds would lead to an increase in the wind stress, and this would induce an onshore Ekman transport, leading to a coastal downwelling. In summer, a slightly lower wind stress was recorded ranging between -0.05 N/m^2 to 0.05 N/m^2. Winter was characterized by a strong south-westerly wind component, estimated around 0.1 N/m^2 reaching to its maximum during the month of June. However, it was likely that the surface stress components of the global atmospheric re-analysis of ERA-Interim from ECMFW underwent much smoothing and exhibited large variability close to the coast (Hutchinson et al, 2018). Hence it was possible that the surface wind stress components were not well resolved in this region. Considering the offshore Ekman transport as a driver, it was unlikely that the upwelling had a seasonal signal. But it was still possible that strong singular wind stress events or a combination of wind stress along with additional driving mechanisms could trigger an upwelling in Port Alfred.

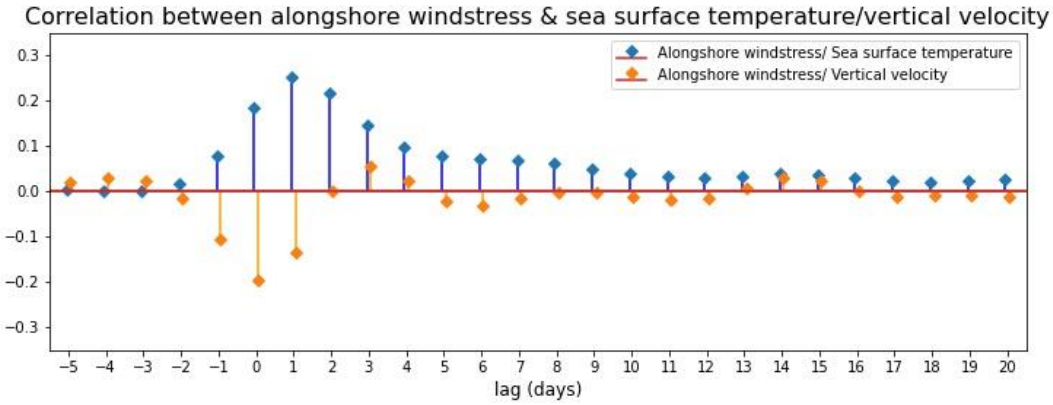

Figure 5.4: Correlation between alongshore wind stress and sea surface temperature (blue line)/ vertical velocity (orange line)

We explored the correlation between the alongshore wind stress and the sea surface temperature/vertical velocity using the simulations of the model for the time period of 1993 to 2014 in Figure 5.4. If wind stress was a significant driver behind the upwelling, we would expect a strong positive correlation between alongshore wind stress and sea surface temperature, and a strong negative correlation between alongshore wind stress and vertical velocity. This was clearly reflected in the correlation plot, but it was interesting to highlight that it took a day for the water to reach its coldest and the vertical velocity was at its highest exactly when the wind stress was the lowest. So there was a lag of 1 day after a strong wind event. This upwelling was seen to last for 3 days only when we considered the link between vertical velocity and wind stress. But the temperature remained cold for more than a week after a strong wind event. Interestingly, winter was generally characterized by lower sea surface temperature and higher wind stress, so there was clearly no seasonal influence on the correlation. Instead the correlation plot captured how the offshore Ekman transport would have been very strong during rapid singular cold water events and upward vertical velocity events due to its strong correlation values (0.3 with sea surface temperature and -0.2 with vertical velocity).

5.4C Wind stress curl

Seasonality of wind stress curl

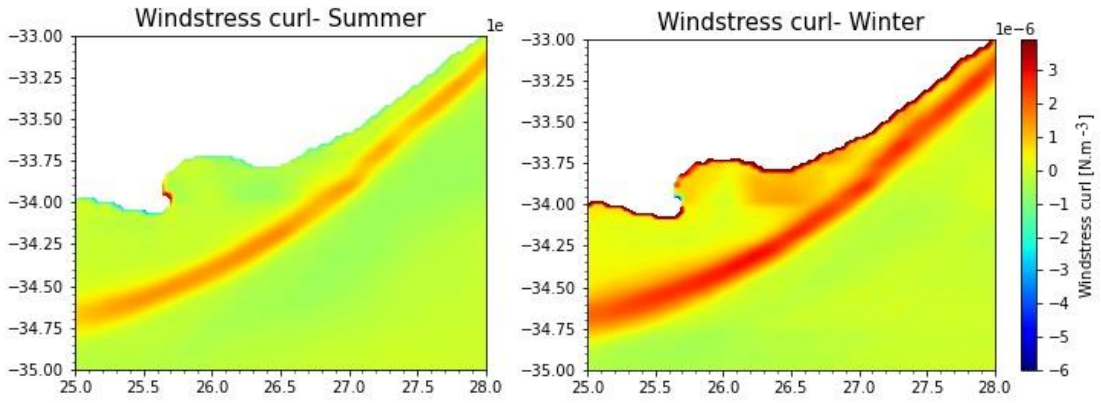

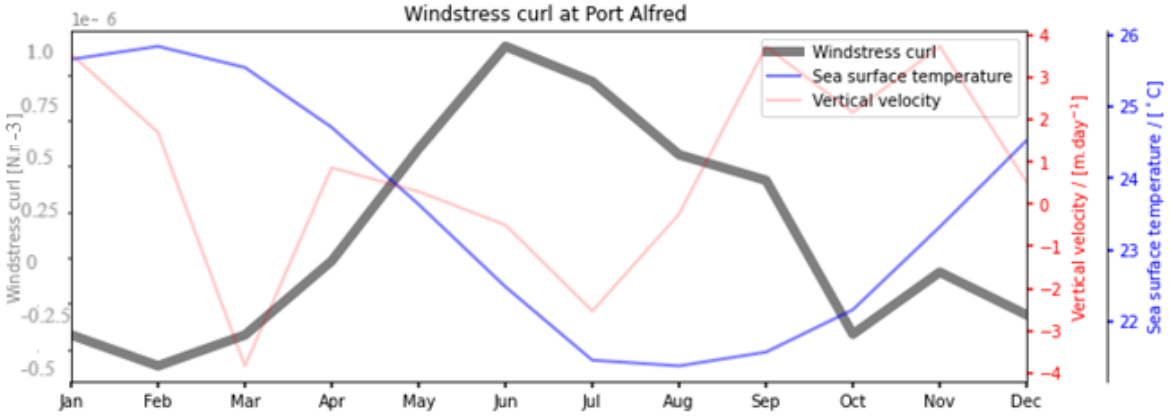

Figure 5.5: 1st row (left to right) - summer and winter windstress curl, 2nd row – monthly mean of wind stress curl (grey line), sea surface temperature (blue line) and vertical velocity (red line)

To investigate the seasonal influence of Ekman pumping, we assessed how the wind stress curl varied between summer and winter. In summer, in the Agulhas Current zone, the wind stress curl ranged from $1x10^{-6}$ to $2x10^{-6}$ N/m^{-3} while in winter, this value ranged from $2x10^{-6}$ to $3x10^{-6}$ N/m^{-3}. The region along the inshore edge of the current showed a relatively lower wind stress curl in summer along with a slight increase in winter even though the variation seemed very small.

It is necessary to highlight the high positive values of the wind stress curl in the Agulhas Current region. The wind stress curl band is associated with the shearing of the Agulhas Current along its inshore front due to the signature of the effect of current. This in turn leads to a positive wind stress curl which leads to downwelling and surface convergence along the front. This phenomenon can allow the convergence of floating material along the Agulhas front.

Focusing specially the Port Alfred region, the wind stress curl was at its maximum ($1x10^{-6}$ N/m^{-3}) during the month of June and its minimum during the month of February ($-0.5x10^{-6}$ N/m^{-3}). The negative wind stress curl, despite being very low, would imply that there was slight probability of surface divergence during the summer. As for winter, on average it would be unlikely for wind stress curl to trigger upwelling.

However, we would still need to be careful when analysing the surface stress components of the global atmospheric re-analysis of ERA-Interim from ECMFW due to its smoothing technique and its close location to the coast. Hutchinson et al. (2018) investigated the seasonal difference in wind stress curl and showed that it included quite some missing values closer to the coast and displayed a mostly positive wind stress curl in the Agulhas region in winter. Summer was characterized by a dominant negative wind stress curl in the Agulhas region with some smaller zones displaying a positive wind stress curl and some missing values as well. It was unlikely that Ekman pumping had a strong seasonal influence on the upwelling as a sole forcing mechanism. Although if Ekman pumping was considered as one of the contributing factors, then strong wind events could potentially be linked to surface divergence.

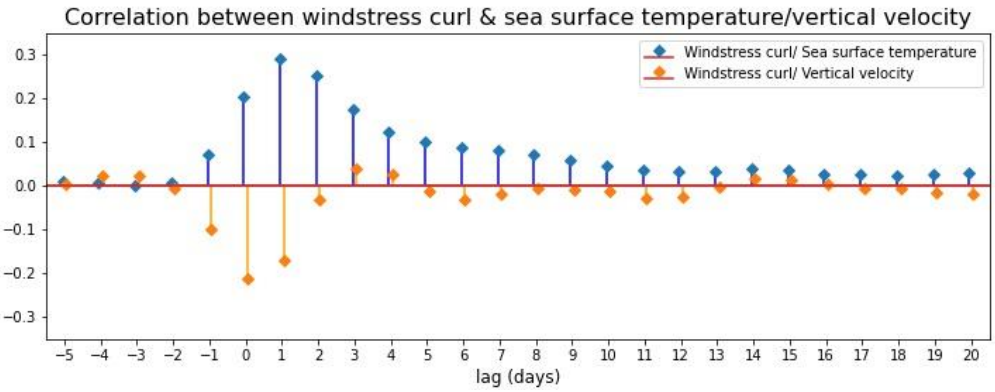

Figure 5.5: Correlation between wind stress curl and sea surface temperature (blue line)/ vertical velocity (orange line)

The seasonal signal could not detect with certainty if there was a direct link between wind stress curl and upwelling events. However a correlation between wind stress curl and upwelling events revealed a decrease in wind stress curl was strongly correlated to an increase in vertical velocity and a decrease in the sea surface temperature. The negative correlation between the wind stress curl and the vertical velocity was strong for a short period of 3 days (day -1, day 0 and day 1), but after day 1, there was no strong link between these 2 fields. As for the temperature, a positive correlation started on day -1, reaching its peak on day 1. It gradually slowed down after day 4 but maintained a weak positive correlation for more than a week. This suggested that the number of days for this type of upwelling would vary between 4 or 5 days. This was similar to the wind stress whereby an upwelling was very rapid and lasted from 3 to 4 days after the presence of an upwelling favorable wind. Another similarity with the wind stress was that the correlation plot did not show any seasonal influence in the correlation values. Since winter was characterized by a higher wind stress curl and lower surface temperature on average, this could have influenced the correlation by showing a negative correlation. However the strong positive correlation between surface temperature and wind stress curl showed that these short rapid singular events were clearly higher than average and influenced the correlation.

5.4D Frictional velocity

Seasonality

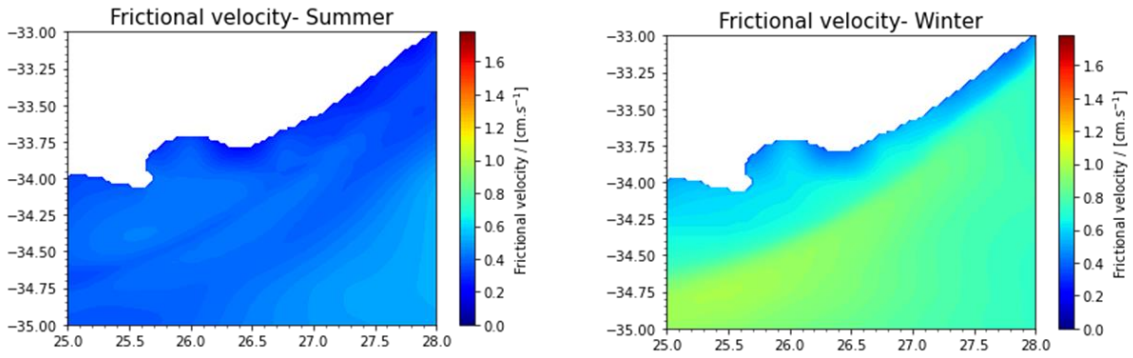

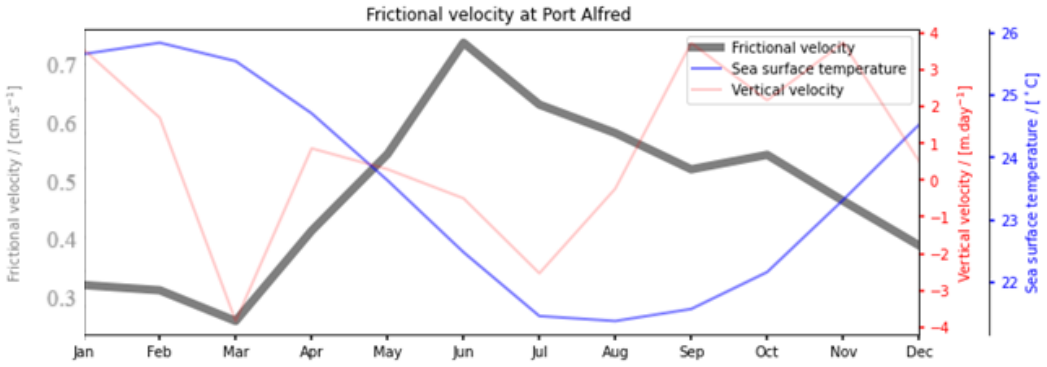

Figure 5.7: 1st row (left to right) - summer and winter of frictional velocity, 2nd row (left to right) – monthly mean of frictional velocity, sea surface temperature (blue line) and vertical velocity (red line)

The frictional velocity in the Port Alfred zone was estimated around 0.4 cm/s in summer and around 0.6 cm/s in winter in the upwelling region. This seemed to be in agreement with Klinger et al. (2006) whereby they also noted that other wind products such as NCEP and QuikSCAT also displayed a higher frictional velocity in winter compared to summer in the Agulhas region. The southwesterlies in Port Alfred would generally cause downwelling through onshore Ekman transport during winter. However, any presence of strong winds could exert a greater force on the water's surface, leading to increased frictional velocity in winter. The sheer strength of the wind stress would result in higher frictional velocity and increased turbulence. This, in turn, would lead to vertical displacement of waters through vertical mixing.

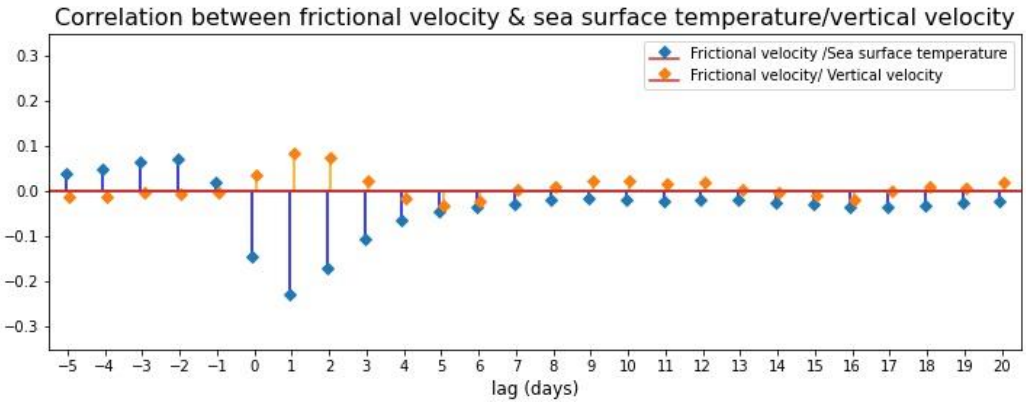

Figure 5.8: Correlation between frictional velocity and sea surface temperature (blue line)/ vertical velocity (orange line)

Frictional velocity showed a strong negative correlation with sea surface temperature, reaching a correlation of -0.2 on day 1. Compared to the previous correlation plots, frictional velocity has a relatively weaker positive correlation of 0.1 with vertical velocity on day 1. It makes sense why there is a weaker positive correlation with vertical velocity. This is because this upwelling is driven by vertical mixing and the depth at which vertical velocity has the most significant impact due to vertical

mixing would differ from the depth influenced by offshore Ekman transport. In both fields, it suggested that when the frictional velocity was at its lowest, an upwelling event would last for 3 days. This correlation clearly indicated during rapid singular events of very strong frictional velocity, this would lead to a decrease in sea surface temperature for 5 short days, and an increase in vertical velocity for 3 days.

5.4E Composites during upwelling events only

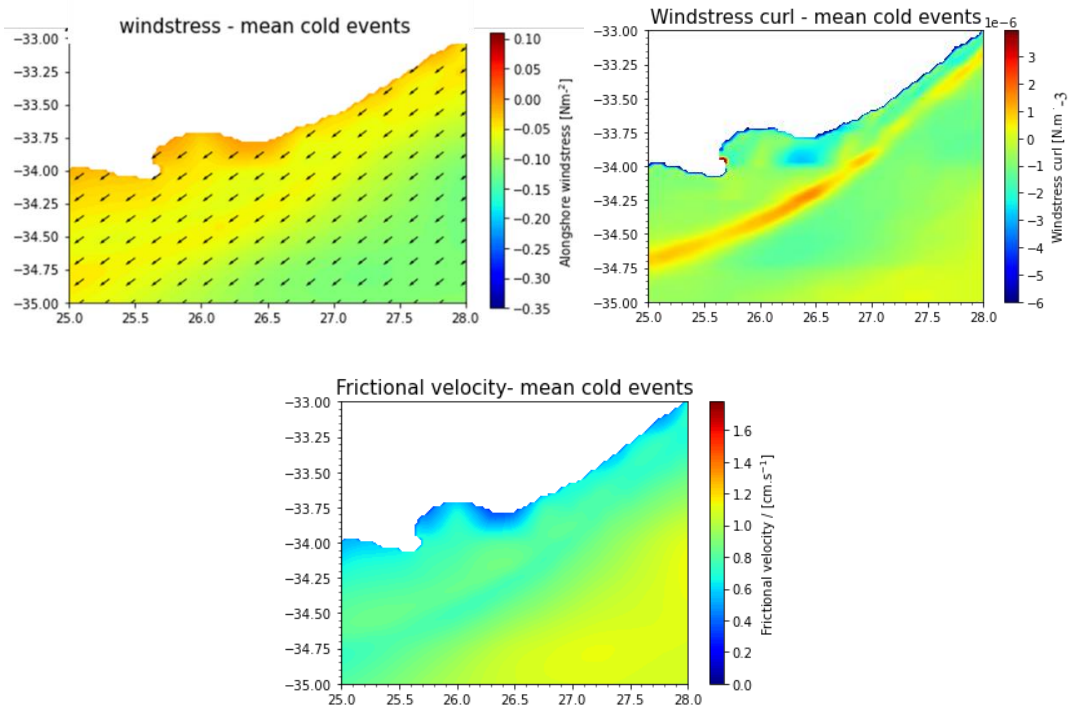

Figure 5.9 Average conditions during 56 selected upwelling events. (from left to right): wind stress, wind stress curl and frictional velocity

Using only the cold water events detected from the sea surface temperature residuals in chapter 4, we plotted a mean composite of the wind stress, wind stress curl and frictional velocity. The alongshore wind stress recorded in the upwelling zone ranges from -0.05 N/m^2 to -0.1 N/m^2 with a dominating

north-east wind component. The wind stress curl ranged mostly from -1 x10^{-6} N/m^3 to -3 x10^{-6} N/m^3 in the upwelling zones. A negative wind stress curl was also an upwelling favourable mechanism leading to surface divergence. Other zones in Algoa Bay were recorded at -4 x10^{-6} N/m^3 while the wind stress curl was much higher in the Agulhas Current zone. Considering the seasonality of wind stress and wind stress curl which did not favour wind-driven upwelling and the short duration of upwelling events from the correlation plots, these 2 composites confirmed that these 56 cold water events were strongly linked to offshore Ekman transport and surface divergence.

The frictional velocity ranged between 0.8 cm/s and 1cm/s in the upwelling region. Since this value is much higher than the average recorded during the monthly state, it is high likely that vertical mixing could also be accounted as a contributing factor for strong upwelling events. Since this was an average of 56 upwelling events, an analysis of individual cases separately would provide a clearer understanding of the influence of atmospheric forcing mechanisms in the next section.

5.4F Case study of selected upwelling events.

After computing the mean state of the upwelling events, we investigated the wind stress and wind stress curl for the 4 chosen case studies from chapter 4 to explore whether wind had an influence on any of these case studies.

Case study 1: Presence of Agulhas Current

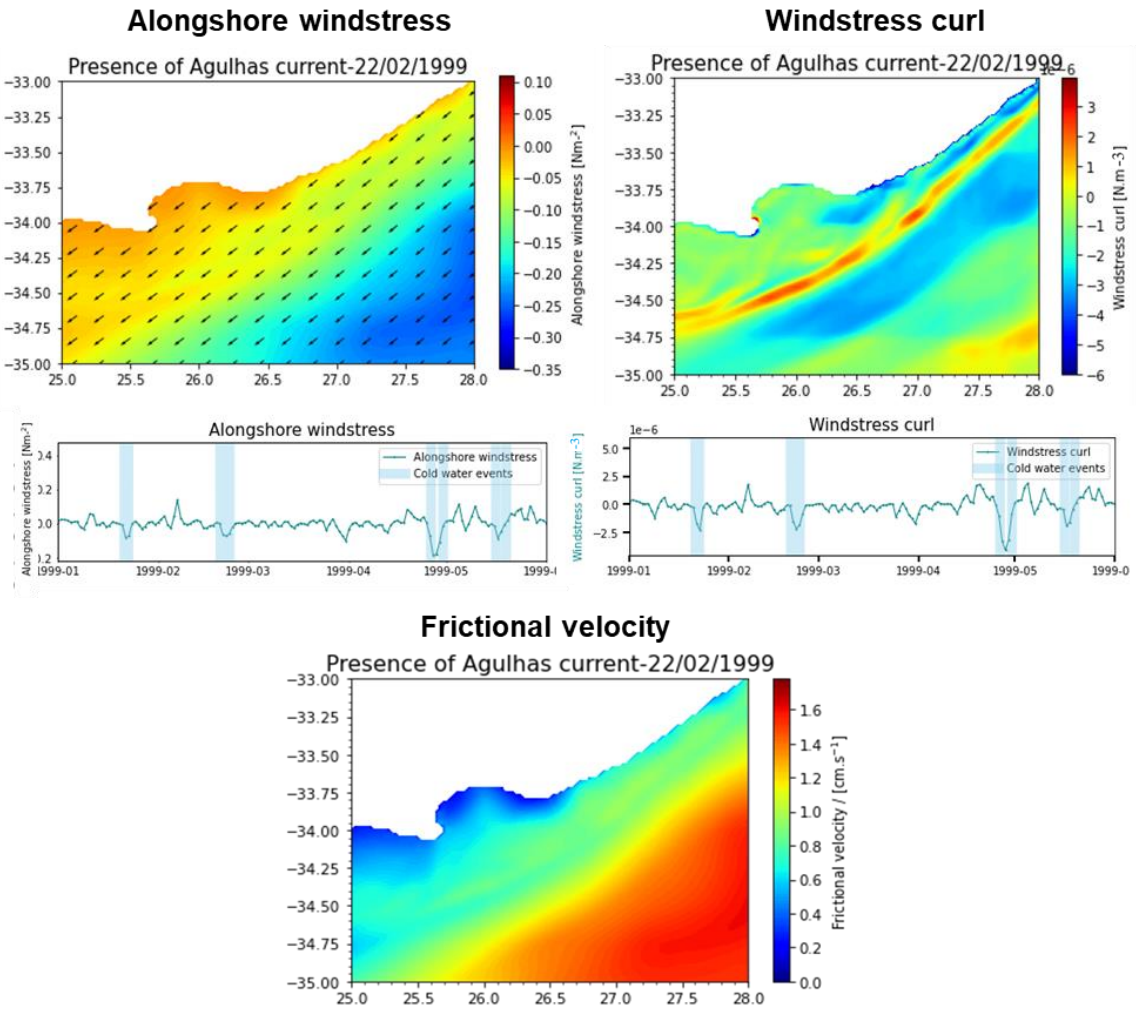

Figure 5.10: 1st row (from left to right) wind stress on the 22nd February 1999, wind stress curl on the 22nd February 1999, 2nd row (from left to right): alongshore wind stress plotted from January to May 1999. wind stress curl plotted from January to May 1999. Detected cold events from upwelling indices were highlighted as light blue along the timeline. 3rd row: Frictional velocity on the 22nd February 1999

The upwelling event on the 22nd February 1999 was defined by the presence of a north-easterly wind component, estimated about -0.1 N/m^2 and showing a gradual decrease towards the offshore region. The wind stress curl also decreased to -2.5 $x10^{-6}$ N/m^3 in the upwelling region. This drop of wind stress and wind stress curl would induce upwelling through its offshore Ekman transport and surface divergence and it was possible that this was mainly a wind-driven upwelling. But the wind stress curl did show a strong convergence in the current zone, sometimes peaking at $2.5x10^{-6}$ N/m^3. The frictional velocity on the other hand was much higher (1.2 cm/s) compared to the other case studies. This reinforced the hypothesis that vertical mixing through turbulence is also a strong contributor to

the Port Alfred upwelling. So, we would still need to explore other oceanographic variables to test whether the strength of the current was also influencing this upwelling on that day.

Case study 2: Presence of meander

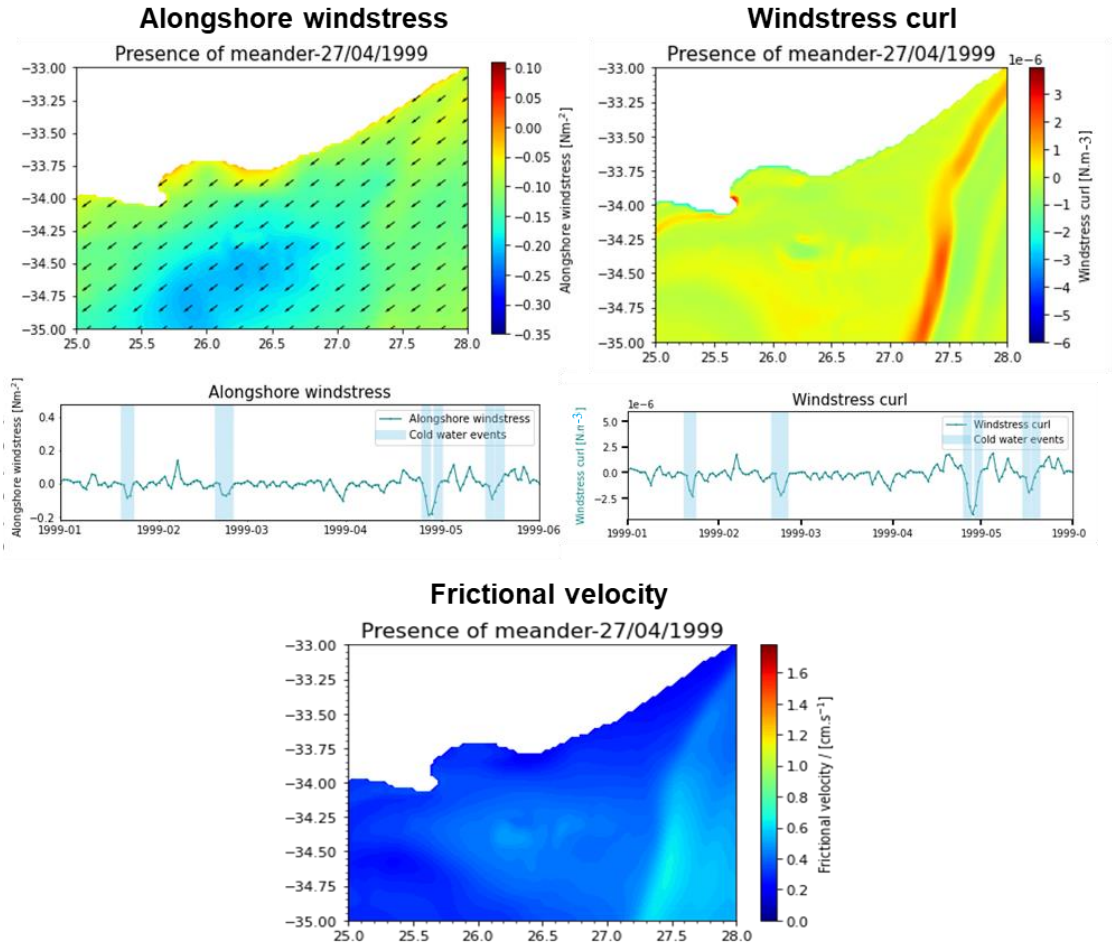

Figure 5.111: 1st row (from left to right) wind stress on the 27th April 1999, wind stress curl on the 27th April 1999, 2nd row (from left to right): alongshore wind stress plotted from January to May 1999. wind stress curl plotted from January to May 1999. Detected cold events from upwelling indices were highlighted as light blue along the timeline. 3rd row: frictional velocity on the 27th April 1999.

On the 27th April 1999, there was very strong presence of the northeasterly wind component everywhere in the region. The alongshore wind stress was recorded to be -0.2 N/m^2 much lower compared to the other cases. It also showed favourable wind stress curl conditions of $-5x10^{-6}$ N/m^3. These values strongly suggested that offshore Ekman transport and surface divergence were contributing to this presence of cold water at the surface. As for the frictional velocity, it was much lower compared to the other case studies. Hence it was unlikely that this upwelling was linked to vertical mixing. However, the meander was another key forcing mechanism present on that day and we could see a further decrease of wind stress further south, ranging between -0.3 N/m^2 to -0.15 N/m^2.

Hence, we would also need to measure other oceanographic fields to investigate whether the eddy was also inducing upwelling as well.

Case study 3: Presence of northeasterly winds

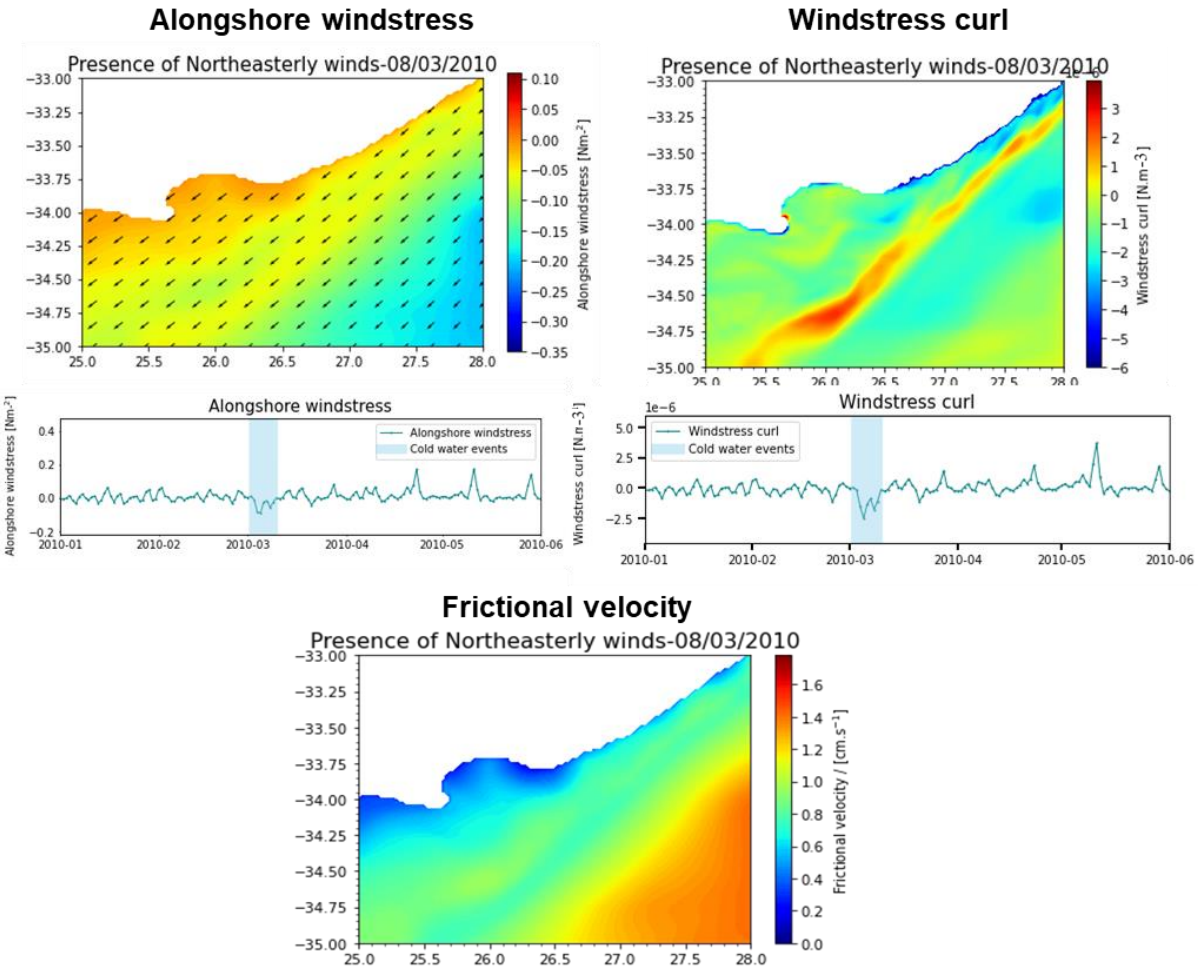

Figure 5.12: 1st row (from left to right) wind stress on the 8th March 2010, wind stress curl on the 8th March 2010, 2nd row (from left to right): alongshore wind stress plotted from January to May 2010. wind stress curl plotted from January to May 1999. Detected cold events from upwelling indices were highlighted as light blue along the timeline. 3rd row: frictional velocity on the 8th March 2010.

On the 8th March 2010 we noted a dominant northeasterly wind component in the region, with a gradual decrease of wind stress as we went offshore. The wind stress was recorded at -0.1 N/m^2 in the upwelling region. As for the wind stress curl, the surface divergence was much stronger in the upwelling region and the wind stress curl ranging between -2.5 $x10^{-6}$ N/m^3 and -1 $x10^{-6}$ N/m^3 in the first week of March 2010. The wind stress curl also defined the presence of the current, with much stronger convergence further south in Algoa Bay. A fairly high frictional velocity from the strong winds was also recorded during this upwelling event, and this indicates possible vertical mixing

through turbulence. After exploring the atmospheric influence, an assessment of its oceanographic fields would provide a better understanding.

Case study 4: Presence of coastal trapped waves

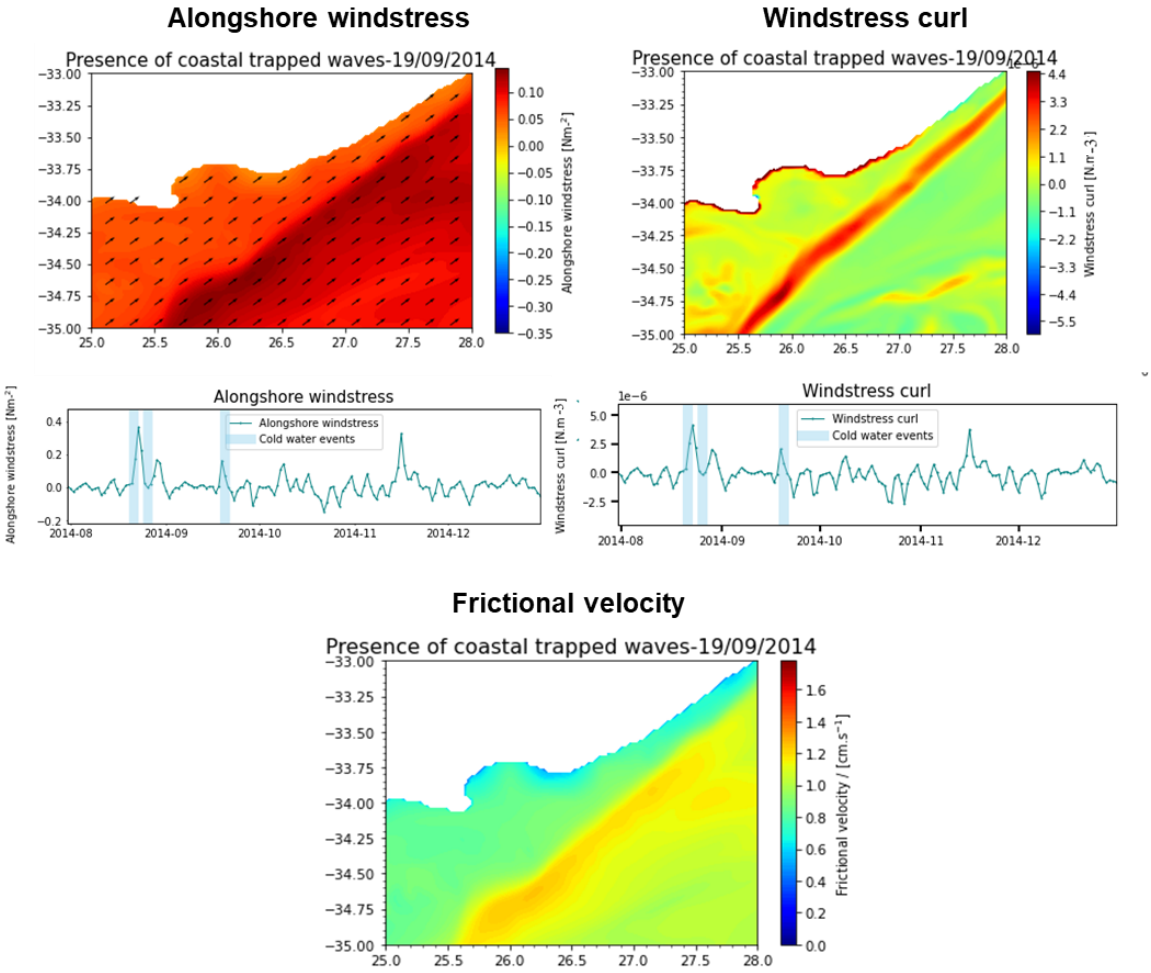

Figure 5.13: 1st row (from left to right) wind stress on the 19th September 2014, wind stress curl on the 19th September 2014, 2nd row (from left to right): alongshore wind stress plotted from January to May 1999. wind stress curl plotted from August to December 2014. Detected cold events from upwelling indices were highlighted as light blue along the timeline. 3rd row: frictional velocity on the 19th September 2014.

The upwelling event on the 19th September 2014 was quite different compared to the previous ones as it displayed a dominating southwesterly wind component, with a very positive wind stress recorded at 0.1 N/m^2 in the upwelling region possibly inducing onshore Ekman transport. The wind stress curl displayed a strong region of convergence delineating the Agulhas Current and recorded a value of 2 $x10^{-6}$ N/m^3 in the upwelling region possibly leading to convergence. Since this case study was associated with a strong presence of coastal trapped waves according to Bailey et al. (2022) and coastal trapped waves were generally linked to westerlies, it made sense that it did not display any

favorable upwelling wind conditions. However, we could still account this upwelling to vertical mixing since it recorded a high frictional velocity of 1cm/s from the strong westerlies.

5.5 Summary and discussion

To understand whether this upwelling was driven by Ekman transport, Ekman pumping or vertical mixing, we explored the wind stress, wind stress curl and frictional velocity generated from the ERA-Interim dataset by ECMWF through the lens of 4 temporal scales. These temporal scales included the seasonal state, the monthly mean, the average conditions during upwelling events and the conditions during a singular upwelling event. However, we also needed to be careful the surface stress components within the ERA-Interim dataset by ECMWF as they had undergone substantial smoothing and had shown considerable fluctuations near the coastline (Hutchinson et al, 2018).

By comparing the monthly mean of the Bakun upwelling index against the model derived vertical velocity, we noted that the vertical velocity was showing a much higher value compared to the upwelling index, indicating possibly other mechanisms as contributing factors. Focussing on the seasonality, summer was mostly characterized by southeasterly winds while winter was strongly characterized by southwesterlies. In the upwelling region, we could find a higher sea surface temperature, a lower wind stress, lower wind stress curl and a lower frictional velocity in summer compared to winter. Hence it was unlikely that the upwelling due to offshore Ekman transport and Ekman pumping was seasonal. As for the correlation plots, it did not include any seasonal influence whereby wind stress and wind stress curl both had a positive/negative correlation with sea surface temperature/vertical velocity. In this case, it was clear that singular events from favourable upwelling winds were very strong and had a short lifespan of 3 to 5 days.

Looking at the mean conditions of the upwelling events, we noted a strong northeasterly wind component, a wind stress of -0.05 N/m^2 and a wind stress curl of $-2x10^{-6}$ N/m^3. Focusing on the case studies of 22nd February 1999, 27th April 1999 and 8th March 2010, they all exhibited upwelling favourable alongshore wind stress and wind stress curl. Some of them also showed possible links to vertical mixing. As for the case study on 19th September 2014, no influence of offshore Ekman transport nor Ekman pumping could be noted on that day. The only atmospheric influence was through vertical mixing. With a further investigation of the oceanographic fields, we would be able to confirm if the current, cyclonic eddies or coastal trapped waves were also additional contributing factors of these upwelling events.

5.6 Highlights

As an overall, this study was conducted to test the hypothesis of the influence of atmospheric influence on the Port Alfred upwelling and 3 new findings from this investigation, highlighting its unique contributions, include:

1) Offshore Ekman transport and Ekman pumping are not the only drivers of Port Alfred upwelling. Vertical mixing can also trigger upwelling strong upwelling events.
2) During summer, upwelling is more likely to be driven by offshore Ekman transport and divergence while stronger southwesterlies are more likely to trigger upwelling through the process of vertical mixing during winter.
3) The distinct presence of shear stress at the inshore front of the Agulhas Current contributes to a strong positive wind stress curl which leads to downwelling along the current's front and strong convergence of floating material along the current.

Chapter 6: Influence of oceanographic forcing on Port Alfred upwelling

6.0 Introduction

After exploring the impact of atmospheric forcing mechanisms on the PA upwelling, we addressed the third research question in this chapter:

What is the influence of oceanographic forcing mechanisms on the Port Alfred upwelling?

From the literature review chapter, we found that aside from the wind, there were many oceanographic forcing mechanisms which could influence this upwelling. It could be triggered by the Agulhas Current (Malan et al, 2013). The presence of mesoscale features like Natal pulses, Durban eddies and shear edge eddies could also lead to upwelling (Goschen et al, 2015). It was also hypothesized that coastal trapped waves flowing from west to east could also trigger upwelling (Malan et al, 2013).

6.1 Ocean properties and tools used to determine presence of currents and mesoscale features

Focusing only on the oceanographic influence on this upwelling, several ocean properties and tools could be explored to measure the intensity of current, presence of meander events and presence of coastal trapped waves.

6.1A Sea surface height

The sea surface height a fundamental oceanographic parameter which has been recorded during several experiments in the Agulhas Current region to study the current and other mesoscale features (Lutjeharms et al, 2003, De Ruijter et al, 1999, Bailey et al, 2022, Leber et al, 2017). Computing this term from numerical models in the Port Alfred region can indicate the presence of the Agulhas Current since western boundary currents are associated with elevated sea surface heights due to their high transport of warm water. Measuring the sea surface height is also useful when a coastal trapped wave would interact with the coastline. In areas where the wave energy is concentrated, a temporary rise in sea level will occur due to the convergence of wave energy (Bailey et al, 2022). As for Natal pulses, border edge eddies and Durban eddies, this will reflect as a decrease in sea surface height (Lutjeharms et al, 2003).

6.1B Ocean velocity

Ocean velocity allows researchers to analyse the intricate dynamics of the ocean flow through different methods and has previously been measured on several occasions in the Agulhas Current

region (Beal, 1997, Malan, 2013, Garzoli, 1992; Leber et al, 2017). Oceanographers can compute its speed and direction at the surface and subsurface levels to identify major currents, eddies and ocean circulation patterns. Bottom ocean velocity offers insights into the vertical water movement near the ocean floor and the understanding of the interactions between currents and the ocean floor (Malan, 2013). Geostrophic velocity can also be computed from the gradients of sea surface height with respect to latitude and longitude (Garzoli, 1992). It is a theoretical concept derived from the balance between the Coriolis effect and the pressure gradient force (Garzoli, 1992). Measuring the geostrophic velocity helps us to detect any mesoscale changes in the region. When a cyclonic eddy flows on the inshore edge of the Agulhas Current, the direction of the current is flowing towards the north east direction at the leading edge of the eddy, inducing a rise in the geostrophic velocity while it is also indicating a south west direction at the trail of the eddy, displaying a negative change.

6.1C Bottom Ekman transport

Bottom stress, simulated in numerical models, represents the force exerted by the flow at the ocean bottom and this property influences major ocean currents and coastal circulation patterns (Lin et al, 2023). Bottom Ekman transport can also be derived from the bottom stress to indicate the net movement of water near the ocean bottom due to Ekman transport (Lin et al, 2023). The presence of a strong Agulhas Current on the shelf would be determined by an increase of the bottom stress and in bottom Ekman transport due to its interaction against the continental shelf. However, if the current would meander and flow further from the coast, it would cause a decrease in the bottom stress and a decrease in the bottom Ekman transport in the upwelling region.

6.1D Vorticity

The computation of vorticity also contributes to the identification of regions with strong vortical motion, aiding in the assessment of eddy formation and behavior as well as detecting the presence of ocean currents. There are several methods to investigate the vorticity. For instance, relative vorticity is the measure of rotation of a fluid element relative to its surrounding fluid, absolute vorticity is the sum of the relative vorticity and planetary vorticity and potential vorticity is the ratio of absolute vorticity to the vertical spacing between pressure surfaces (Hunt et al, 1988).

6.1E Generalized Ekman pumping

Computing the linear and non linear terms of the generalized Ekman pumping equation is another great tool for assessing the oceanographic features. This method allows us to outline the dominant terms influencing the vertical pumping at a specific depth in the ocean (Djakoure et al, 2017). These terms include the planetary vorticity associated with Earth's rotation, the wind stress curl, the advection of momentum (inertia), and the viscous flux associated with friction. Each term captures a different physical process contributing to the vertical motion of water masses at the specified depth. Djakoure et al (2017) investigated the vorticity equation balance in the northern Gulf of Guinea and

found that the effect of the advection of the momentum through the detachment of the Guinea Current from the coast is a primary driver of coastal upwelling east of Cape Palmas, while the beta effect and wind stress curl also contribute to the vertical movement of water.

6.1F Current tracker algorithms

Current tracker algorithms can enhance our understanding of current dynamics by monitoring the movement of specific features over time for identifying and tracking phenomena such as mesoscale eddies and coastal currents. Prior research in the Agulhas region involved variations in the current's position using a range of data sources and methodologies. Krug and Tournadre (2012) employed satellite-derived Sea Surface Temperature and sea surface height data to delineate the core and boundaries of the Agulhas Current around 34°S. Their objective was to assess the Agulhas Current's variability. Malan et al. (2018) also relied on simulations from two numerical models and satellite altimetry data focused around 34°S to pinpoint the Agulhas Current's core position. This effort aimed to analyze how the meanders influence the interactions between the current and the shelf. Braby et al. (2020) used sea surface height datasets from remote sensing and a numerical model to ascertain the Agulhas Current's location. Recently, Russo et al (2020) demonstrated an upgraded method on the detection of the Location of the Agulhas Current's Core and Edges (LACCE) in the South western part of the Indian ocean by using the daily sea surface height and geostrophic velocities from remote sensing products.

6.1G Eddy tracker algorithms

Eddy tracker algorithms monitor the movement and evolution of eddies over time, contributing to the study of eddy dynamics. These algorithms are essential for tracking the paths, sizes, and lifetimes of eddies, helping researchers understand their impact on oceanic processes. With an increased focus on meander events in the Agulhas region, eddy tracking algorithms would also be useful in the detection of Natal pulses, border edge eddies and Durban eddies. There was a wide variety of eddy tracker algorithms which were available. In the past, eddies garnered interest due to their significant influence in the dynamics of mesoscale circulation. During recent years, many automated eddy tracking algorithms emerged, contributing to our understanding of eddy characteristics and their variability. These techniques encompassed three primary methods: geometric (e.g., Chaigneau et al. 2008; Nencioli et al. 2010); Okubo–Weiss (Chelton et al. 2007); and wavelet (Doglioli et al. 2007).

6.3 Aims and objectives

Through this chapter, we aimed at providing a detailed description by investigating the influence of the Agulhas Current and other mesoscale features on the Port Alfred upwelling at different temporal scales. This chapter involved 3 research questions.

6.3A What is the influence of the Agulhas Current on the Port Alfred upwelling zone?

We investigated the different terms of the vorticity equation balance as well as calculated the geostrophic velocity, surface ocean velocity, bottom ocean velocity, bottom stress, bottom Ekman transport and sea surface height to investigate the influence of the Agulhas Current on the upwelling at varying temporal scales.

6.3B What is the influence of meanders on the Port Alfred upwelling zone?

We used some of the previous ocean properties as well as 2 methods for measuring the occurrence of meanders, namely the LACCE algorithm and the PY eddy tracker algorithm to track meander events in the region at different temporal scales.

6.3C What is the influence of coastal trapped waves on the Port Alfred upwelling zone?

We also explored the potential influence of coastal trapped waves on the upwelling by investigating its sea surface height and using the LACCE algorithm at different temporal scales.

6.4 Data and methods

6.4A Oceanographic forcing variables

To address these key questions, firstly we computed the terms of the generalized Ekman pumping equation during the mean state. We then computed the sea surface height, surface and bottom ocean speed, geostrophic velocity, bottom stress, bottom Ekman transport, minimum distance between the core of the current and the upwelling region, eddy radius, eddy amplitude and the eddy area at various temporal scales. We explored their seasonality, the mean state during the 56 upwelling events and their conditions during the 4 upwelling events chosen from chapter 4 and their correlation with sea surface temperature and vertical velocity.

6.4B Generalized Ekman pumping equation

The terms of the generalized Ekman pumping were computed (see section 3.2G from chapter 3) for the mean state.

$$\underbrace{w(z_0)}_{Pumping} = -\underbrace{\frac{\beta V}{f}}_{Planetary} + \underbrace{\frac{\nabla \times \tau}{\rho_0 f}}_{WindCurl} + \underbrace{\frac{\nabla \times ADV}{f}}_{Inertia} + \underbrace{\frac{\nabla \times KFLX}{f}}_{ViscousFlux}$$

This diagnostic has been obtained through the integration of the vorticity equation. This equation can be broken down into 4 terms: the planetary vorticity (β), wind stress curl, advection of momentum (inertia) and viscous flux (associated with friction). These terms represent the contributions of different physical processes to the generation and evolution of vorticity in the ocean. The Beta effect term describes the variation of the Coriolis parameter with latitude. The wind stress curl term describes the curl of the wind stress vector, which is the force exerted by the wind on the surface of

the ocean. It represents the tendency of the wind to generate vorticity in the ocean. The advection of momentum term describes the transport of vorticity by the horizontal flow of water. As for the viscous flux term, it indicates how the effects of friction contribute to the curling of vorticity.

In order to identify the most dominant term contributing to the upwelling, the equation is integrated over the depth of the layer, and the resulting value is used to determine the vertical movement of water. The buoyancy frequency and Coriolis parameter are physical constants, while the horizontal velocity is obtained from the model output. The depth of the base of the layer is set to 75 m. The reconstructed vertical pumping derived from the vorticity equation balance is then compared with the model-derived vertical velocities to validate the model output and the reconstructed vertical pumping. A gaussian filter smoothing technique is also applied.

6.4C Oceanographic forcing variables from CROCO simulations

The sea surface height was directly generated from the CROCO simulations. We computed the ocean speed at the surface and at the bottom by using this equation:

$$V_{\text{ocean}} = \sqrt{u^2 + v^2}$$

Whereby *u* is the eastward velocity component and *v* is the northward velocity component. The geostrophic velocity was calculated as followed:

$$V_g = \frac{g}{f}\frac{\partial SSH}{\partial x}$$

whereby V_g is the northwardward geostrophic velocity along the slope, f is the Coriolis force, g is gravity, $\frac{\partial SSH}{\partial x}$ is the gradient sea surface height in the eastward direction.

Bottom stress was also calculated as followed:

$$\tau_b = \rho_o C_d \sqrt{u_b^2 + v_b^2}$$

τ_b is the linear bottom stress whereby ρ is the seawater density, C_d is drag coefficient (C_d = 0.001 based on Perlin et al. (2005)), u_b and v_b are the current velocity at the seafloor.

$$Ek_b = -\frac{\tau_b}{f}$$

where τ_b is the bottom stress which was directly generated from the CROCO simulations and f is the Coriolis parameter, which is a function of latitude and represents the effect of the Earth's rotation on ocean currents.

6.4D Current tracker algorithm: LACCE

We used the LACCE algorithm to measure the minimum distance from the Port Alfred upwelling to the location of the current's core. The LACCE algorithm, an operational monitoring tool (OCIMS, www.ocims.gov.za), was founded on a technique introduced by Braby et al. (2020). In their study, Braby et al. (2020) successfully determined the current's core location along South Africa's east coast by extracting daily mean Absolute Dynamics Topography (ADT) from gridded altimetry data. The LACCE algorithm, built upon a similar contour-fitting approach as Braby et al. (2020), possessed noteworthy advantages (Russo et al, 2020). Specifically, it had the ability to connect distant regions seamlessly and offer a continuous and easily interpretable representation of the current's position (Chapman et al. 2020). LACCE represents one of the pioneering techniques capable of daily tracking of the Agulhas Current's core, inner and outer edges across the entire Agulhas System (Russo et al, 2020).

6.4E Eddy tracker algorithm: Py eddy

We also used the Py eddy tracker algorithm to detect eddy activity and we generated its eddy radius, eddy amplitude and eddy area. The Py-eddy-tracker sea level-based method, inspired by Kurian et al. (2011), and Penven et al. (2005), made use of sea surface height anomalies data from AVISO. Eddy track coordinates and its properties were mapped using the Py eddy tracking code (Mason et al., 2017) which relied on daily 0.25° × 0.25° altimetric all-sat gridded sea level anomaly data (Capet et al., 2014) from AVISO. This dataset incorporated observations from multiple altimeter missions, providing improved mesoscale feature resolution compared to the two-sat reference product (Ducet et al., 2000). The domain boundaries for this tracking algorithm encompassed the region from 25°E to 28°E longitude and from 33°S to 35°S latitude. Eddy characteristics, such as position, date, eddy radius, eddy amplitude and eddy area were recorded at each time interval.

6.5 Results and Discussion

6.5A Influence of the Agulhas Current on the Port Alfred upwelling zone

Comparing the vertical pumping and model derived vertical velocity

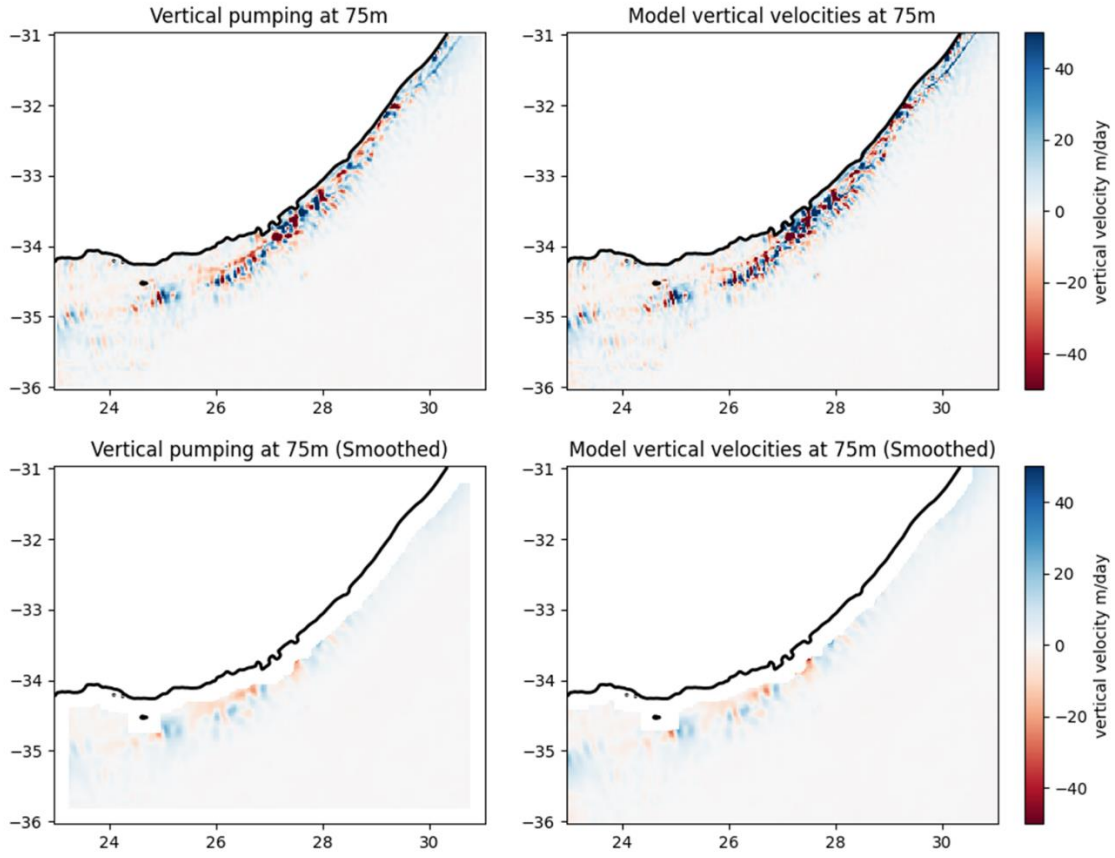

Figure 6.1: first row (from left to right) Reconstructed vertical pumping (m/day) and model mean vertical velocities at 75 m (m/day), 2nd row Smoothed reconstructed vertical pumping (m/day) and smoothed model mean vertical velocities at 75 m (m/day)

The mean state of the vertical pumping and model derived vertical velocity were plotted in figure 6.1. Their signal contains high-frequency variations and these noise signals prevent us to identify and analyse relevant features, hence we applied a gaussian filter to emphasize the overall trends or variations while suppressing small-scale fluctuations. The vertical pumping ranged from -188 to 122m/day while the model derived vertical velocity ranged from -224 to 170 m/day. We recorded an overall average a vertical velocity of 0.43m/day from the model derived vertical velocity and a vertical pumping of 0.56m/day from the vorticity equation from the surface to a depth of 75m. We also calculated the vertical velocity from 2 upwelling sites along the inshore edge of the current. In the Port Alfred region, the vertical pumping was 3.66 m/day while the model derived vertical velocity was 3.75 m/day. As for the Durban region, the vertical pumping was -0.11 m/day while the model derived vertical velocity was -0.12 m/day. These comparisons between the model-derived vertical

velocity and the reconstructed vertical pumping (w_0) from the vorticity equation indicated that they good agreement, showing that the robustness of the reconstruction.

Planetary vorticity and wind stress curl from the generalized Ekman pumping equation

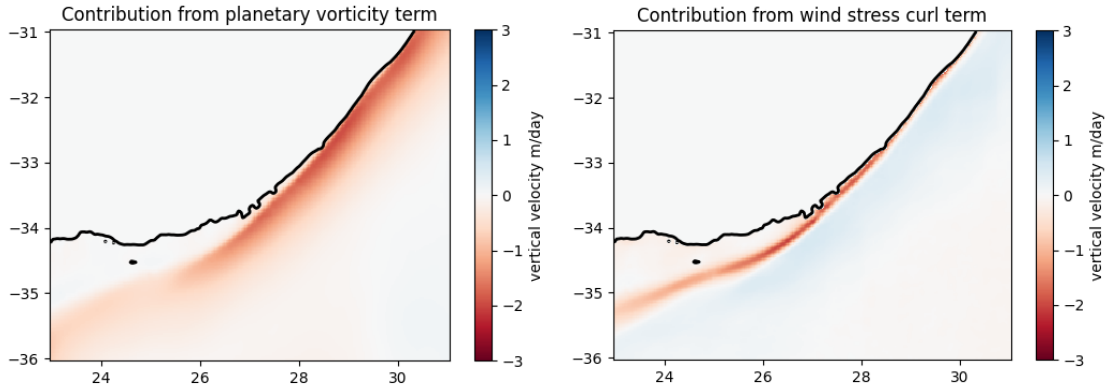

Figure 6.2: (from left to right) planetary vorticity term (m/day) and wind stress curl at 75 m (m/day),

In the Port Alfred region, the beta effect was found to be a minor contributor downwelling. Overall, it recorded a vertical velocity of -0.33m/day in the Agulhas Current region and would not show any contribution to upwelling. From the beta effect, we noted a vertical velocity of -1.11 m/day in Port Alfred region and -0.95 m/day in the Durban region. As for the wind stress curl, it could not be accounted to the vertical pumping. It was also found to be mostly forcing downwelling on the inshore edge of the current, with a more pronounced downwelling further south, with a recording of -1.0 m/day in the Port Alfred region, -0.5 m/day in the Durban region and an overall average vertical velocity of -0.19 m/day.

Advection of momentum term from the generalized Ekman pumping equation

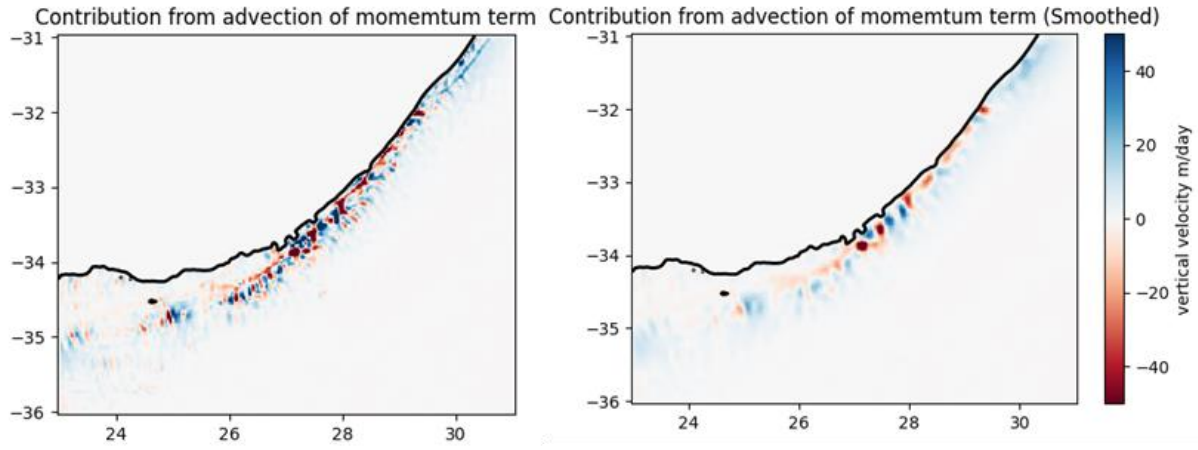

Figure 6.3:(from left to right) Advection of momentum term (m/day) and applied smoothing to advection of momentum at 75 m (m/day),

In figure 6.3, we plotted the contribution of vertical velocity of the advection of momentum term and the smoothed one. The advection of momentum is the non linear term from the equation which plays a crucial role in explaining the generation and maintenance of the turbulence of the current through the horizontal flow of water. This process proves to be mainly responsible for the strong vertical pumping observed on the inshore edge, reaching a maximum of 122m/day. It recorded an overall average vertical velocity of 0.58 m/day during the mean state, 4.22 m/day in the Port Alfred region and 0.89 m/day in the Durban region. This reinforces the hypothesis that during the mean state, the advection of momentum is the inertial term which causes the detachment of the current. This in turn leads to a higher divergence and increases the vertical velocity.

Viscous flux term from the generalized Ekman pumping equation

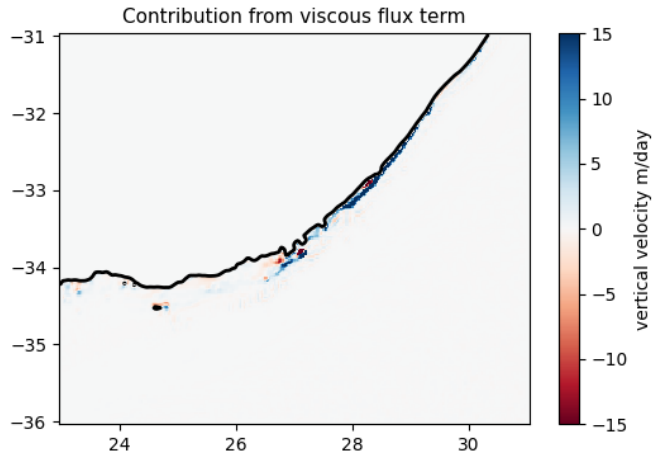

Figure 6.4: (from left to right) viscous flux term at 75 m (m/day),

In Figure 6.4, we plotted the contribution of vertical velocity of the viscous flux term from the vorticity equation. Here it captures how this shearing effect, associated with friction, influences the rotation and curling of vorticity. The vertical velocity ranged from -77 to 93 m/day whereby 0.5m/day was recorded in the Port Alfred region, -0.15 m/day in the Durban region and the overall average recorded was 0.15 m/day. This term becomes significant especially in regions where there is friction along the continental slope, hence showing it is also a minor contributor to the upwelling during the mean state.

6.5B Sea surface height

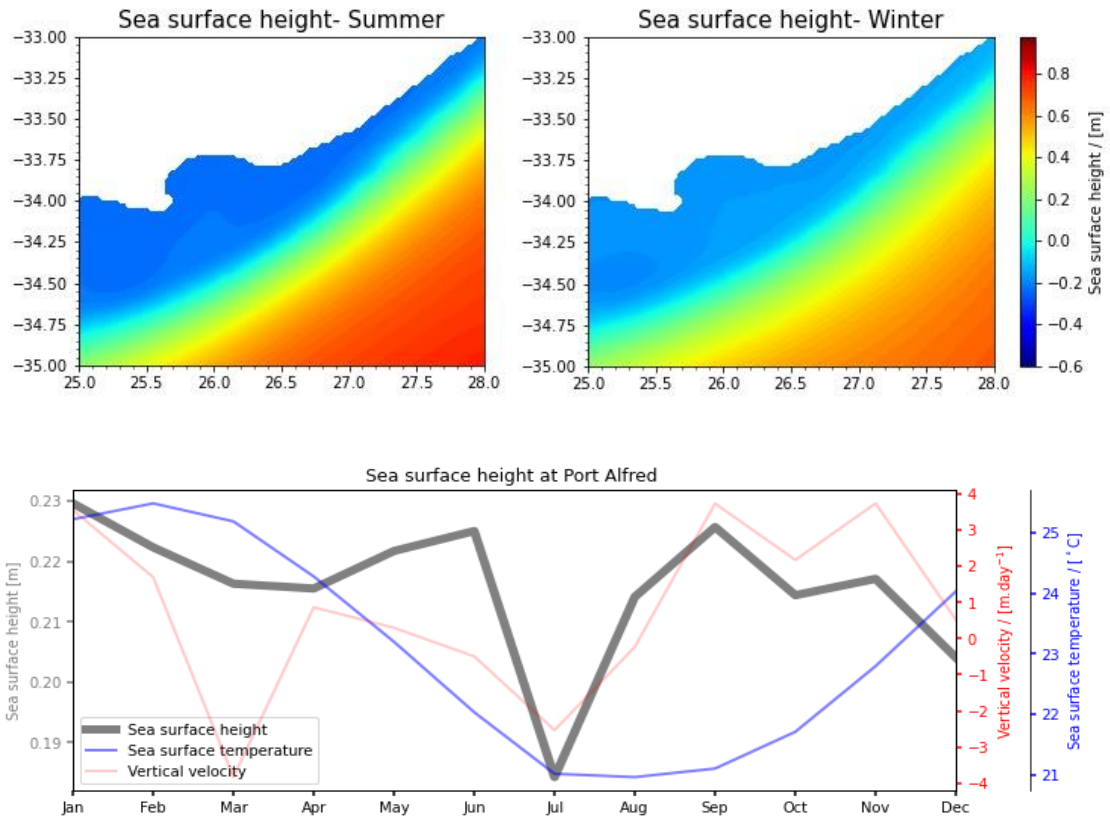

Figure 6.5: 1st row (left to right) - summer and winter sea surface height, 2nd row (left to right) – monthly mean of sea surface height, sea surface temperature (blue line) and vertical velocity (red line)

The seasonal variations showed that the sea surface height for both winter and summer was relatively smaller compared to the Agulhas region. It had a slight peak (-0.15m) around the winter month June and September. In the Agulhas Current zone, the sea surface height varied between 0.2 and 0.4m in summer, but this decreased in winter, ranging from 0 to 0.3m. An increase in sea surface height could also be influenced by the high occurrence of coastal trapped waves in the region as well. Looking at its seasonality, it exhibited a strong presence of the Agulhas Current, especially in summer. This could in turn lead to an increase of upwelling events in summer through the detachment of the current as well as through onshore bottom Ekman transport, especially if other upwelling favorable forcing mechanisms would be present (such as coastal trapped waves or north easterly wind component). It did not capture any eddy activity in summer, although there seemed to be a slight circular motion of sea surface height closer to the Algoa bay in winter.

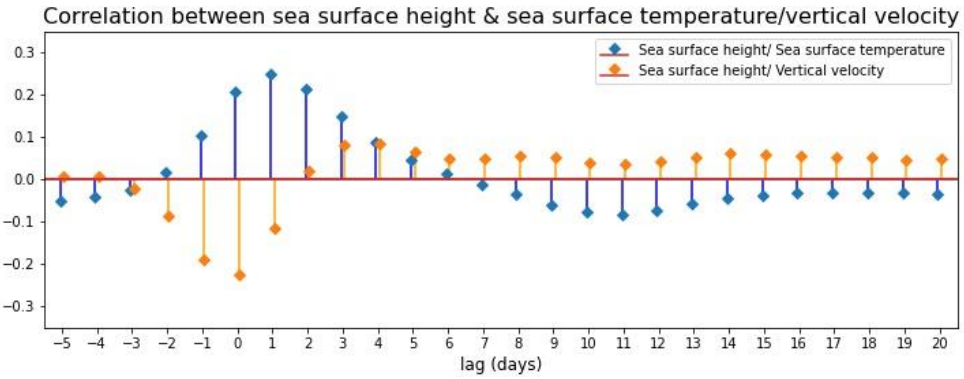

Figure 6.6: Correlation between sea surface height and sea surface temperature/vertical velocity

Assessing the correlation between sea surface height and upwelling events, we see that the majority of upwelling events showed a decrease in sea surface height and would last between day -2 to day 5. It had a positive correlation of 0.25 with sea surface temperature on day 1 and a negative correlation of 0.25 on day 0 with vertical velocity. This correlation was similar to the study conducted by Leber et al. (2018) whereby they recorded a positive correlation of 0.21 between sea surface temperature and sea surface height. This would translate to an upwelling due to the occurrence of a cyclonic eddy. As an eddy's leading edge approached on the inshore edge, the vertical velocity would show a negative correlation of 0.1 on day -2 while the sea surface temperature showed a positive correlation of 0.1 on day -1. The correlation would slightly decrease during the passage of the center of the eddy. This type of upwelling would quickly be characterized by downwelling as onshore Ekman transport would occur at the trailing edge of the eddy. On day 3, the vertical velocity had a correlation 0.1 was noted while the sea surface temperature showed a correlation of -0.1 on day 8. Since the correlation did not show any negative/positive correlation with sea surface temperature/vertical velocity, this could suggest that an upwelling on average was not linked to the presence of the current or coastal trapped waves.

6.5C Ocean velocity

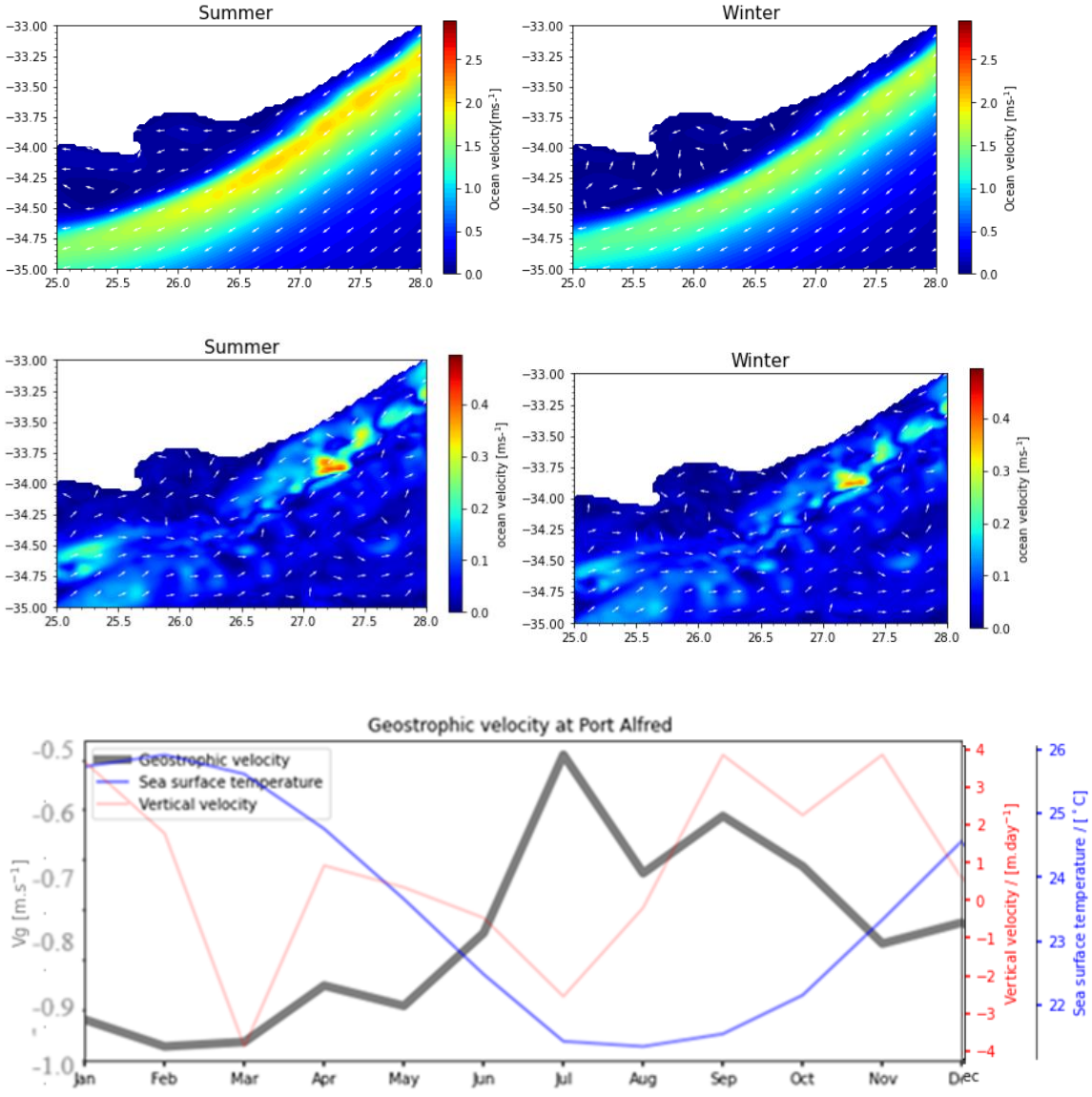

Figure 6.7: 1st row (left to right) - summer and winter sea surface velocity, 2nd row (left to right) - summer and winter bottom velocity, 3rd row– monthly mean of geostrophic velocity, sea surface temperature (blue line) and vertical velocity (red line)

As we examined the surface velocity, in summer, higher values of the velocity was recorded compared to winter. The core of the current ranged approximately between 1.8 to 2.1m/s, while in winter, it varied between 1.4 to 1.8m/s. During winter, it could also be noted from the arrows, that there seemed to be a rotational flow which possibly captured eddy activity in the Algoa Bay. The current showed a flow from a north east to a south west direction, indicating negative geostrophic velocity in both summer and winter. In February, it recorded a velocity of -1m/s while there was a slight peak of -0.5 m/s in July. This could either be due to a weakening of the Agulhas Current or

more eddy activity in winter. As for the bottom velocity, the geostrophic velocity was positive in both summer and winter and ranged between 0 to 0.5m/s.

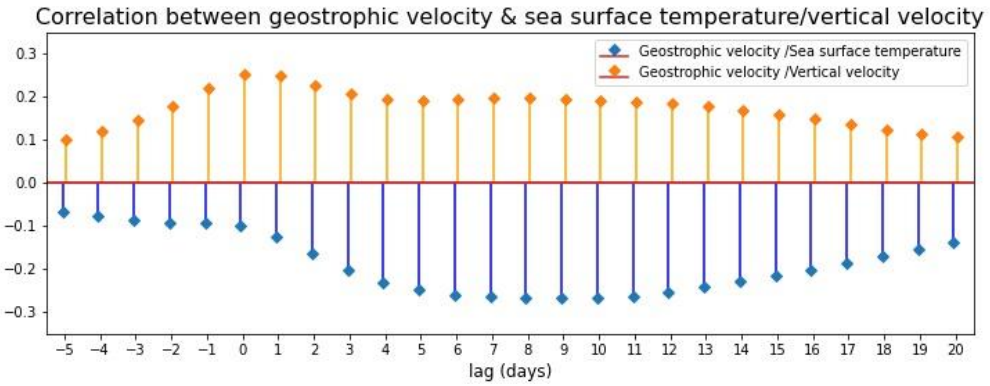

Figure 6.8: Correlation between geostrophic velocity and sea surface temperature/vertical velocity

The correlation analysis revealed some noteworthy links. Geostrophic velocity exhibited a positive correlation with vertical velocity, ranging from 0.1 to 0.25, while it displayed a negative correlation with sea surface temperature, ranging from -0.1 to -0.25. Leber et al. (2017) also observed a negative correlation of -0.3 between sea surface temperature and geostrophic velocity, typically associated with the passage of a cyclonic eddy. As the current meandered, geostrophic velocity tended to increase at the leading edge of the eddy and decrease at the trailing edge, a pattern consistent with cyclonic eddy behavior. Intriguingly, this correlation persisted for a duration exceeding one month. This extended duration could suggest the presence of a Natal pulse, although it was important to consider the potential influence of seasonal factors. During the winter season, meander events were more frequent due to the presence of circular motion of velocity in the model. Additionally, the Agulhas Current weakened, and sea surface temperature decreased during this season, contributing to the possible prolonged correlation observed.

6.5D Bottom stress and bottom Ekman transport

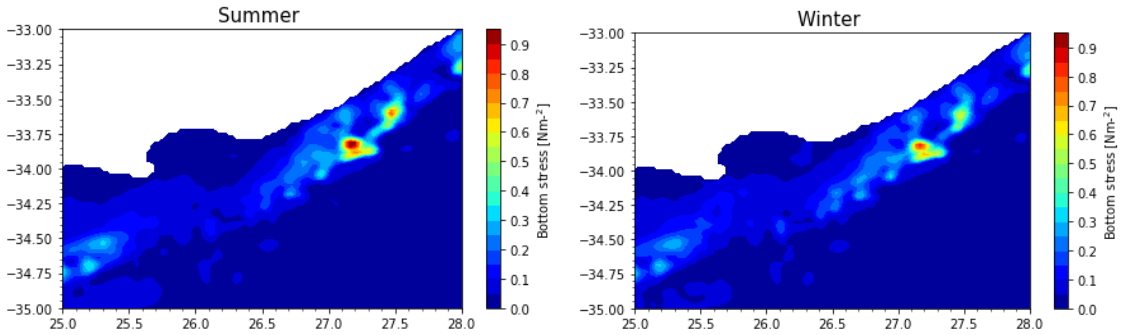

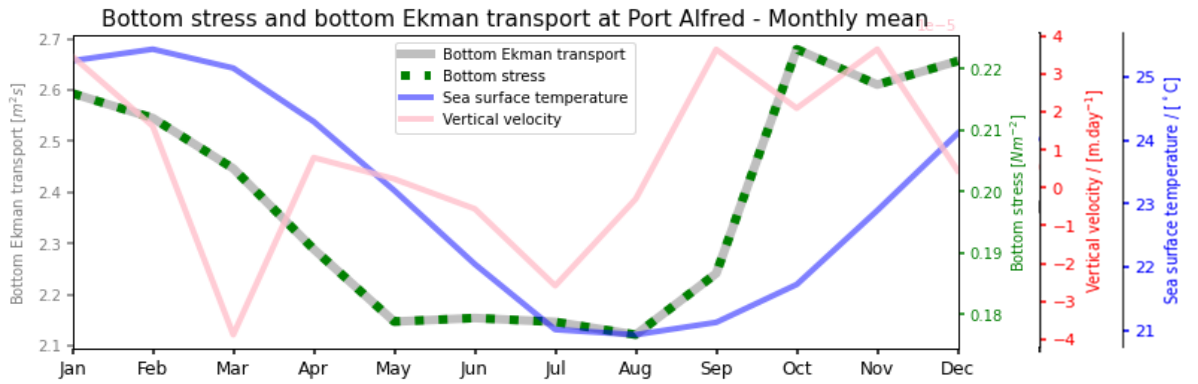

Figure 6.9: 1st row (left to right) - summer and winter bottom stress, 2nd row (left to right) – monthly mean of bottom Ekman transport (grey line), bottom stress (dotted green line), sea surface temperature (blue line) and vertical velocity (red line)

The seasonality of the bottom stress in the upwelling zone varied between 0.15 N/m^2 to to 0.2 N/m^2 in summer and winter while in the current zone, it ranged from 0.2 N/m^2 to to 0.9 N/m^2. However a slight decrease of bottom stress was noted in winter. In the Southern hemisphere, the negative Ekman transport signifies an onshore (toward the coast) transport. The bottom Ekman transport was computed and ranged from 2.1 m^{2}s^1 to 2.7 m^{2}s^1 in the Port Alfred region. It showed a slight decrease in the month of August possibly due to the weakening of the current in winter. The seasonality of the bottom dynamics seemed to show a strong presence of the onshore Ekman transport throughout the whole year.

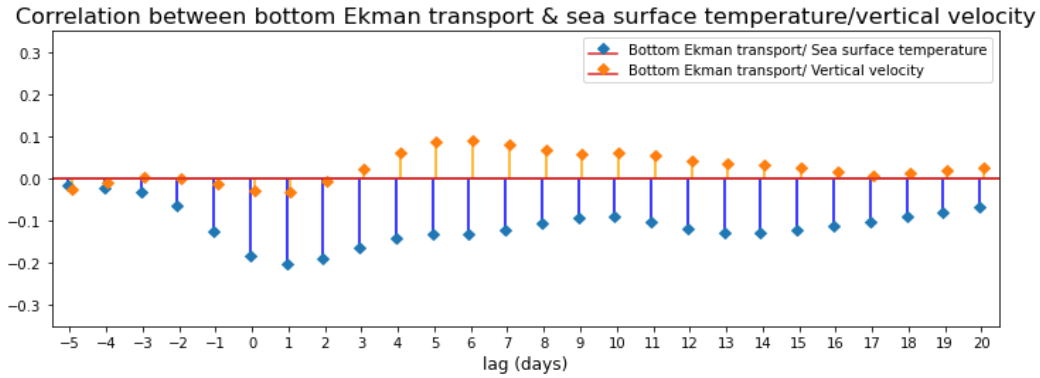

Figure 6.10: Correlation between bottom Ekman transport and sea surface temperature/vertical velocity

Investigating the link between the bottom Ekman transport and upwelling events, we noted a negative correlation with sea surface temperature ranging from 0 to -0.2, peaking on day 1. This correlation plot indicated how an increase in bottom Ekman transport from a strong current would lead to a decrease in sea surface temperature. As for the vertical velocity, it took 4 days until there was a positive correlation between vertical velocity and bottom Ekman transport. This showed that a peak in the bottom stress can take a few days before inducing upwelling.

6.5E Detection of eddies and core of the current

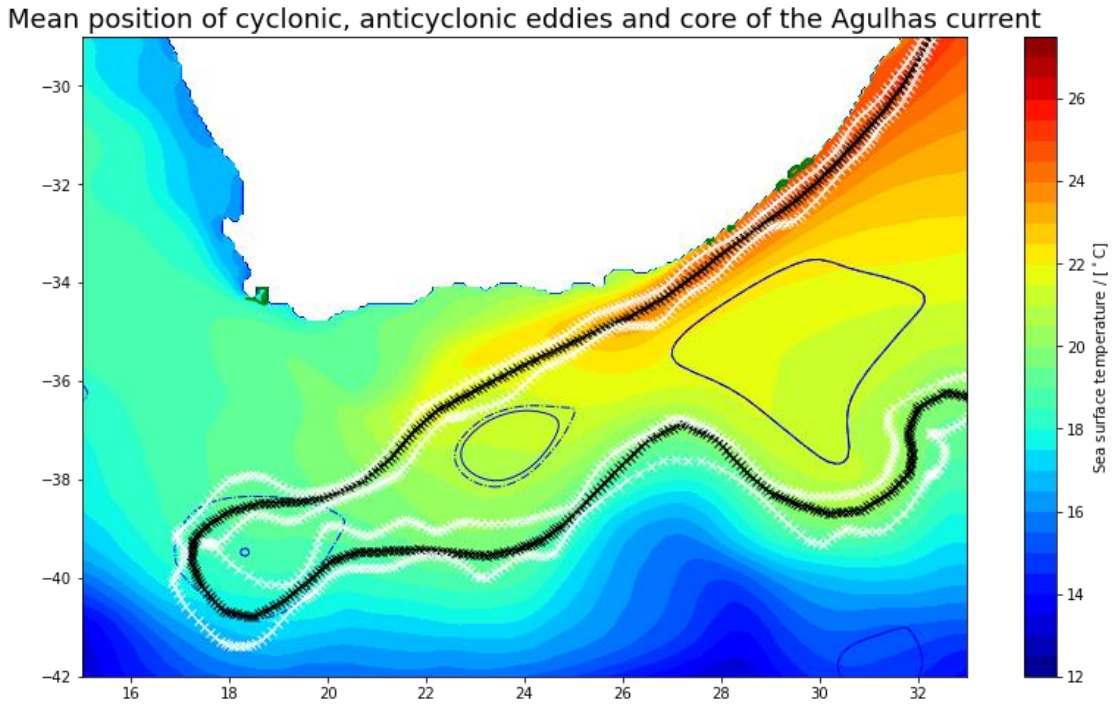

Figure 6.11: Mean position of cyclonic, anticyclonic eddies and the core of the Agulhas Current overlaid on the mean sea surface temperature. Core of the current (Black line), inner and outer edge of the current (white lines) generated from the LACCE algorithm, anticyclonic eddies (blue line) and cyclonic eddies (red line) generated from the PY eddy tracker algorithm.

After computing the sea surface height, ocean velocity, bottom stress, bottom Ekman transport, we used the LACCE algorithm to generate the position of the core of the current as well as the Py eddy tracker algorithm to generate the position of major and minor cyclonic and anticyclonic eddies. Looking at the whole Agulhas region during its mean state, the current did not capture big meander activity on its inshore edge except some minor cyclonic eddies were present upstream. 2 large and 1 minor anticyclonic eddies were also detected on the offshore edge of the Agulhas Current.

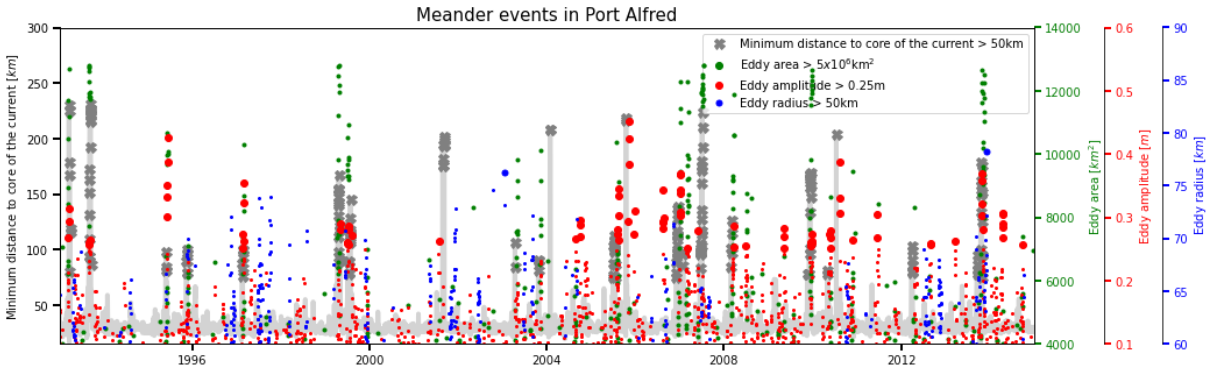

Figure 6.12: Daily time series of minimum distance between Port Alfred upwelling and core of the current generated from the LACCE algorithm (grey line), PY eddy tracker variables: eddy area (green dots), eddy amplitude (red dots) and eddy radius (blue dots).

Focusing on the upwelling region, we computed the minimum distance between Port Alfred and the core of the current as well as used the Py eddy tracker algorithm to compute the eddy radius, the eddy amplitude and the eddy area to measure the meander events. The model outputs suggested that on average in one year, 1.9 large meander events were generated from the distance between the current and the upwelling zone, 2.2 large meander events from the eddy amplitude, 1.5 large meander events from the eddy area and 1.3 large meander events from the eddy radius were recorded. These 4 variables compared relatively well with the 1.8 large meanders per year computed by Russo et al (2021) by applying the LACCE algorithm using satellite data from 1993 to 2020. This dataset was measured further downstream in Gqeberha. In another study Krug et al. (2014) had also measured the meander events upstream from 1992-2012 and identified 1.7 large meander events per year. Russo et al (2021) had also applied the LACCE algorithm to reanalysis datasets and noted that there was an overestimation of meander events. They identified 2.5 large meanders per year using Mercator Ocean's Global Re-analysis (GLORYS), 2.9 large meanders per year from the Bluelink Reanalysis dataset (BRAN) and 3.4 large meanders from the Hybrid Coordinate Ocean Model (HYCOM) reanalysis dataset. This overestimate was also consistent with the calculation of the EKE in northern Agulhas region, hence it was likely that these models in the reanalysis datasets could not resolve the energy dissipation processes, and this could affect the position of the current downstream (Braby et al., 2016).

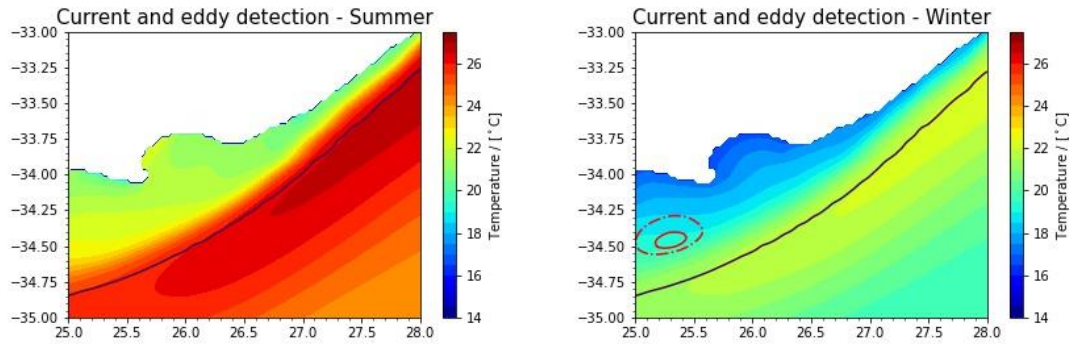

Figure 6.13: Position of the current's core (black line), strong cyclonic eddy (red line) and weak cyclonic eddy (dotted red line) overlaid on sea surface temperature for summer (left) and winter (right).

The seasonality showed that the position of the current's core was closer to the coastline compared to winter. A minor eddy activity was also detected in winter closer to the Algoa Bay however no presence of coastal trapped waves was captured from the LACCE algorithm. Even though the continental shelf is very wide in this region, a closer proximity to the coast would induce upwelling due to the conservation of potential vorticity and the narrowing of its inertial jet. This type of upwelling would possibly not be strong enough to reach the surface, but with additional upwelling forcing mechanisms, it could be more prominent in summer. Both the LACCE and Py-eddy tracker algorithm were in agreement that there was a continuous permanent flow of the current with no display of potential meander activity in the upwelling zone.

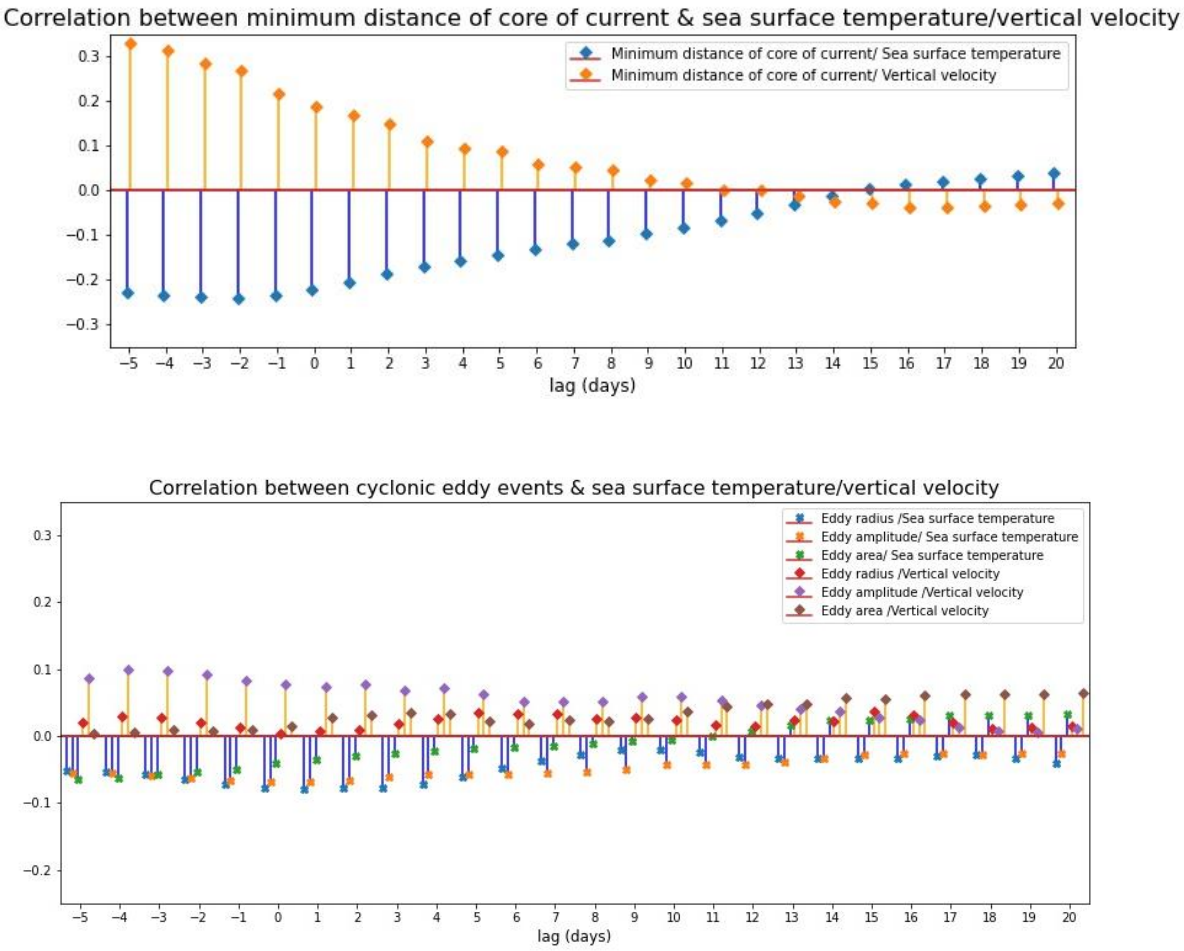

Figure 6.14: 1st row: Correlation between minimum distance of current's core and sea surface temperature (blue line)/vertical velocity (orange line). 2nd row: Correlation between eddy radius and sea surface temperature (blue dot on blue line)/vertical velocity (red dot on orange line), correlation between eddy amplitude and sea surface temperature (orange dot on blue line)/vertical velocity (purple dot on orange line), correlation between eddy area and sea surface temperature (green dot on blue line)/vertical velocity (brown dot on orange line).

As we explored the correlation plots between these variables and the upwelling events, this indicated the potential presence of meander induced upwelling. As the current's core was more distant, it showed a peak correlation of 0.3 with vertical velocity on day -5, and a negative correlation of -0.25 on day -2 with sea surface temperature. All the eddy variables also generated a positive correlation with vertical velocity and a negative correlation with sea surface temperature. The eddy amplitude had a correlation of 0.1 with vertical velocity on day -4 and -3 and the eddy radius also showed a negative correlation of 0.1 with sea surface temperature on day 1 and 2. While these correlation plots seemed to agree with the hypothesis of meander induced upwelling, similar to the other correlation plots, it was likely that seasonal influence was playing a role since winter was characterized by low sea surface temperature and weakening of the Agulhas Current.

6.5E Composites

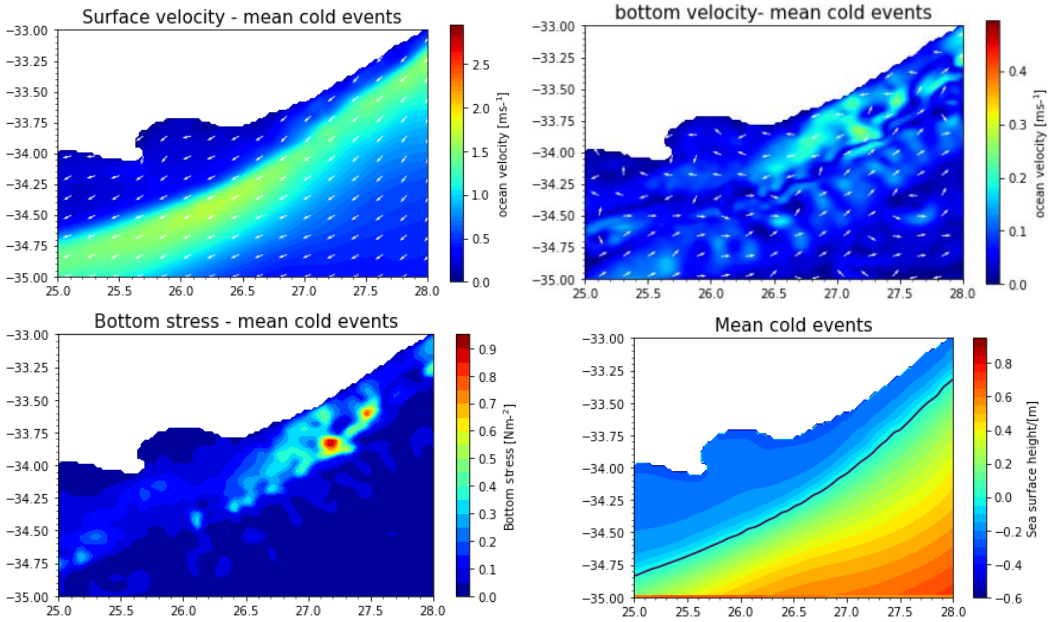

Figure 6.15: Average conditions during 56 selected upwelling events. 1st row (from left to right): sea surface velocity and bottom velocity, 2nd row (from left to right): bottom stress and sea surface height and detection of current's core and cyclonic eddies,

By focusing exclusively on the occurrences of 56 strong cold water events identified from sea surface temperature residuals, we calculated the mean state for various oceanographic parameters. These parameters included sea surface height, the position of the current's core, the detection of eddies, surface and bottom ocean velocities, and bottom stress. The core of the current consistently followed the shoreline without exhibiting any noticeable meandering activity. Sea surface height measurements confirmed the pronounced presence of the Agulhas Current. In the upwelling zone, surface ocean velocities ranged from 0.5 ms^{-1} to 1 ms^{-1}, indicating a negative geostrophic velocity and flowed from the northeast. Along the current itself, ocean velocities varied from 1.5 ms^{-1} to 2 ms^{-1}. Bottom ocean velocities were around 0.5 ms^{-1}, while bottom stress was significantly higher within the upwelling region, peaking at 0.7 N/m^2.

It was worth noting that the correlation plots demonstrated that, on average, meanders were associated with upwelling events rather than the mere presence of a strong current or coastal trapped waves. However, when we examined the average conditions during selected strong upwelling events, we observed less influence from meander events. This could be attributed to the fact that these correlation plots considered seasonal effects. During the winter season, there was typically a decrease in temperature, a weaker Agulhas Current and a slight increase in geostrophic velocity. transport. Excluding meander events from the analysis did not necessarily imply that other oceanographic forcing mechanisms were solely responsible for these upwelling events. Instead, it suggested a

substantial influence from atmospheric forcing mechanisms. This was further supported by the absence of upwelling-favorable winds during the winter season, indicating that seasonal factors played no role in the correlation plots for these atmospheric fields compared to the oceanographic fields.

6.5F Case study of selected upwelling events.

After computing the mean state of the 56 upwelling events, we investigated the various oceanographic variables for the 4 chosen case studies from chapter 4. In chapter 5, we had previously found that the case study from 22nd February 1999, 27th April 1999 and 8th March 2010 displayed a strong atmospheric influence on the upwelling. In the next section, we explored whether the current, the cyclonic eddies or the coastal trapped waves also had an influence on these upwelling events.

Case study 1: Presence of Agulhas Current

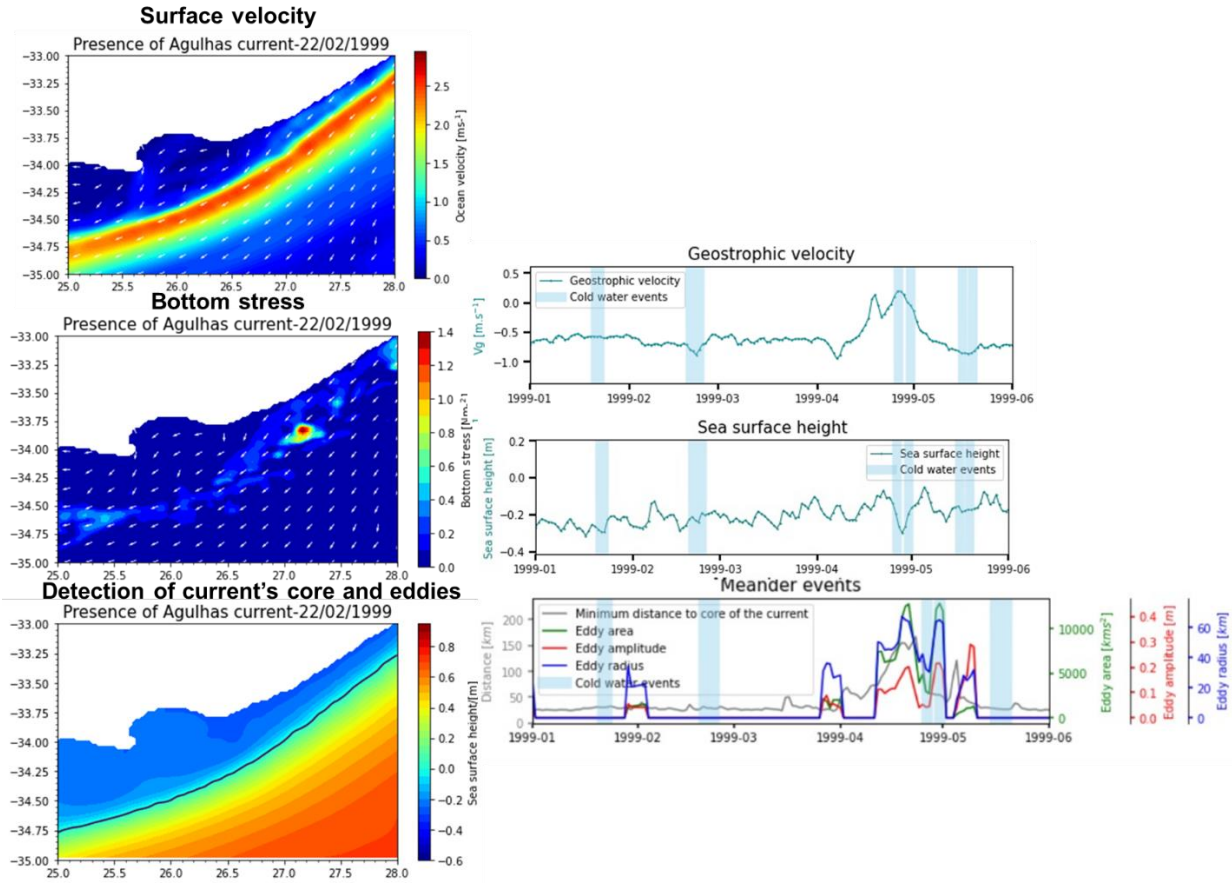

Figure 6.16: (Left side) 1st row: ocean velocity on the 22nd February 1999, 2nd row: current vectors overlaid on bottom stress on the 22nd February 1999, 3rd row: Detected current's core and cyclonic eddies overlaid onto sea surface height on the 22nd February 1999. (Right side) 1st row: geostrophic velocity plotted from January to May 1999. 2nd row: sea surface height plotted from January to May 1999. 3rd row: minimum distance between upwelling and current's core (black line)eddy area (green

line), eddy amplitude (red line) and eddy radius (blue line) plotted from January to May 1999. Detected cold events from upwelling indices were highlighted as light blue along the timeline.

We found that on the 22nd February 1999, the Agulhas Current's speed was relatively stronger with a speed of 2.5 m/s and a drop in geostrophic velocity in the Port Alfred upwelling zone. This decrease made sense as when the current flowed from a northeast to southwest direction, the geostrophic velocity would also decrease in the upwelling zone, hence resulting to almost -1 m/s on that date. As the current velocity was also strong, this also showed a more pronounced increase ($1.4N/m^2$) in the bottom stress. The negative change in geostrophic velocity and the increase in the bottom stress certainly proved that the Agulhas Current was very strong during this upwelling event. We also detected the position of the core of the current, which showed a smooth flow. As we applied the eddy tracker algorithm, no presence of cyclonic eddy was detected and there was no big change recorded in the sea surface height from the model outputs. Based on these two algorithms and the other oceanographic fields, we could clearly say that it reinforced the hypothesis of Ekman veering in the bottom boundary layer whereby an increase in the current strength was strongly influencing this upwelling. Hence in this case, this upwelling was induced by a combination of two forcing mechanisms: the presence of strong north easterly winds and an increase of the current's strength.

Case study 2: Presence of meander

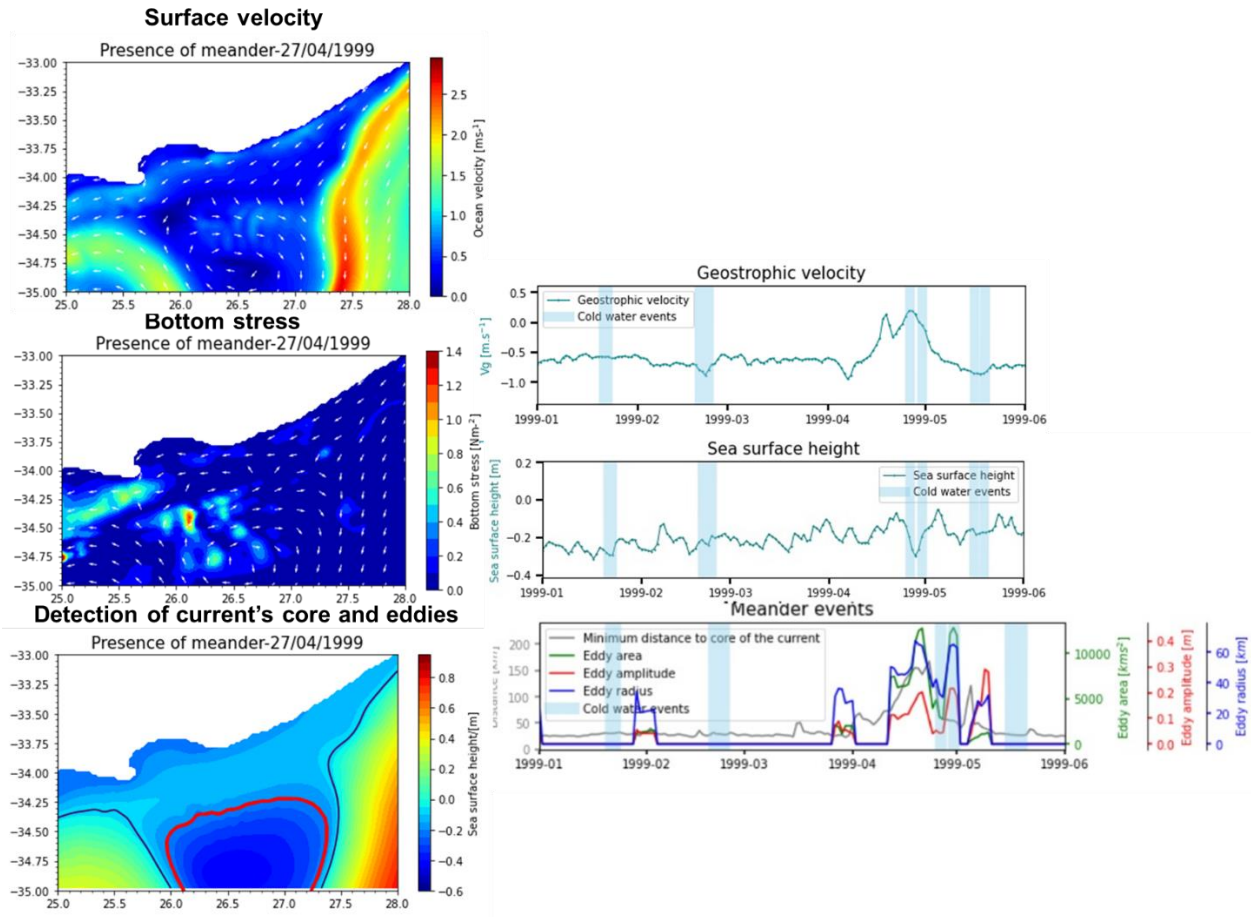

Figure 6.17: (Left side) 1st row: ocean velocity on the 27th April 1999, 2nd row: current vectors overlaid on bottom stress on the 27th April 1999, 3rd row: Detected current's core and cyclonic eddies overlaid onto sea surface height on the 27th April 1999. (Right side) 1st row: geostrophic velocity plotted from January to May 1999. 2nd row: sea surface height plotted from January to May 1999. 3rd row: minimum distance between upwelling and current's core (black line)eddy area (green line), eddy amplitude (red line) and eddy radius (blue line) plotted from January to May 1999. Detected cold events from upwelling indices were highlighted as light blue along the timeline.

We had also identified that in chapter 5 the upwelling on the 27th April 1999 was highly influenced by the wind as well. Here, we tested whether this upwelling was also influenced by the meander. The presence of the cyclonic eddy was very clear from the measurements of the horizontal velocity. The core of the current moved further offshore beyond -35°S. In the Port Alfred upwelling zone, the geostrophic velocity was seen to go from -0.5 to 0.1m/s in the upwelling region. To further ensure that there were no interactions of the current in the bottom boundary layer, the model outputs showed that the bottom stress was too low (0.1 N/m^2) during this event. The direction of the current at the bottom could not indicate any onshore Ekman transport. This upwelling was certainly not influenced from the bottom boundary layer.

The position of the core of the current was detected and was seen to strongly meander. The eddy tracker algorithm applied to the model output detected a clear outline of the eddy along with the inshore edge of the current. There was a relatively high decrease in the sea surface height, which was expected during the clockwise rotation of an eddy. The LACCE algorithm showed that the core of the current was 150 km away from the upwelling zone and this also correlated with the outputs from the eddy tracker algorithm, with an eddy radius of 60km, an eddy amplitude of 0.2 m and an eddy area of 12000 km^2. Relying on these 2 robust methods of tracking meander events, this reinforced the hypothesis that this upwelling event was indeed influenced by the meander. Therefore, this upwelling was triggered by the combined influence of 2 driving factors: the presence of north easterly winds and a cyclonic eddy.

Case study 3: Presence of northeasterly winds

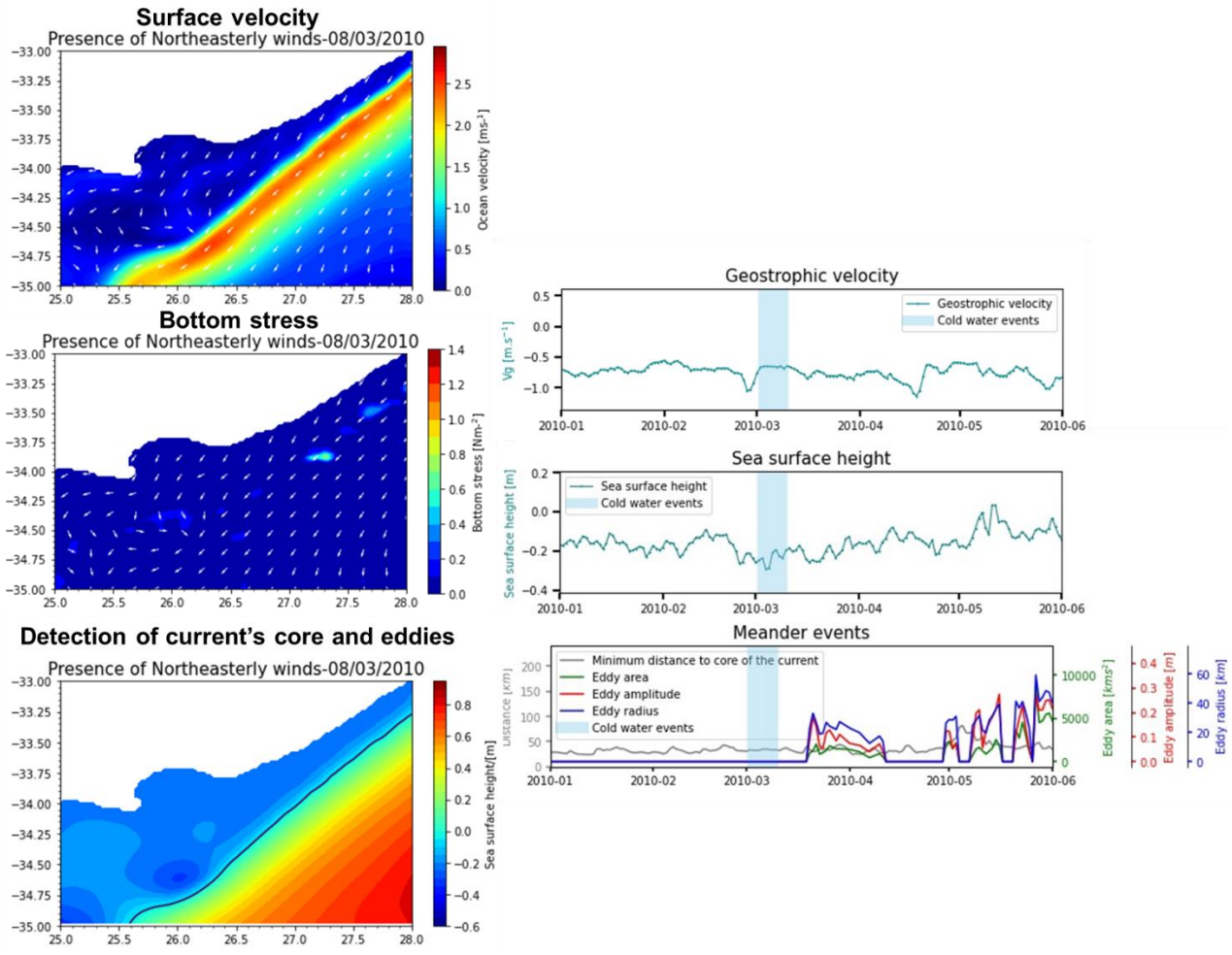

Figure 6.18: (Left side) 1st row: ocean velocity on the 8th March 2010, 2nd row: current vectors overlaid on bottom stress on the 8th March 2010, 3rd row: Detected current's core and cyclonic eddies overlaid onto sea surface height on the 8th March 2010. (Right side) 1st row: geostrophic velocity plotted from January to May 2010. 2nd row: sea surface height plotted from January to May 2010. 3rd row: minimum distance between upwelling and current's core (black line)eddy area (green line), eddy

amplitude (red line) and eddy radius (blue line) plotted from January to May 2010. Detected cold events from upwelling indices were highlighted as light blue along the timeline.

The case study of the 8th March 2010 was shown to have a strong influence of upwelling favorable winds in chapter 5 as well as in the study of Goschen et al (2015). Here we also assessed the influence of the oceanographic forcing mechanisms on this upwelling. It was interesting to point out that the horizontal velocity of the current was about 2 m/s relatively lower than the one on the 22nd February 1999, hence the current strength was less strong. On further inspection, there was a sudden decrease in the geostrophic velocity around the 28th of February. The presence of the core of the current was very close to the upwelling zone but did meander very slightly as it passed by Algoa Bay. The eddy tracker algorithm only detected a minor possible eddy but did not record any values for the eddy area, eddy amplitude and the eddy radius. It was unlikely that the current would induce upwelling from bottom Ekman veering as the bottom stress was very low. Hence we were unable to detect the oceanographic influence and this upwelling event was solely influenced by the presence of northeasterly winds.

Case study 4: Presence of coastal trapped waves

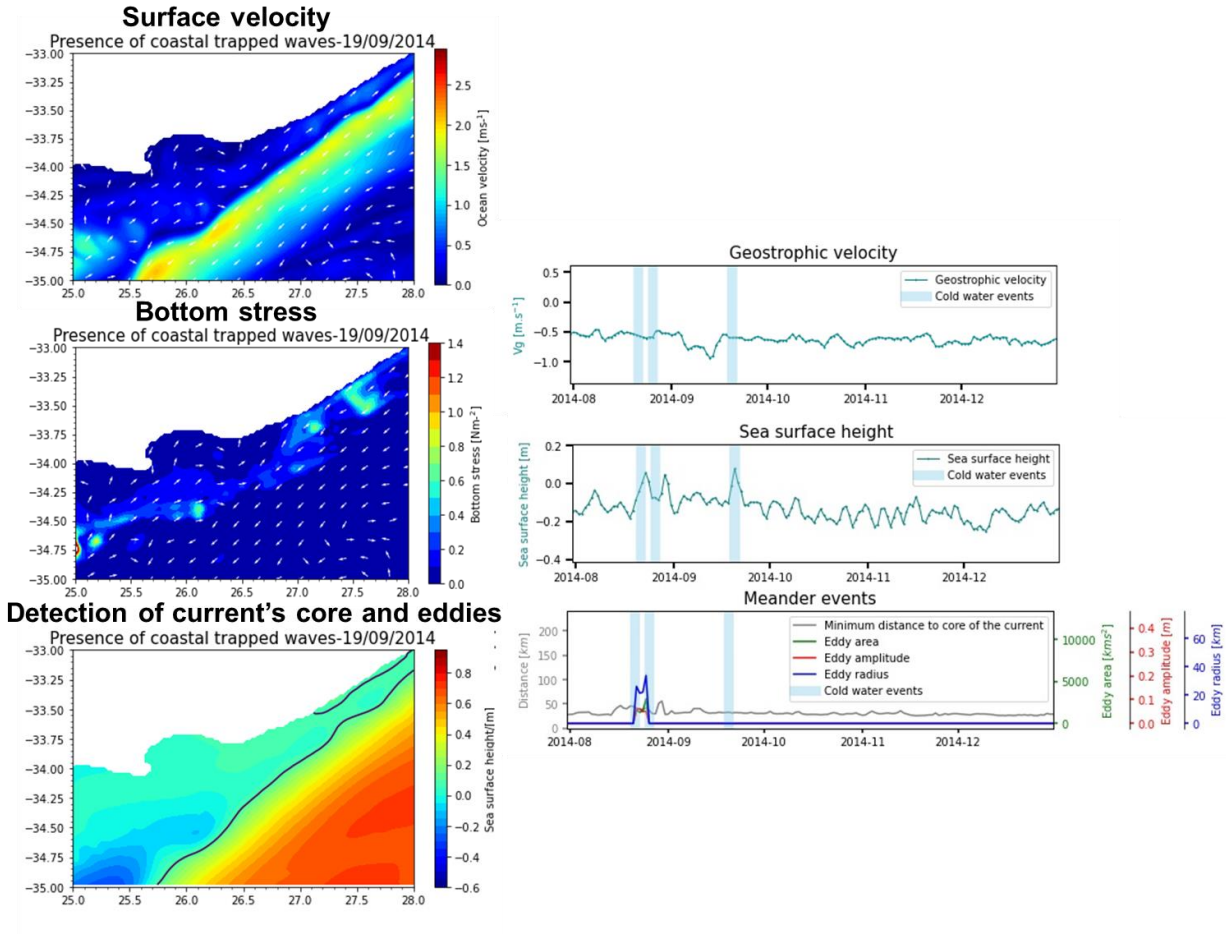

Figure 6.19: (Left side) 1st row: ocean velocity on the 19th September 2014, 2nd row: current vectors overlaid on bottom stress on the 19th September 2014, 3rd row: Detected current's core and cyclonic

eddies overlaid onto sea surface height on the 19th September 2014. (Right side) 1st row: geostrophic velocity plotted from August to December 2014. 2nd row: sea surface height plotted from August to December 2014. 3rd row: minimum distance between upwelling and current's core (black line)eddy area (green line), eddy amplitude (red line) and eddy radius (blue line) plotted from August to December 2014. Detected cold events from upwelling indices were highlighted as light blue along the timeline.

Previously in chapter 5, we noted that there was no presence of upwelling favourable winds on that day. Bailey et al (2022) had also reported a strong presence of coastal trapped waves on that day. In this section, we assessed if there was any oceanographic influence on this upwelling. The current did not display any sign of increasing strength through its bottom stress however we noted a small decrease of geostrophic velocity a few days before the event where it reached about -0.8 m/s. The current direction near the coast was flowing against the direction of the current indicating potential offshore Ekman transport due to the current. A strong increase of sea surface height, peaking till 0.1m was recorded on the day. Bailey et al (2022)'s higher resolution model also recorded an increase in sea surface height of 0.55m. The LACCE algorithm also detected a higher sea surface height closer to the shore alongside the core of the current. It was high likely that this upwelling event occurred due to the propagation of these coastal trapped waves along the coast.

6.6 Summary and discussion

This study investigated the mean state, seasonal, monthly variations and correlations of oceanographic parameters in the Agulhas region. The vertical pumping from the generalized Ekman pumping equation was quite similar to the model derived vertical velocity. By breaking down the terms of this equation, we found that the non linear term of the equation, i.e the advection of momentum was a major contributor to upwelling whereby the detachment of the current could induce upwelling through divergence. The viscous flux term also showed that friction was a minor contributor of the Port Alfred upwelling.

Sea surface height exhibited lower values in both winter and summer, with a slight peak in winter. The Agulhas Current's strong presence on the shelf, especially in summer, suggested increased upwelling potential due to the narrowing of the inertial jet, potential vorticity conservation and onshore bottom Ekman transport. Correlations indicated that upwelling events were associated with decreased sea surface height, with patterns suggesting cyclonic eddy-induced upwelling. Surface velocity showed seasonal variations, with higher values in summer. Geostrophic velocity correlated positively with vertical velocity and negatively with sea surface temperature, persisting for an extended period, possibly indicating a Natal pulse. The bottom Ekman transport displayed negative correlations with sea surface temperature and negative correlations with vertical velocity, reinforcing the hypothesis of bottom Ekman veering from the current.

To ensure we captured the presence of the current, we relied on a current's core tracker algorithm to compute the minimum distance between the current and the upwelling. We also generated the eddy area, eddy amplitude and eddy radius from the PY eddy tracker algorithm. We identified 1.9 large meander events per year from the LACCE's algorithm, 2.2 large meander events from the eddy amplitude, 1.5 large meander events from the eddy area and 1.3 large meander events from the eddy radius. This was quite similar to previous studies conducted by Russo et al (2020) whereby they identified 1.8 large meanders per year.

While Lutjeharms (2006) hypothesized that Natal pulses were triggering upwelling activity, the rate of occurrence of Natal pulses from this study was fairly low (1.3 to 2.2 large meander events per year), and the occurrence of Natal pulses only would not satisfy the explanation of the entire upwelling activity. Hence a separate investigation of smaller cyclonic eddies could also be done to determine the difference between the influence of large and small meander events on this upwelling.

We explored the correlation between the variables from these algorithms and sea surface temperature/vertical velocity. The correlation plots appeared to support the notion of meander-induced upwelling, similar to the other correlation plots. Upon examining the average conditions during strong upwelling events, we noted that the influence of meander events was less pronounced. This was likely due to the consideration of seasonal effects, particularly during the winter season, marked by decreased temperature, a weaker Agulhas Current, a slight increase in geostrophic velocity, and a minor decrease in bottom Ekman transport. Excluding meander events from the analysis did not imply that other oceanographic forcing mechanisms were the sole drivers of these upwelling events. Instead, it suggested a significant role for atmospheric forcing mechanisms, supported by the absence of upwelling-favorable winds during the winter season, highlighting the importance of seasonal factors in these correlations, particularly for atmospheric fields compared to oceanographic ones.

We explored the 4 case studies individually whereby we noted that the current was a strong contributor of the upwelling on the 22nd February 1999. As for the 27th April 1999, a strong meander event was found to be inducing upwelling. The winds were also already identified as an upwelling driver. We could not account any oceanographic influence during the upwelling event of 8th March 2010 and only northeasterly winds could explain this upwelling. On the 19th September 2014, a strong coastal trapped wave was detected through the sea surface height and the LACCE algorithm and this upwelling was most likely triggered by the propagation of coastal trapped waves.

6.7 Highlights

As an overall, this study was conducted to test the hypothesis of the influence of oceanographic influence on the Port Alfred upwelling and 3 new findings from this investigation, highlighting its unique contributions, include:

1) During the mean state, the different terms of the generalized Ekman pumping equation were computed and the advection of momentum proved to be a dominating upwelling driver, recording a vertical velocity of 4.22 m/day in the Port Alfred upwelling region while the viscous flux term also contributed partially to 0.5 m/day of vertical velocity in the Port Alfred region.
2) Focusing on the Port Alfred region in the CROCO simulations, the LACCE current tracker algorithm identified an average of 1.9 large meander events annually, while the Py eddy tracker algorithm located 2.2 large meander events based on eddy amplitude, 1.5 based on eddy area, and 1.3 based on eddy radius.
3) Assessing the sea surface height, ocean velocity, bottom Ekman transport, detection of the current and eddies in the Port Alfred upwelling region through the lens of different temporal scales (seasonal, monthly, mean state of all the upwelling events) reveals that the Agulhas Current is the main upwelling driver during the mean state. However, in individual cases, the upwelling could also be triggered by cyclonic eddies and coastal trapped waves.

Chapter 7: Driving mechanisms of Port Alfred upwelling: A statistical approach.

7.0 Introduction

After exploring the impact of atmospheric and oceanographic forcing mechanisms on the Port Alfred upwelling, we found that during the mean state and the seasonal state, the Agulhas Current was a dominant upwelling driver, while during individual case studies, the upwelling driver would vary from different forcing mechanisms (upwelling favorable winds, vertical mixing, the Agulhas Current, the cyclonic eddies and coastal trapped waves). Each forcing mechanism, or sometimes a combination of them was linked to the upwelling. However, we did not compare which forcing mechanism was the most important upwelling driver in the Port Alfred.

In this chapter we addressed the fourth research question:

What is the most dominating forcing mechanism of the Port Alfred upwelling?

To determine the most dominant variable causing a cold sea surface temperature or an increase in vertical velocity in the presence of influencing factors such as wind stress, wind stress curl, frictional velocity, sea surface height, minimum distance to current, eddy amplitude, bottom Ekman transport, and geostrophic velocity, various statistical methods for variable selection and causality analysis could be explored.

7.1 Statistical methods to compare variables

For instance, we could conduct a correlation analysis whereby we would measure the strength and direction of the linear relationship between two variables (Yi et al, 2018). It would involve calculations of Pearson correlation coefficients between cold sea surface temperature and each potential influencing variable. Higher absolute correlation values would indicate a stronger association. However, a correlation would not be enough for any strong deductions to be made. It would not always imply causation and this type of analysis would not consider other variables' influence.

A combined Empirical Orthogonal Function analysis could also be conducted whereby it would reduce the dimensionality of the dataset while capturing the most important patterns of variability. This approach would allow us to examine the interrelation among all the variables such as wind stress, geostrophic velocity and sea surface height by breaking down their correlation matrix into eigenvectors (Kutzbach, 1967). These eigenvectors, termed EOFs, would represent intertwined modes of variation where two or more driving variables would collaborate to induce a decrease in sea surface temperature or an increase in vertical velocity. In Port Alfred, Leber et al (2017) adopted this

approach by using only cold water events and presented two modes of the combined EOF analysis of sea surface temperature anomalies and 4 forcing mechanisms (alongshore wind speed, wind stress curl, sea surface height and geostrophic velocity) to assess the main driver of the upwelling.
Another method would involve a multiple linear regression to examine how multiple independent variables collectively predicted a dependent variable. A regression model would be created with cold sea surface temperature/positive vertical velocity as the dependent variable and all potential influencing variables as independent variables (Feng et al, 2020). The significance of the coefficients and their signs would then be assessed to determine which variables contributed significantly to the model's prediction of cold water/positive vertical velocity. Zhang and McPhaden (2006) have previously used multiple linear regression to examine the relationship between wind stress variations and interannual sea surface temperature anomalies in the eastern equatorial Pacific.

Other approaches also could include a stepwise regression, an automated variable selection process, used to iteratively add or remove variables based on their contribution to explaining the variance in the dependent variable (cold SST) or a partial correlation analysis could be used to assess the relationship between two variables while controlling for the effects of other variables.

7.2 Aims and objectives

In this chapter, we relied on a combined empirical orthogonal function analysis to compare all the forcing mechanisms in order to find out which forcing mechanism was the largest contributor in this upwelling.

7.3 Materials and methods

Firstly we computed the correlation coefficient between every forcing variable (wind stress, wind stress curl, frictional velocity, sea surface height, geostrophic velocity, bottom stress, minimum distance between current's core and Port Alfred, and eddy amplitude) and sea surface temperature/vertical velocity and compared the values. Secondly we computed the correlation matrix to understand the co-variabilities of the 8 forcing variables. This allowed us to verify any interdependence between any of the forcing variables.
We then proceeded to conduct a combined Empirical Orthogonal function analysis in 2 different ways. To ensure we were capturing the forcing mechanisms for upwelling, we chose to select only the upwelling events from 1993 to 2014. The combined EOF was conducted twice, firstly through cold water events identified from sea surface temperature's residuals < -1°C and secondly through upward velocity events identified by vertical velocity's residuals at 100m > 0.15 cm/s (see chapter 4). Every field was detrended and deseasonalized through a classical decomposition and we used only the residuals. We then decomposed the correlation matrix into eigenvectors and eigenvalues. This process involves a mathematical operation known as the eigenvalue decomposition. Each eigenvector represents a different mode of variability, or a different way that the variables are related to each other

and the eigenvalues represent the amount of variance captured by each mode. The first few eigenvectors generally explain the most variability in the data, while the later eigenvectors would explain less.

7.4 Results

7.4A correlation analysis

	Sea surface temperature	Vertical velocity
Wind stress	0,25	-0,21
Wind stress curl	0,2	-0,21
Frictional velocity	-0,24	0,08
Sea surface height	0,21	-0,22
Geostrophic velocity	0,1	0,25
Bottom Ekman transport	-0,12	-0,08
Minimum distance from PA to current	-0,22	0,27
Eddy amplitude	-0,07	0,08
Eddy area	-0,04	0,01
Eddy radius	-0,08	0

Table 7.1: Correlation between forcing mechanisms and sea surface temperature/vertical velocity

In chapter 5 and 6, for each variable, we had previously conducted a decomposition of their respective daily time series, retaining only the residuals which represented the unexplained variability beyond their long term means. Using these residuals at a daily scale from 1993 to 2014, we computed the correlation coefficient between the sea surface temperature/vertical velocity and each variable. Here it made sense that each positive/negative correlation to sea surface temperature reflected as a negative/positive correlation vertical velocity. Wind stress had the strongest positive correlation with sea surface temperature while vertical velocity had the strongest positive correlation with minimum distance from Port Alfred to the current. Leber et al (2017) also explored the correlation between sea surface temperature anomalies and other variables such as wind speed, wind stress curl, geostrophic velocity and sea surface height anomalies in the Port Alfred region. They also found that sea surface temperature had a positive correlation with alongshore wind speed and sea surface height and a negative correlation with wind stress curl and geostrophic velocity (Leber et al, 2017).

7.4B Correlation within each other

	Wind stress curl	Frictional velocity	Sea surface height	Minimum distance to core of current	Eddy amplitude	Geostrophic velocity	Bottom Ekman transport
Alongshore windstress	0,90	0,45	0,52	-0,16	-0,22	-0,34	0,23
Windstress curl		0,36	0,51	-0,15	-0,13	-0,37	0,33
Frictional velocity			0,23	-0,09	-0,15	-0,17	-0,12
Sea surface height				-0,13	-0,11	-0,39	0,23
Minimum distance to core of current					0,20	0,10	-0,14
Eddy amplitude						0,13	-0,10
Geostrophic velocity							-0,45

Table 7.2 : Correlation matrix for the 8 forcing variables: Alongshore windstress, windstress curl, frictional velocity, sea surface height, minimum distance to core of the current, eddy amplitude, geostrophic velocity and bottom Ekman transport.

We also computed the correlation coefficient between the different variables. Describing cold events in terms of their underlying forcing mechanisms presented a challenge due to the interdependence among the different oceanographic and atmospheric variables. For instance, we found that sea surface height and geostrophic velocity had a negative correlation of -0.39. Leber et al (2017) also reported a negative correlation of -0.77 between these two variables. This correlation would be explained in 2 ways. Firstly, during the passage of a cyclonic eddy, the eddy would initiate an inshore countercurrent whereby the geostrophic velocity would increase and the sea surface height would decrease. Secondly, based on the hypothesis of increased current strength, as the geostrophic velocity would decrease, the sea surface height would increase due to the intrusion of the current on the shelf. As for the atmospheric forcing variables, wind stress and wind stress curl showed a strong positive correlation of 0.9 as a negative wind stress would induce offshore Ekman transport while a negative wind stress curl would trigger divergence.

7.4C PCA modes of variance

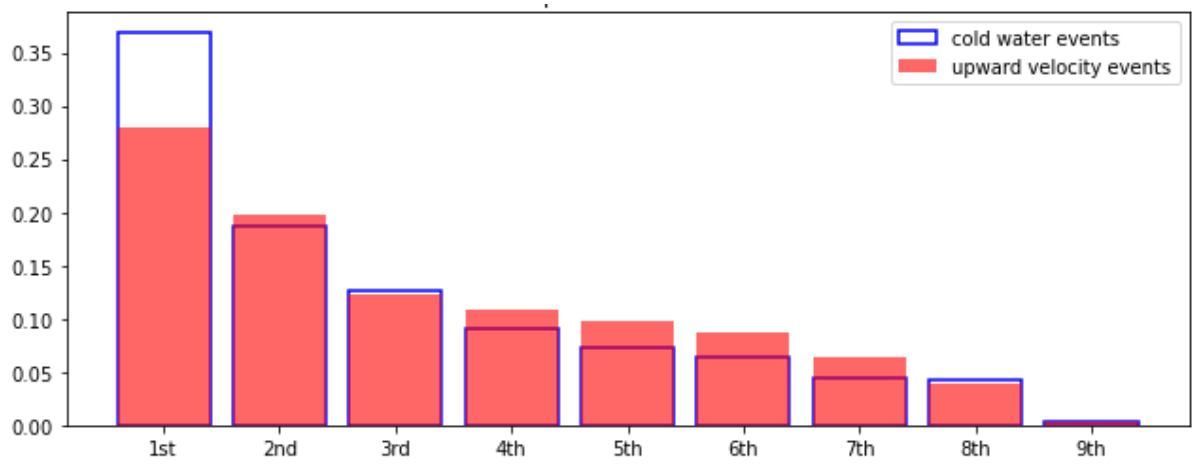

Figure 7.1: Distribution of variance explained by different EOF modes of cold water events (blue bar) and upward velocity events (red bar)

The bar chart in Figure 7.1 illustrates the distribution of variance explained by different PCA modes in figure . Both the cold water events and upward velocity events exhibited similar distribution except for the first mode whereby the cold water events could explain 36.9% while the upward velocity only explained 27.9% of the total variance. The first mode stood out as the most significant for the cold water events. Following closely is the second mode, which accounts for approximately 18.8% of the variance for the cold water events and 19.8% for the positive vertical velocity events, indicating substantial importance as well. The third mode contributes around 10%, still significant but less dominant. As we progress through the modes, the variance explained gradually decreases, with the eighth mode contributing a minimal 0.05% to the overall variance. This demonstrates a clear diminishing trend in the importance of each successive mode in explaining the dataset's variability.

7.4D 1st and 2nd EOF mode

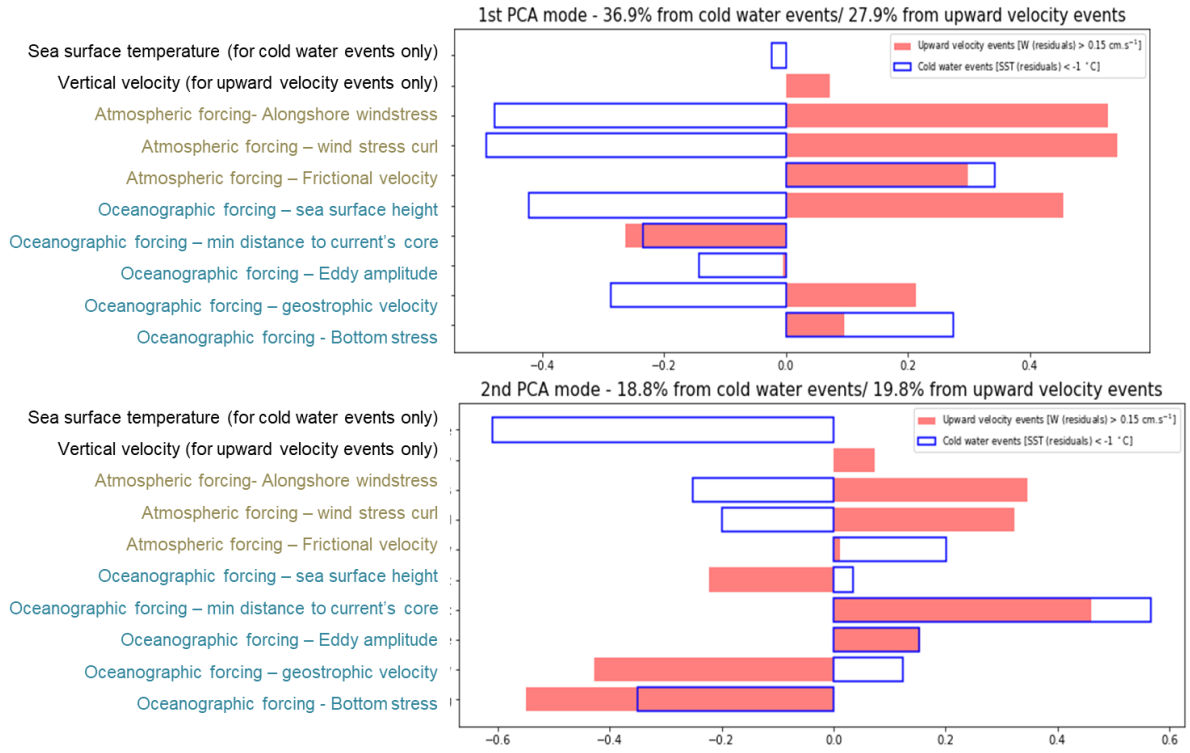

Figure 7.2: Two panels showing the amplitude of the eigenvectors for the first two modes of a combined EOF analysis of (1) cold water events [sea surface temperature and its forcing variables alongshore windstress, windstress curl, frictional velocity, sea surface height, minimum distance to core of the current, eddy amplitude, geostrophic velocity and bottom stress (all in blue bars)] and (2) upward velocity events [vertical velocity and its forcing variables alongshore windstress, windstress curl, frictional velocity, sea surface height, minimum distance to core of the current, eddy amplitude, geostrophic velocity and bottom stress (all in red bars)]. For cold water events, the negative/positive

phases correspond to stronger/weaker cold events. For upward velocity events, the positive/negative phases correspond to stronger/weaker upward velocity events.

The calculated amplitudes of the eigenvectors for the first two modes are plotted to visually represent the contribution of each forcing mechanism to the variability in cold water events/upward velocity events in figure 7.2. The first two EOF modes accounted for 55.7% of the variability during the cold events and 47.7% during the upward velocity events. For the cold water events, the residuals for sea surface temperature for each mode are defined as residuals less than -1°C, and hence the negative phases for each mode represented stronger events and positive phases represented the weaker events amongst the cold events. As for the upward velocity events, we selected the vertical velocity's residuals where they were higher than 0.15 cm/s. In this case, the positive phases for each EOF mode represent stronger upward velocity events and the negative phases indicated the weaker upward velocity events.

Cold water events

The negative phase of EOF1 for the cold water events recorded an amplitude of -0.05 for sea surface temperature. It was characterized by negative eigenvectors of wind stress, wind stress curl, sea surface height, minimum distance to core of the current, eddy amplitude and geostrophic velocity. Among these forcing variables, the negative eigenvectors of wind stress, windstress curl and sea surface height were more dominant compared to the other forcing variables. For the positive phase of EOF1, only frictional velocity and bottom stress were linked to the weaker cold water events. Hence, this implied that for 36.9% of the cold water events, changes in the wind stress, wind stress curl, sea surface height, minimum distance to core of the current, eddy amplitude and geostrophic velocity could explain the stronger upwelling events, and only changes in frictional velocity and bottom stress could explain the weaker upwelling events. As for the second EOF mode, it recorded an amplitude of -0.6 for sea surface temperature. It also accounted for 18.8% of the cold water events, alongshore wind stress, windstress curl and bottom stress were the only forcing variables which contributed to a stronger cold water event. The remaining forcing variables contributed to weaker cold water events. These two modes of EOF can also be compared to similar findings from Leber et al (2017) in figure 7.3 whereby they reported that their 1st EOF mode accounted for 43% while their 2nd EOF mode accounted for 31%.

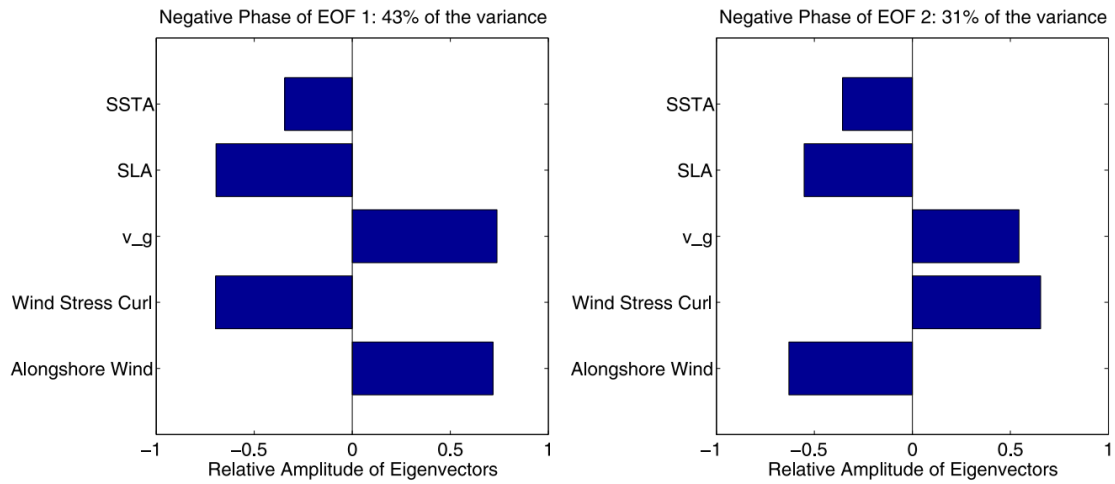

Figure 7.3: Findings from Leber et al (2017) showing the amplitude of the eigenvectors for the first two modes of a combined EOF analysis of cold water events [sea surface temperature anomalies and its forcing variables sea level anomaly, geostrophic velocity, wind stress curl and alongshore wind]

Upward velocity events

For the 1st EOF mode, accounting for 27.9% of upward velocity events, stronger upwelling events were primarily linked to its positive eigenvectors: alongshore wind stress, wind stress curl, frictional velocity, sea surface height, geostrophic velocity and bottom stress, while changes in the remaining forcing variables accounted for weaker upwelling events. And for 19.8% of the upward velocity events (2nd EOF mode), changes in all the forcing variables except for sea surface height, geostrophic velocity and bottom stress could explain the stronger upwelling events.

7.4E EOF time series

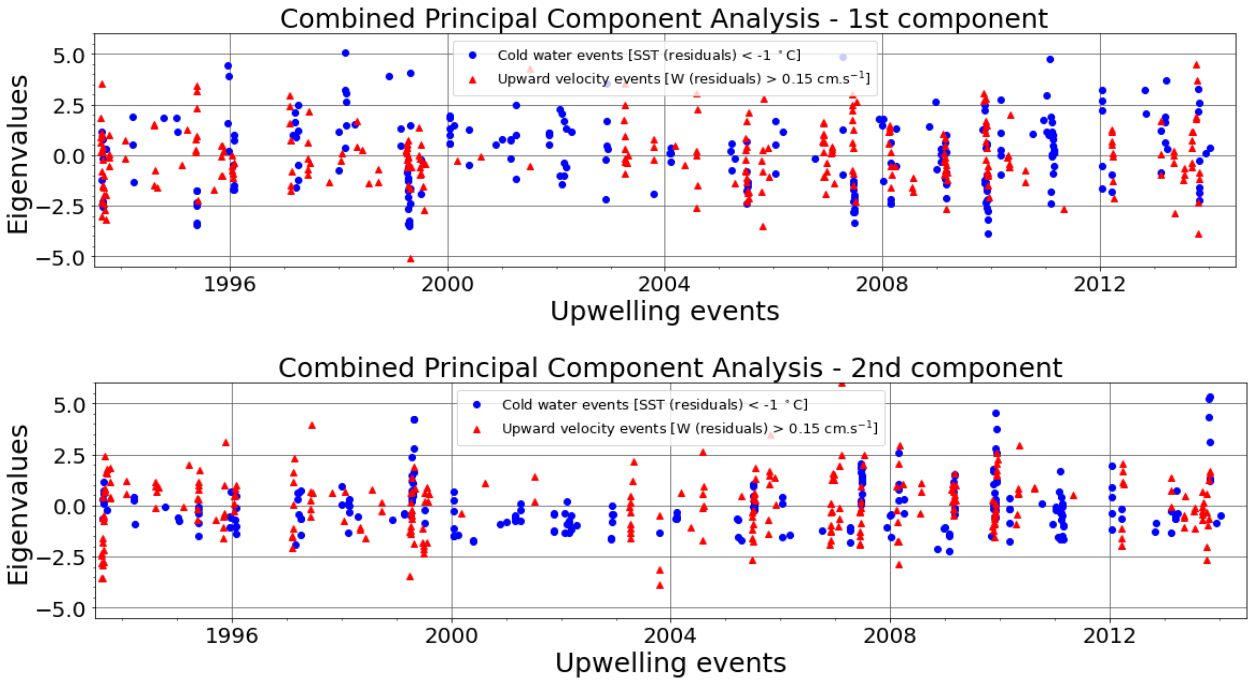

Figure 7.4: The eigenvalues for the cold water events (blue) and upward velocity events (red) plotted from 1993 to 2014 for the EOF1 and EOF2.

The time series of their eigen values for cold water events and upward velocity events are plotted in Figure 7.4. The eigenvalues corresponding to cold water events (depicted in blue) and upward velocity events (depicted in red) are depicted in a time series spanning from 1993 to 2014 for both EOF1 and EOF2. In this time series, values below zero for cold water/upward velocity events are indicative of stronger/weaker upwelling events, while values above zero signify weaker/stronger upwelling events. It is evident from the time series that, in numerous instances, stronger cold water events (represented by negative eigenvalues in blue) and stronger upward velocity events (indicated by positive eigenvalues in red) coincided across both EOF modes. Similarly it can also be observed that in many cases, the weaker cold water events (negative eigenvalues in blue) and the weaker upward velocity events (positive eigenvalues in red) occurred at the same time too.

It is necessary to highlight that some forcing variables could indicate different upwelling mechanisms. For instance, if the negative phase of EOF1 for cold water events could be explained by a decrease in sea surface height, this would imply that these stronger cold water events were occurring due to the presence of a cyclonic eddy. However, if it was explained by an increase in sea surface height, then it would have resulted in upwelling due to the presence of the current or coastal trapped waves. Hence an analysis of the mean residuals of these forcing variables and the average conditions of the positive and negative modes of the EOF1 and EOF 2 would provide clarity on these upwelling driving mechanisms.

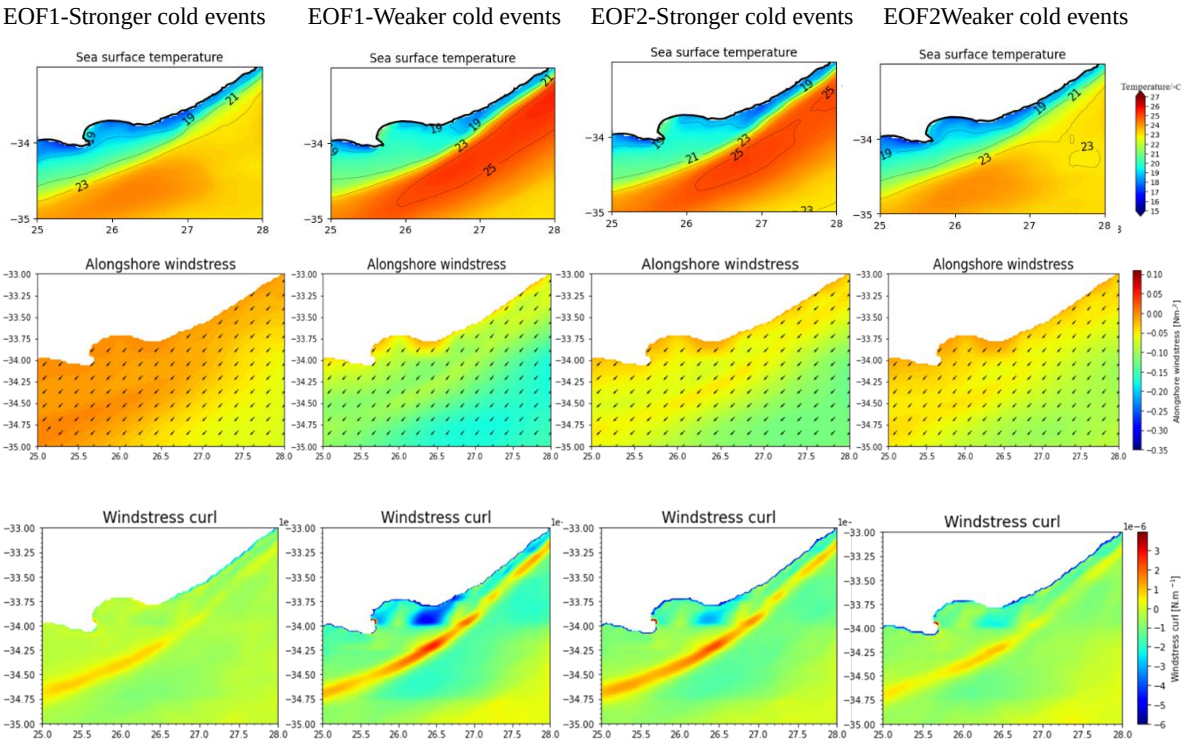

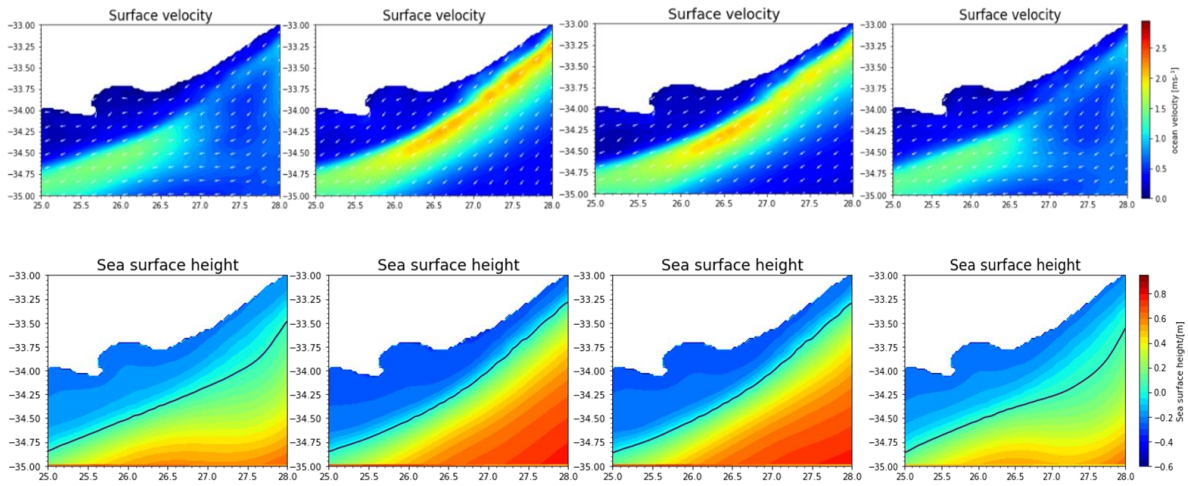

Figure 7.5 illustrates the patterns associated with the two EOFs (1st row: sea surface temperature, 2nd row: alongshore wind stress, 3rd row: wind stress curl, 4th row: surface velocity and 5th row: sea surface height)

Figure 7.5 shows the composites for stronger and weaker cold water events for EOF 1 and EOF 2 were calculated from the 56 cold water events. This was done by locating all the events for the negative/positive eigenvalues along the time series in figure and by computing the average conditions of sea surface temperature, alongshore wind stress, wind stress curl, ocean velocity, sea surface height and position of the core the Agulhas Current for the stronger/weaker cold water events of the 2 EOF modes.

1st EOF mode of stronger cold water events – combination of northeasterlies and meanders

We found a clear link between stronger cold water events from EOF 1 to a combination of northeasterlies and the presence of meanders. For the first mode of EOF, the dominant forcing variables which mostly explained the stronger cold water events from Figure 7.2 were: (1) wind stress curl (2) wind stress and (3) sea surface height. This was confirmed in Figure 7.5 with the presence of northeasterlies dominating geographically everywhere. The sea surface height along with the other variables such as the geostrophic velocity, minimum distance to core of current and eddy amplitude confirmed a slight presence of meander from the EOF1 stronger cold water events' mean in Figure 7.5 Compared to Leber et al (2017), their EOF1 stronger cold water events were also linked to upwelling favourable winds and presence of a meander.

1st EOF mode of weaker cold water events – Agulhas Current

As for weaker cold water events, it was likely that these events were driven by the Agulhas Current. Based from the positive eigenvectors of (1) frictional velocity and (2) bottom stress in Figure 7.2, vertical mixing and a strong current were found to be present. The increase in the current strength from Figure 7.5 also showed a clear presence of a strong current.

2nd EOF mode of stronger cold water events – combination of Agulhas Current and northeasterlies

For the second mode of EOF, the stronger cold water events were driven by a combination of the current and the northeasterlies. Figure 7.2 identified (1) bottom stress, (2) wind stress and (3) wind stress curl as the 3 most dominant forcing variables which could explain these events. The bottom stress showed a clear link of stronger cold water events to the strength of the current during their 2nd EOF mode. In Figure 7.5, we detected no meander and the surface horizontal speed identified a strong current during the stronger cold water events. Figure 7.5 also showed a stronger presence of northeasterlies through its negative wind stress and negative wind stress curl in the Port Alfred upwelling region. Compared to Leber et al (2017), their EOF2 stronger cold water events were also linked to upwelling favourable winds.

2nd EOF mode of weaker cold water events – meanders

As for the EOF 2 weaker cold water events, they were mainly driven by a meander event. The most dominant forcing mechanism was explained by its positive eigenvector of the minimum distance to the core of the current. Other variables showing a positive eigenvectors were also eddy amplitude, geostrophic velocity and sea surface height. As for the average of the composites for EOF 2 weaker cold water events in Figure 7.5, we also noted a weak presence of the current from the horizontal surface velocity. The current tracker algorithm detected the presence of a meander. Hence it was likely that these events were mainly driven by a meander event.

1st EOF mode of stronger upward velocity events – northeasterlies and meanders

The EOF 1 stronger upward velocity events were driven by a combination of upwelling favourable winds and meanders. The stronger upward velocity events associated with EOF 1 can be elucidated through its 3 most dominant forcing variables displaying positive eigenvectors: (1) wind stress curl (2) wind stress and (3) sea surface height. These 3 forcing variables were also identified as the dominant forcing variables for EOF1 stronger cold water events whereby they were linked to upwelling favourable winds and meanders.

1st EOF mode of weaker upward velocity events - meanders

The weaker upward velocity events were explained mostly by its 2 forcing variables displaying negative eigenvectors: (1) minimum distance to current's core and (2) eddy's amplitude and were possibly linked to a meander.

2nd EOF mode of upward velocity events

Regarding the 2nd EOF mode, the stronger upward velocity events were driven possibly by a combination of upwelling favourable winds and meanders while the weaker upward velocity events were driven by the Agulhas Current. In Figure 7.2, the stronger upward velocity events identified 1) minimum distance to the current's core 2) wind stress 3) wind stress curl and 4) eddy amplitude as

their most dominant positive eigenvectors while the EOF2 weaker upward velocity events identified 1) bottom stress 2) geostrophic velocity and 3) sea surface height as the most dominant negative eigenvectors.

7.5 Discussion

A correlation analysis between the forcing variables and sea surface temperature/vertical velocity is not enough to determine which upwelling drivers are more dominant and can possibly be influenced by seasons or other factors as it reflects an average of 2 decades of data. Conducting a combined EOF analysis is more suitable as we can focus on the upwelling events only and this method reduces the dimensions of all the variables and provides a deeper understanding of the magnitude of the upwelling drivers. In this study we used 8 forcing variables (measuring ocean and atmospheric properties not only from the surface but also from the bottom of the ocean) to ensure we were able to assess different upwelling drivers in Port Alfred: upwelling favorable winds, cyclonic eddies, Agulhas Current and coastal trapped waves.

We conducted 2 combined EOF analysis based from: 1) cold water events derived from residuals of sea surface temperature and 2) upward velocity events derived from vertical velocity. The first EOF mode observed for stronger cold water events suggests that both northeasterly winds and meanders contribute to these events. The main driver for the weaker cold water events seems to be the Agulhas Current. Looking at the 2nd EOF mode for stronger cold water events, it appears that both the Agulhas Current and northeasterly winds play a role. On the other hand, for weaker cold water events, meanders seem to be the key upwelling factor.

As for upward velocity events, a combination of northeasterly winds and meanders seems to be responsible for stronger upward velocity events. In contrast, for weaker upward velocity events, meanders are more dominant. In the 2nd EOF mode for stronger upward velocity events, both northeasterly winds and meanders seem to trigger upwelling. Finally, for weaker upward velocity events, the Agulhas Current appears to be the primary upwelling driver.

We ensured that it was a robust method as we conducted 2 combined EOF analysis (from 56 cold water events and 49 upward velocity events). Both seemed to be in agreement with each other as both identified surface divergence as the most dominant upwelling driver for stronger cold water and upward velocity events during their 1st mode of a combined EOF. Comparing our results to Leber et al (2017)'s study, we found that their first EOF mode for cold water events consisted of 43% of the variance compared to 37% in this study. Similarly, they had also identified surface divergence as a dominant forcing mechanism for stronger cold water events during their first EOF mode.

7.6 Highlights

As an overall, the main findings from this investigation highlighting this study's unique contributions included:

1) 2 combined EOF analysis were performed from: 1) 56 cold water events and 2) 49 upward velocity events to understand which of the 8 forcing variables (wind stress, wind stress curl, frictional velocity, sea surface height, minimum distance to current's core, eddy amplitude, geostrophic velocity and bottom stress) had the most influence on the Port Alfred upwelling events. The wind stress curl was identified as the most dominant upwelling driver for stronger cold water and upward velocity events during their 1st mode of a combined EOF of cold water events and upward velocity events.
2) The 1st EOF mode for stronger upwelling events identified a combination of upwelling favorable winds and meanders as the main upwelling drivers from both cold water and upward velocity events.
3) The 1st EOF mode of weaker cold water events identified the Agulhas Current as its main upwelling driver while the weaker upward velocity events identified the presence of meanders as its main upwelling driver.
4) During their 2nd EOF mode, stronger cold water events were explained by a combination of upwelling favorable winds and the Agulhas Current while the stronger upward velocity events were more likely to be explained by a combination of upwelling favorable winds and meanders.

Chapter 8: Conclusion and perspectives

8.0 Introduction

This study has been conducted to shed more light on the Port Alfred upwelling and its possible driving mechanisms. In this chapter, we present the key findings of each chapter, the limitations, research scope and future recommendations of this study.

8.1 Literature review

In chapter 2, we discussed a wide range of studies covering different types of upwelling, a review of the study area and possible hypotheses behind the Port Alfred upwelling. There were different mechanisms which could trigger upwelling in general, for instance wind driven upwelling occurred in the eastern boundary currents. Other mechanisms could also trigger upwelling, for instance shelf break upwelling on the inshore edge of western boundary currents. Other features such as islands, submarine canyons, coastal trapped waves and cyclonic eddies could also induce upwelling. We have also reviewed prior studies which highlighted the potential hypotheses of this upwelling:

- The northeasterly wind component could trigger offshore Ekman transport and surface divergence (Goschen et al. 2012).
- The Agulhas Current could induce upwelling due to the widening of the continental shelf due to the conservation of potential vorticity and the narrowing of its inertial jet (Gill and Schumann, 1982). An intensification of the Agulhas Current could also lead to stronger friction against the seafloor, inducing an onshore bottom Ekman transport leading to upwelling (Malan, 2013).
- Eddy induced upwelling due to Natal pulses, Durban eddies and shear-edge eddies has been explored (Goschen et al. 2015) and coastal trapped waves was also seen as a potential forcing mechanism (Malan, 2013).
- Lastly, a combination of various upwelling favourable mechanisms has also been suggested to drive the Port Alfred upwelling (Goschen et al. 2015; Leber et al. 2017).

8.2 Data and methods

Chapter 3 was focused on the different datasets which were used in this study. We have used 3 observational datasets (CARS09, WOA2018 and OSTIA) and 3 different grids of the CROCO model outputs, with daily outputs of varying spatial resolution (22.5km, 7.5km, 2.5km). We have eventually chosen the CROCO 1/36° grid (2.5km and 60 vertical levels) as it was the most appropriate grid to study this type of upwelling considering its horizontal and vertical resolution. We were able to explore different upwelling events as well as other mesoscale features from Jan 1993 to Dec 2014. We

also used several atmospheric forcing variables (such as wind stress, wind stress curl) which were calculated from the daily ERA-ECMWF's reanalysis dataset as surface forcing for the model.

8.3 Spatial and temporal characteristics of Port Alfred upwelling

Chapter 4 was focused on unravelling the spatial and temporal characteristics of the Port Alfred upwelling. To achieve this, the study delved into oceanographic properties such as temperature, salinity, and vertical velocity across different time scales. Additionally, two upwelling indices derived from sea surface temperature were employed to identify and characterize upwelling events, shedding light on their frequency and intensity. Furthermore, the investigation explored the intricate relationship between sea surface temperature and vertical velocity, aiming to discern underlying patterns. The final facet of this question was focused on the conditions during upwelling events, involving an in-depth examination of the mean state during selected upwelling episodes and a comprehensive analysis of four distinct case studies. Some of the main highlights of this chapter are:

- After assessing the upwelling through different spatial resolutions (22.5, 7.5 and 2.5 km spatial resolutions) of the temperature, salinity and vertical velocity, we noted that the 2.5km grid was the fittest grid to represent the signature of the upwelling.
- The 1/12° and 1/36° CROCO grids successfully captured the temperature signature of the upwelling during the mean state, with the 1/36° grid displaying a more pronounced presence of the current and upwelling, averaging 19°C in the upwelling region and 23°C in the core of the current.
- The CROCO grids recorded higher salinity compared to the observational datasets, particularly noticeable in the CARS09 and WOA2018 datasets, with the 1/36° CROCO grid registering a salinity of 35.3 PSU in the upwelling region.
- The vertical velocity signal exhibited significant noise at that depth in each CROCO simulation. While the 1/4° and 1/12° CROCO grids struggled to delineate changes in bathymetry at 100m and showed minimal variation in vertical velocity, the 1/36° CROCO grid was able to outline the seafloor on the continental shelf. Near Port Alfred, it depicted small pockets with a high variation of vertical velocity ranging between -50 and 50 m/day in the current region.
- We decomposed the sea surface temperature and the vertical velocity to filter the seasonal influence and noted a strong seasonal influence. The 1/36° CROCO grid was in agreement with the OSTIA dataset showing a range between 16°C to 22°C while the coarser resolution grid overestimated the sea surface temperature.
- There is a negative correlation of 0.2 between vertical velocity and sea surface temperature. After detrending and deseasonalizing the sea surface temperature's time series, 56 upwelling events were identified from the residuals of the sea surface temperature and 49 upwelling events were found from the residuals of the vertical velocity.

- A composite of the 56 upwelling events were explored and 4 individual case studies indicated different conditions of the temperature, salinity and vertical velocity.

8.4 Influence of atmospheric forcing mechanism

Chapter 5 revolved around the influence of atmospheric forcing on the Port Alfred upwelling. Here, the study meticulously examined several crucial factors, including alongshore wind stress, wind stress curl, wind direction, and frictional velocity. The investigation began with a thorough exploration of the roles played by Ekman transport and Ekman pumping within the Port Alfred upwelling zone, scrutinizing their effects at various temporal scales. Furthermore, the study sought to establish correlations between these atmospheric variables and sea surface temperature/vertical velocity, offering insights into the interplay between atmospheric conditions and upwelling dynamics. To gain a more nuanced understanding, the research extended its scope to encompass individual case studies and an overarching analysis of the upwelling state during upwelling events. Some of the main highlights of this study include:

- Upwelling during summer tends to be driven by offshore Ekman transport and divergence, while in winter, stronger southwesterlies are more likely to cause upwelling through vertical mixing.
- The presence of shear stress at the inshore front of the Agulhas Current results in a strong positive wind stress curl, leading to downwelling along the current's front and significant convergence of floating material.

8.5 Influence of oceanographic forcing mechanism

In chapter 6, we ventured into the influence of oceanographic forcing mechanisms on the Port Alfred upwelling. This entailed an in-depth investigation into the role of the Agulhas Current, cyclonic eddies, and coastal trapped waves on the upwelling dynamics, evaluated across different temporal scales. We investigated the 4 terms of the generalized Ekman pumping equation during its mean state i.e the planetary vorticity, wind stress curl, advection of momentum and the viscous flux. We assessed the geostrophic velocity, surface and bottom ocean velocities, bottom Ekman transport, and sea surface height. In parallel, the research explored the significance of meanders by employing oceanic data and specialized tracking methods like the LACCE algorithm and PY eddy tracker, all evaluated at different temporal scales. The minimum distance from the current’s core and the upwelling was computed from the LACCE algorithm. As for the PY eddy tracker algorithm, we computed the eddy radius, eddy amplitude and the eddy area. Additionally, the study probed into the potential influence of coastal trapped waves through the analysis of sea surface height data and the application of the LACCE algorithm, shedding light on their potential contribution to the upwelling processes. The main highlights of this chapter include:

- During the mean state, the momentum of advection drives significant upwelling, generating a vertical velocity of 4.22 m/day in the Port Alfred upwelling region. Viscous flux also contributes partially to the upwelling, with 0.5 m/day of vertical velocity.
- CROCO simulations focusing on Port Alfred show an average of 1.9 large meander events annually detected by the LACCE current tracker algorithm. The Py eddy tracker algorithm identifies slightly more events, averaging 2.2 based on eddy amplitude, 1.5 based on eddy area, and 1.3 based on eddy radius.
- Evaluation of various contributing oceanographic upwelling drivers in the Port Alfred upwelling region across different time scales indicates that the Agulhas Current primarily drives upwelling during the mean state. However, individual upwelling events can also be triggered by other oceanographic upwelling drivers such as cyclonic eddies and coastal trapped waves.

8.6 Most dominant forcing mechanism

In chapter 7, we aimed to identify the most dominant oceanographic and atmospheric variables during Port Alfred upwelling events. We employed a combined empirical orthogonal function (EOF) analysis, enabling a comprehensive assessment and comparison of various forcing mechanisms contributing to the upwelling phenomenon. The overarching goal was to pinpoint the primary driving force behind this dynamic upwelling process, ultimately providing valuable insights into the complex interactions and influential factors shaping the Port Alfred upwelling. Some of the main highlights of this chapter are:

- Wind stress curl emerged as the most influential factor for both stronger cold water events and upward velocity events during their first mode of a combined EOF analysis.
- The 1st EOF mode for stronger upwelling events identified a combination of upwelling favourable winds and meanders as the main upwelling drivers from both cold water and upward velocity events.
- The 1st EOF mode of weaker cold water events identified the Agulhas Current as its main upwelling driver while the weaker upward velocity events identified the presence of meanders as its main upwelling driver.
- During their 2nd EOF mode, stronger cold water events were explained by a combination of upwelling favourable winds and the Agulhas Current while the stronger upward velocity events were more likely to be explained by a combination of upwelling favourable winds and meanders.

8.7 Limitations of the study

A few limitations have been highlighted in this study. Since there was only a small number of hydrographic cruises conducted in the region, we chose to not rely on any *in situ* observations. As for

the remote sensing products, we required several ocean properties which could not be measured by satellites (e.g vertical velocity and bottom stress) and hence opted to use the variables from the simulations of the model. As for the numerical model, the spatial and vertical resolution were about 2.5 km and 60 vertical levels. But a higher resolution would improve the study as the upwelling cell was relatively small in size, sometimes ranging from 15 to 100km (Lutjeharms et al, 2000).

8.8 Recommendations

There is still a lot of work to be done in the Port Alfred region, for instance more hydrographic cruises could be conducted in this area. More variables could have been measured, for instance, turbulence could have also been explored to investigate the link between vertical mixing and the upwelling. Eddy kinetic energy and wave spectrum analysis could have also been computed to investigate the influence of cyclonic eddies. Since we found that Natal pulses events vary from 1.3 to 2.2 events per year, it was likely that small cyclonic eddies held a major influence on this upwelling and future studies could look at the difference between the influence of smaller and large meander events.

A longer time period could have allowed for more refined results. We could also assess if the Agulhas Current would weaken in the future due to climate change. The weakening or strengthening of the current would definitely influence the upwelling. As for the wind datasets, a higher resolution dataset would have improved the results of this study. In the case of the numerical model, the use of a grid of larger number of vertical levels and higher horizontal spatial resolution would greatly improve our understanding by being able to identify potential smaller features influencing the upwelling. For instance, there are many submarine canyons in this region, and it is also likely that upwelling is driven due to these canyons. Recently there has also been a need to address marine heat waves which occur in this region and this would often lead to harmful algal blooms causing fish mortality. Figure 8.1 shows the sea surface temperature and chlorophyll concentration during 7th March 2021 whereby high fish mortality was recorded on the beaches in Port Alfred region. A deeper analysis of this upwelling would contribute to better predictions of the harmful algal blooms.

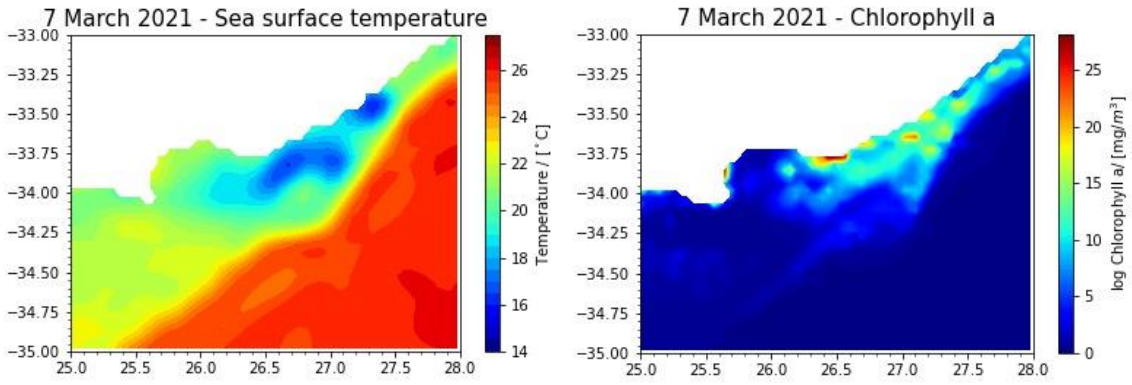

Figure 8.1: Harmful algal bloom causing a high fish mortality during March 2021 - NOAA/MODIS satellite images of sea surface temperature and chlorophyll concentration.

This study has been conducted to shed more light on the Port Alfred upwelling and its possible driving mechanisms. Currently there has still been an ongoing pressure to reach a target of protecting 30% of the coastline of South Africa by 2030. Upwelling zones are crucial in the ecosystem, and Port Alfred, being a semi-permanent upwelling throughout the year and allowing the conditions for primary productivity, would be a great fit to join the future list of MPAs in South Africa or to extend the Amathole MPA zone to Port Alfred region.

Bibliography

Bailey, D.F., Hermes, J., Penven, P., Bornman, T.G. and Goschen, W., 2022. An investigation of sea level and circulation response during a coastal trapped wave event on the Eastern Agulhas Bank, South Africa. Continental Shelf Research, 240, p.104698.

Bakun, A., 1973. Coastal upwelling indices, west coast of North America, 1946-71.

Bakun, A. 1975. Daily and weekly upwelling indices, west coast of North America, 1967–73. U.S. Department of Commerce, NOAA Technical Report, NMFS SSRF-693, 114 p.

Beal, L.M., 1997. Observations of the velocity structure of the Agulhas Current (Doctoral dissertation, University of Southampton).

Beal, L. M., De Ruijter, W. P. M., Biastoch, A., and Zahn, R. (2011). On the role of the Agulhas system in ocean circulation and climate. Nature, 472(7344):429–36.

Beckley LE. 1988. Spatial and temporal variability in sea tempera tures in Algoa Bay, South Africa. South African Journal of Science 84: 67–69

Bower, A., H. Rossby, and J. Lillibridge, 1985: The Gulf Stream— Barrier or blender? J. Phys. Oceanogr., 15, 24–32

Blanton, J. O., Atkinson, L. P., Pietrafesa, L. J., and Lee, T. N. (1981). The intrusion of Gulf Stream Water across the continental shelf due to topographically-induced upwelling. Deep Sea Research Part I: Oceanographic Research Papers, 28A(4):393–405.

Braby, L., Backeberg, B.C., Ansorge, I., Roberts, M.J., Krug, M. and Reason, C.J., 2016. Observed eddy dissipation in the Agulhas Current. Geophysical Research Letters, 43(15), pp.8143-8150.

Braby, L., Backeberg, B., Krug, M. and Reason, C., 2020. Quantifying the impact of wind-current feedback on mesoscale variability in forced simulation experiments of the Agulhas Current using an eddy-tracking algorithm. Journal of Geophysical Research: Oceans, 125(1), p.e2019JC015365.

Brandini, F., 1990: Hydrography and characteristics of the phyto plankton in shelf and oceanic waters off southeastern Brazil during winter (July/August 1982) and summer (February/March 1984). Hydrobiologia, 196, 111–148

Campos, E. J. D., Velhote, D., and da Silveira, I. C. A. (2000). Shelf break upwelling driven by Brazil Current cyclonic. Geophysical Research Letters, 27(6):751–754.

Capet, A., E. Mason, V. Rossi, C. Troupin, Y. Faugère, M.-I. Pujol, and A. Pascual (2014), Implications of refined altimetry on estimates of mesoscale activity and eddy-driven offshore transport in the eastern boundary upwelling systems, Geophys. Res. Lett., 41, 7602–7610

Castelão, R.M., and J.A. Barth. 2006. Upwelling around Cabo Frio, Brazil: The importance of wind stress curl. Geophysical Research Letters 33: L03602.

Castro, B. D., and L. D. Miranda, 1998: Physical oceanography of the western Atlantic continental shelf located between 48N and 348S. The Global Coastal Ocean: Regional Studies and Syntheses, A. R. Robinson and K. H. Brink, Eds., The Sea— Ideas and Observations on Progress in the Study of the Seas, Vol. 11, John Wiley and Sons, 209–251.

Chaigneau, A., Gizolme A. , and Grados C. , 2008: Mesoscale eddies off Peru in altimeter records: Identification algorithms and eddy spatio-temporal patterns. Prog. Oceanogr., 79, 106–119

Chapman, C.C., Lea, M.A., Meyer, A., Sall´ee, J.B., Hindell, M., 2020. Defining Southern Ocean fronts and their influence on biological and physical processes in a changing climate. Nature Climate Change 1–11.

Chavez, F.P., and M. Messié. 2009. A comparison of eastern boundary upwelling ecosystems. Progress in Oceanography 83(1–4): 80–96.

Chelton, D. B., M. G. Schlax, and R. M. Samelson, 2007: Summertime coupling between sea surface temperature and wind stress in the California Current System. J. Phys. Oceanogr., 37, 495–517

Churchill, J. H., Cornillon, P. C., and Milkowski, G. W. (1986). A Cyclonic Eddy and Shelf-Slope Water Exchange Associated With a Gulf Stream Warm-Core Ring. Journal of Geophysical Research, 91(C8):9615–9623.

Clemente-Colón, P., 2001, July. Evolution of upwelling-associated biological features in the Middle Atlantic Bight as captured by SAR, SST, and ocean color sensors. In IGARSS 2001. Scanning the Present and Resolving the Future. Proceedings. IEEE 2001 International Geoscience and Remote Sensing Symposium (Cat. No. 01CH37217) (Vol. 6, pp. 2616-2618). IEEE.

Cuypers, Y., Le Vaillant, X., Bouruet-Aubertot, P., Vialard, J. and Mcphaden, M.J., 2013. Tropical storm-induced near-inertial internal waves during the Cirene experiment: Energy fluxes and impact on vertical mixing. Journal of Geophysical Research: Oceans, 118(1), pp.358-380.

de Ruijter, W. P. M. D., Biastoch, A., Drijfhout, S. S., Lutjeharms, J. R. E., Matano, R. P., Pichevin, T., Leeu, V., and Weijer, W. (1999a). Indian-Atlantic interocean Dynamics, estimation and impact ring shedding. Journal of Geophysical Research, 104:20885–20910.

de Ruijter, W. P. M. D., van Leeuwen, P. J., and Lutjeharms, J. (1999b). Generation and Evolution of Natal Pulses : Solitary Meanders in the Agulhas Current. Journal of physical oceanography, 29:3043–3055.

Debreu, L. and Blayo, E. (2008). Two-way embedding algorithms: a review. Ocean Dynamics, 58(5-6):415–428.

Debreu, L., Marchesiello, P., Penven, P., and Cambon, G. (2012). Two-way nesting in split-explicit ocean models: algorithms, implementation and validation. Ocean Modell., 49:1–21.

Dee, D., and Coauthors, 2011: The ERA-Interim reanalysis: Configuration and performance of the data assimilation system. Quarterly Journal of the royal meteorological society, 137 (656), 553–597

Demarq, H. & Faure, V. (2000), 'Coastal upwelling and associated retention indices derived from satellite sst. application to octopus vulgaris recruitment', Oceanologica Acta 23(4), 391–408

Djakouré, S., Penven, P., Bourlès, B., Koné, V. and Veitch, J., 2017. Respective roles of the Guinea Current and local winds on the coastal upwelling in the northern Gulf of Guinea. Journal of Physical Oceanography, 47(6), pp.1367-1387.

Doglioli, A. M., Blanke B. , Speich S. , and Lapeyre G. , 2007: Tracking coherent structures in a regional ocean model with wavelet analysis: Application to cape basin eddies. J. Geophys. Res., 112, C05043

Doty, M.S., and M. Oguri. 1956. The island mass effect. International Council for the Exploration of the Sea 22: 33–37.

Ducet, N., P.-Y. Le Traon, and G. Reverdin (2000), Global high-resolution mapping of ocean circulation from TOPEX/Poseidon and ERS-1 and −2, J. Geophys. Res., 105(C8), 19,477–19,498.

Durski, S., S. Glenn, and D. Haidvogel, 2004: Vertical mixing schemes in the coastal ocean: Comparison of the level 2.5 Mellor-Yamada scheme with an enhanced version of the K profile parameterization. Journal of Geophysical Research: Oceans, 109 (C1).

Ekman, V.W. 1905. On the influence of the Earth's rotation on ocean currents. Arkiv foer Matematik Astronomi och Fysik 2: 11.

Fairall, C., E. Bradley, D. Rogers, J. Edson, and G. Young, 1996: Bulk parameterization of air-sea fluxes for tropical ocean-global atmosphere coupled-ocean atmosphere response experiment. Journal of Geophysical Research: Oceans, 101 (C2), 3747–3764.

Feng, C., Li, L. and Sadeghpour, A., 2020. A comparison of residual diagnosis tools for diagnosing regression models for count data. BMC Medical Research Methodology, 20(1), pp.1-21.

Ferry, N., and Coauthors, 2012: Glorys2v1 global ocean reanalysis of the altimetric era (1992–2009) at mesoscale. Mercator Ocean–Quaterly Newsletter, 44.

Flierl, G., and C. Davis, 1993: Biological effects of Gulf Stream meandering. J. Mar. Res., 51, 529–560

Garzoli, S.L., 1993. Geostrophic velocity and transport variability in the Brazil-Malvinas Confluence. Deep Sea Research Part I: Oceanographic Research Papers, 40(7), pp.1379-1403.

Gill, A. E. and Schumann, E. (1979). Topographically Induced Changes in the Structure of an Inertial Coastal Jet: Application to the Agulhas Current. Journal of physical oceanography, 9:975–991.

Gill, A. E., 1982: Atmosphere–Ocean Dynamics. Academic Press, 662 pp.

Gordon, A. L. (1985). Indian-Atlantic Transfer of Thermocline Water at the Agulhas Retroflection. Science, 227(4690):1030–1033.

Gordon, R. L. (1996). Acoustic Doppler Current Profiler Principles of Operation A Practical Primer.

Goschen, W. S., Schuman, E. H., Bernard, K. S., Bailey, S. E., and Deyzel, S. H. P. (2012). Upwelling and ocean structures off Algoa Bay and the south-east coast of South Africa. African Journal of Marine Science, 34:4(April 2013):37–41.

Goschen, W.S., Bornman, T.G., Deyzel, S.H.P. and Schumann, E.H., 2015. Coastal upwelling on the far eastern Agulhas Bank associated with large meanders in the Agulhas Current. Continental Shelf Research, 101, pp.34-46.

Haidvogel, D., and A. Beckmann, 1999: Numerical ocean circulation modeling. World Scientific

Hedstrom, K. (1997), User's Manual for an S-Coordinate Primitive Equation Ocean Circulation Model SCRUM Version 3.0, Institute of Marine and Coastal Sciences Rutgers University.

Heywood, K.J., E.D. Barton, and J.H. Simpson. 1990. The effects of flow disturbance by an oceanic island. Journal of Marine Research 48: 55–73.

Hickey, B.M. 1997. The response of a steep-sided, narrow canyon to time-variable wind forcing. Journal of Physical Oceanography 27: 697–726.

Hutchings, L., Beckley, L.E., Griffiths, M.H., Roberts, M.J., Sundby, S. and Van der Lingen, C., 2002. Spawning on the edge: spawning grounds and nursery areas around the southern African coastline. Marine and Freshwater Research, 53(2), pp.307-318.

Hutchinson, K., 2018. Seasonality of the Agulhas Current with respect to near-and far-field winds (Doctoral dissertation, University of Cape Town).

Hunt, J.C., Wray, A.A. and Moin, P., 1988. Eddies, streams, and convergence zones in turbulent flows. Studying turbulence using numerical simulation databases, 2. Proceedings of the 1988 summer program.

Jackson, J. M., Rainville, L., Roberts, M. J., McQuaid, C. D., and Lutjeharms, J. R. (2012). Mesoscale bio-physical interactions between the Agulhas Current and the Agulhas Bank, South Africa. Continental Shelf Research, 49:10–24.

Jouanno, J., Marin, F., Du Penhoat, Y., Molines, J.M. and Sheinbaum, J., 2011. Seasonal modes of surface cooling in the Gulf of Guinea. Journal of Physical Oceanography, 41(7), pp.1408-1416.

Jung, J. and Cho, Y.K., 2020. Persistence of coastal upwelling after a plunge in upwelling-favourable wind. Scientific reports, 10(1), p.11938.

Kämpf, J. 2012. Lee effects of localized upwelling in a shelf-break canyon. Continental Shelf Research 42: 78–88.

Kämpf, J., M. Doubell, D. Griffin, R.L. Matthews, and T.M. Ward. 2004. Evidence of a large seasonal coastal upwelling system along the southern shelf of Australia. Geophysical Research Letters 31: L09310.

Kämpf, J. and Chapman, P., 2016. Upwelling systems of the world (pp. 31-42). Springer International Publishing Switzerland.

Klinger, B.A., Huang, B., Kirtman, B., Schopf, P. and Wang, J., 2006. Monthly climatologies of oceanic friction velocity cubed. Journal of climate, 19(21), pp.5700-5708.

Kraus, E.B., and J.A. Businger. 1994. Atmosphere-Ocean Interaction. Oxford University Press, 362 pp.

Krug, M. and Tournadre, J. (2012). Satellite observations of an annual cycle in the Agulhas Current. Geophysical Research Letters, 39(15)

Krug, M., Tournadre, J. and Dufois, F., 2014. Interactions between the Agulhas Current and the eastern margin of the Agulhas Bank. Continental Shelf Research, 81, pp.67-79.

Kutzbach, J. E. 1967. Empirical eigenvectors of sea level pressure, surface temperature and precipitation complexes over North America. J. Appl. Meteor. 6: 791-802.

Kuypers, M.M.M., G. Lavik, D. Woebken, M. Schmid, B.M. Fuchs, R. Amann, B.B. Jorgensen, and M.S.M. Jetten. 2005. Massive nitrogen loss from the Benguela upwelling system through anaerobic ammonium oxidation. Proceedings of the National Academy of Sciences 102: 6478–6483.

Large, W., McWilliams, J., and Doney, S. (1994). Oceanic vertical mixing: A review and a model with a nonlocal boundary layer parameterization. Rev. Geophys., 32(4):363–403.

Largier, J. L. and Swart, V. P. (1987). East-west variation in thermocline breakdown on the Agulhas Bank. South African Journal Of Marine Science, 5(1):263–272.

Leber, G.M., Beal, L.M. and Elipot, S., 2017. Wind and current forcing combine to drive strong upwelling in the Agulhas Current. Journal of Physical Oceanography, 47(1), pp.123-134.

Lemarié, F., Kurian, J., Shchepetkin, A. F., Jeroen Molemaker, M., Colas, F., and McWilliams, J. C. (2012). Are there inescapable issues prohibiting the use of terrain-following coordinates in climate models? Ocean Modell., 42:57–79.

Lin, C., Fung, J.C., Ren, C., Ng, E.Y., Li, Y., He, Y., Leung, K.K., Ning, Z. and Lau, A.K., 2023. Horizontal flux of ozone in the planetary boundary layer in Hong Kong using wind LiDAR measurements. Atmospheric Environment, 312, p.120046.

Lutjeharms, J. R. E., Catzel, R., and Valentine, H. (1989). Eddies and other boundary phenomena of the Agulhas Current. Continental Shelf Research, 9:597–616.

Lutjeharms, J. R. E. and Roberts, H. (1988). The Natal Pulse: An Extreme Transient on the Agulhas Current. Journal of Geophysical Research, 93:631–645.

Lutjeharms, J. (1993). On some similarities between the oceanic circulations off Southern Africa and off Taiwan. South African Journal of Science, 89:367–371.

Lutjeharms, J. R. E. and Machu, E. (2000a). An upwelling cell inshore of the East Madagascar Current. Deep-Sea Research, 47:2405–2411.

Lutjeharms, J., Cooper, J., and Roberts, M. (2000b). Upwelling at the inshore edge of the Agulhas Current. Continental Shelf Research, 20(7):737–761.

Lutjeharms, J. (2006). The Agulhas Current. Springer.

Malan, N., 2013. Driving mechanisms of the Port Alfred upwelling cell inshore of the Agulhas Current (Master's thesis, University of Cape Town).

Malan, N.C., 2017. The Impact Of Agulhas Current Dynamics On Shelf Waters: A Modelling Approach. University of Cape Town.

Marchesiello, P., J. McWilliams, and A. Shchepetkin, 2001: Open boundary conditions for long-term integration of regional oceanic models. Ocean modelling, 3 (1-2), 1–20

Mason, E., Pascual, A., Gaube, P., Ruiz, S., Pelegrí, J.L. and Delepoulle, A., 2017. Subregional characterization of mesoscale eddies across the B razil-M alvinas C onfluence. Journal of Geophysical Research: Oceans, 122(4), pp.3329-3357.

McCalpin, J., 1994: A comparison of second-order and fourth-order pressure gradient algorithms in a σ-co-ordinate ocean model. International Journal for Numerical Methods in Fluids, 18 (4), 361–383.

McPhaden, M.J., Zhang, X., Hendon, H.H. and Wheeler, M.C., 2006. Large scale dynamics and MJO forcing of ENSO variability. Geophysical research letters, 33(16).

Messié, M., J. Ledesma, D.D. Kolber, R.P. Michisaki, D.G. Foley, and F.P. Chavez. 2009. Potential new production estimates in four eastern boundary upwelling systems. Progress in Oceanography 83(1–4): 151–158.

Nencioli, F., Dong C. , Dickey T. D. , Washburn L. , and McWilliams J. C. , 2010: A vector geometry–based eddy detection algorithm and its application to a high-resolution numerical model product and high-frequency radar surface velocities in the Southern California Bight. J. Atmos. Oceanic Technol., 27, 564–579

Oke, P. and Middleton, J. (2000). Topographically induced upwelling off eastern Australia. Journal of Physical Oceanography, pages 512–531.

Palma, E. D. and Matano, R. P. (2009). Disentangling the upwelling mechanisms of the South Brazil Bight. Continental Shelf Research, 29(11-12):1525–1534.

Parrish, R.H., F.B. Schwing, and P. Mendelsson. 2000. Mid latitude wind stress: The energy source for climatic shifts in the North Pacific Ocean. Fishery Oceanography 9: 224–238.

Pickett, M. H., and J. D. Paduan, 2003: Ekman transport and pumping in the California Current based on the U.S. Navy's high-resolution atmospheric model (COAMPS). J. Geophys. Res., 108, 3327

Pivan, X., Krug, M. and Herbette, S., 2016. Observations of the vertical and temporal evolution of a N atal P ulse along the E astern A gulhas B ank. Journal of Geophysical Research: Oceans, 121(9), pp.7108-7122.

Penven, P., Echevin V. , Pasapera J. , Colas F. , and Tam J. , 2005: Average circulation, seasonal cycle, and mesoscale dynamics of the Peru Current System: A modeling approach. J. Geophys. Res., 110, C1002

Penven, P., P. Marchesiello, L. Debreu, and J. Lefèvre, 2008: Software tools for pre-and post-processing of oceanic regional simulations. Environmental Modelling & Software, 23 (5), 660–662.

Pond, S., and G.L. Pickard. 1983. Introductory Dynamical Oceanography, 2nd ed. Oxford: Pergamon Press. 329 pp.

Qi, H., De Szoeke, R.A., Paulson, C.A. and Eriksen, C.C., 1995. The structure of near-inertial waves during ocean storms. Journal of Physical Oceanography, 25(11), pp.2853-2871.

Ramanantsoa, J.D., Krug, M., Penven, P., Rouault, M. and Gula, J., 2018. Coastal upwelling south of Madagascar: Temporal and spatial variability. Journal of Marine Systems, 178, pp.29-37.

Renault, L., J. McWilliams, and P. Penven, 2017: Modulation of the Agulhas Current Retroflection and Leakage by Oceanic Current Interaction with the Atmosphere in Coupled Simulations. Journal of Physical Oceanography, 47 (8), 2077–2100.

Roberts, M. (2005). Chokka squid (Loliga vulgaris reynaudi) abundance linked to changes in South Africa's Agulhas Bank ecosystem during spawning and the early life cycle. ICES Journal of Marine Science, 55.

Roberts, M. J. (2010). Coastal currents and temperatures along the eastern region of Algoa Bay, South Africa, with implications for transport and shelf-bay water exchange. African Journal of Marine Science, 32(1):145–161.

Roberts, M. J., van der Lingen, C. D., Whittle, C., and van den Berg, M. (2010). Shelf currents, lee-trapped and transient eddies on the inshore boundary of the Agulhas Current, South Africa: their relevance to the KwaZulu-Natal sardine run. African Journal of Marine Science, 32(2):423–447.

Rouault, M., Lee-Thorp, A., and Lutjeharms, J. (2000). The Atmospheric Boundary Layer above the Agulhas Current during Alongcurrent Winds. Journal of Physical Oceanography, 30:40–50.

Rouault, M., Pohl, B. and Penven, P., 2010. Coastal oceanic climate change and variability from 1982 to 2009 around South Africa. African Journal of Marine Science, 32(2), pp.237-246.

Rouault, M. J. and Penven, P. (2011). New perspectives on Natal Pulses from satellite observations. Journal of Geophysical Research, 116(C7):1–14.

Roughan, M., Oke, P.R. and Middleton, J.H., 2003. A modelling study of the climatological current field and the trajectories of upwelled particles in the East Australian Current. Journal of Physical Oceanography, 33(12), pp.2551-2564.

Roughan, M. and Middleton, J.H., 2002. A comparison of observed upwelling mechanisms off the east coast of Australia. Continental Shelf Research, 22(17), pp.2551-2572.

Roughan, M. and Middleton, J.H., 2004. On the East Australian Current: variability, encroachment, and upwelling. Journal of Geophysical Research: Oceans, 109(C7).

Roy, C., van der Lingen, C., Coetzee, J., and Lutjeharms, J. (2007). Abrupt environmental shift associated with changes in the distribution of Cape anchovy Engraulis encrasicolus spawners in the southern Benguela. African Journal of Marine Science, 29(3):309–319.

Russo, C.S., Lamont, T. and Krug, M., 2021. Spatial and temporal variability of the Agulhas Retroflection: Observations from a new objective detection method. Remote Sensing of Environment, 253, p.112239.

Santos, A.M.P., Kazmin, A.S., Peliz, A. Decadal changes in the Canary upwelling system as revealed by satellite observations their impact on productivity. Journal of Marine Research, 2005, 63: 359–379.

Shchepetkin, A. and McWilliams, J. (1998). Quasi-monotone advection schemes based on explicit locally adaptive dissipation. Mon. Wea. Rev., 126(6):1541–1580.

Schumann, E.H., Perrins, L.A. and Hunter, I.T., 1982. Upwelling along the south coast of the Cape Province, South Africa. South African Journal of Science, 78(6), pp.238-242.

Schumann, E. and Brink, K. (1990). Coastal-trapped waves off the coast of South Africa: generation, propagation and current structures. Journal of physical oceanography, 20:1206–1218.

Schumann, E.H., 1999. Wind-driven mixed layer and coastal upwelling processes off the south coast of South Africa. Journal of Marine Research, 57(4), pp.671-691.

Shaffer, G., O. Pizarro, L. Djurfeldt, S. Salinas, and J. Rutllant. 1997. Circulation and low-frequency variability near the Chilean coast: Remotely forced fluctuations during the 1991–92 El Niño. Journal of Physical Oceanography 27: 217–230.

Smith, R. L., 1995: The physical processes of coastal ocean up welling systems. Environ. Sci. Res. Rep. ES, 18, 39–64.

Speich, S., Lutjeharms, J. R. E., Penven, P., and Blanke, B. (2006). Role of bathymetry in Agulhas Current configuration and behaviour. Geophysical Research Lettters, 33(23):L23611.

Speth, P., Detlefsen, H., Sierts, H. Meteorological influences on upwelling off northwest Africa. Ocean Dynamics, 1978, 31: 95–104.

Soufflet, Y., P. Marchesiello, F. Lemarié, J. Jouanno, X. Capet, L. Debreu, and R. Benshila, 2016: On effective resolution in ocean models. Ocean Modelling, 98, 36–50.

Sverdrup, H.U., Johnson, M.W. and Fleming, R.H., 1942. The Oceans: Their physics, chemistry, and general biology (Vol. 1087, No. 8). New York: Prentice-Hall.

Swart, V. P. and Largier, J. L. (1987). Thermal structure of Agulhas Bank water. South African Journal Of Marine Science, 5:243–253

Taljaard, J.J., 1953. The mean circulation in the lower troposphere over southern Africa. South African Geographical Journal, 35(1), pp.33-45.

Tedesco, P., J. Gula, C. Ménesguen, P. Penven, and M. Krug, 2019: Generation of submesoscale frontal eddies in the Agulhas Current. Journal of Geophysical Research: Oceans, 124 (11), 7606–7625.

Thompson, R.O.R.Y., and T.J. Golding. 1981. Tidally induced 'upwelling' by the Great Barrier Reef. Journal of Geophysical Research 86: 6517–6521.

Van der Lee, E.M. and Umlauf, L., 2011. Internal wave mixing in the Baltic Sea: Near-inertial waves in the absence of tides. Journal of Geophysical Research: Oceans, 116(C10).

Veitch, J. A. (2009), 'Equilibrium dynamics of the Benguela system: a numerical modelling approach'.

Weatherall, P., and Coauthors, 2015: A new digital bathymetric model of the world's oceans. Earth and Space Science, 2 (8), 331–345.

Wolanski, E., and W.M. Hamner. 1988. Topographically controlled fronts in the ocean and their biological influence. Science 241: 177–181.

Wooster, W.S., Bakum, A., McLain, D.R. The seasonal upwelling cycle along the eastern boundary of the North Atlantic. Journal of Marine Research, 1976, 34: 131–141.

Yi, X., Hünicke, B., Tim, N. and Zorita, E., 2018. The relationship between Arabian Sea upwelling and Indian Monsoon revisited in a high resolution ocean simulation. Climate dynamics, 50, pp.201-213.

Zhang, Y. and Tian, J., 2014. Enhanced turbulent mixing induced by strong wind on the South China Sea shelf. Ocean Dynamics, 64(6), pp.781-796.

Sheveenah Sunnassee Taukoor - Thèse de Doctorat de l'Université de Bretagne Occidentale

Etude de modélisation de l'upwelling de Port Alfred au bord côtier du courant des Aiguilles

L'upwelling de Port Alfred, situé sur le plateau sud-est africain, se trouve à la limite côtière d'un courant bord ouest, le courant des Aiguilles. Cette étude aborde les mécanismes de forçage atmosphérique et océanographique responsables de ces événements d'upwelling à travers les simulations quotidiennes d'un modèle CROCO d'une résolution spatiale horizontale d'environ 2,5 km de 1993 à 2014. Nous avons testé plusieurs indices d'upwelling côtiers et nous avons identifié 56 événements d'upwelling du résiduels de la température de surface de mer et 49 événements d'upwelling à travers la décomposition de la vitesse verticale. Pour évaluer l'influence du vent, nous avons mesuré la tension du vent, le rotationnel de la tension de vent et la vitesse de friction à différentes échelles temporelles. Notre analyse a montré que les remontées d'eau au cours de l'été étaient principalement provoquées par les vents du nord-est emettant un transport et une divergence d'Ekman au large. En revanche, des vents plus forts du sud-ouest en hiver pourraient provoquer un mélange vertical. Pour déterminer le mécanisme d'upwelling de Port Alfred pendant l'état moyen, nous avons calculé les termes de l'équation de pompage d'Ekman généralisée et avons constaté que l'advection de momentum contribuait à 4,22 m/jour de vitesse verticale tandis que le terme de friction contribuait partiellement à 0,5 m/jour de vitesse verticale. Pour déterminer si l'upwelling était influencé par des caractéristiques océanographiques à méso-échelle (courant des Aiguilles, Natal pulses, tourbillons de Durban, tourbillons de cisaillement et ondes côtières de Kelvin), nous avons mesuré la hauteur de la surface de la mer, la vitesse géostrophique, le transport d'Ekman au fond et identifié 1,9 événements de méandres par an de l'algorithme de detection de courant LACCE, 2,2 basé sur l'amplitude des tourbillons, 1,5 basé sur la zone de tourbillon et 1,3 basé sur le rayon de tourbillon de l'algorithme de detection de tourbillons PY. Nous avons constaté que le courant des Aiguilles était le principal moteur de la remontée d'eau au cours de l'état moyen, mais que certains événements individuels étaient influencés par des tourbillons cycloniques et des ondes côtières de Kelvin.

Enfin, nous avons effectué 2 analyses de méthode décomposition orthogonale aux valeurs propres à partir de (1) la température de surface de mer et (2) la vitesse verticale et nous avons identifié la divergence de surface comme le moteur de remontée d'eau le plus dominant dans les deux EOF combinés. Cependant, le transport d'Ekman, la présence de tourbillons cycloniques, le courant des Aiguilles et les ondes côtières de Kelvin ont également contribué à des événements d'upwelling plus forts et plus faibles. Dans l'ensemble, cette étude confirme que le courant des Aiguilles reste le principal moteur de la remontée d'eau pendant l'état moyen, mais à travers le prisme d'une échelle temporelle différente (études de cas individuelles et EOF combinés), il est probable qu'une combinaison d'un ou plusieurs mécanismes de forçage (vents favorables, tourbillons cycloniques, courant des Aiguilles, ondes côtières de Kelvin) déclencheront un événement d'upwelling. Approfondir sur ce sujet et ses principaux moteurs permettra aux océanographes de concentrer davantage leur attention sur cet upwelling à l'avenir, ce qui pourrait inciter aux politiciens à considérer la région d'upwelling de Port Alfred comme une future zone marine protégée.

Mots-clés : Port Alfred, courant des Aiguilles, upwelling, tourbillons cycloniques, Natal pulses, CROCO

Modelling study of Port Alfred upwelling at the inshore edge of Agulhas current

Port Alfred upwelling, located on the southeast African shelf, lies on the inshore edge of a western boundary current, the Agulhas Current. This study addressed the atmospheric and oceanographic forcing mechanisms responsible for these upwelling events through the daily simulations of a CROCO model of a horizontal spatial resolution of ~2.5km from 1993 to 2014. We tested several coastal upwelling indices and we identified 56 upwelling events from the residuals of sea surface temperature and 49 upwelling events through the decomposition of the vertical velocity. To assess the influence of the wind, we measured the alongshore wind stress, wind stress curl and frictional velocity at different temporal scales. Our analysis showed that upwelling during summer was primarily driven by northeasterlies inducing offshore Ekman transport and divergence. In contrast, stronger southwesterlies during winter could cause vertical mixing. To determine the Port Alfred upwelling's driving mechanism during the mean state, we computed the terms of the generalized Ekman pumping equation and found that the advection of momentum contributed to 4.22 m/day of vertical velocity while the viscous flux term contributed partially to 0.5 m/day of vertical velocity. To determine whether the upwelling was driven by oceanographic mesoscale features (Agulhas current, Natal pulses, Durban eddies, shear edge eddies and coastal trapped waves), we measured the sea surface height, geostrophic velocity, bottom Ekman transport and identified 1.9 large meander events annually from the LACCE current tracker algorithm, 2.2 based on eddy amplitude, 1.5 based on eddy area, and 1.3 based on eddy radius from the PY eddy tracker algorithm. We found that the Agulhas current was the primary upwelling driver during the mean state, but some individual upwelling events were influenced by cyclonic eddies and coastal trapped waves.

Finally, we conducted 2 combined Empirical Orthogonal Function analysis from (1) sea surface temperature and (2) vertical velocity and identified surface divergence as the most dominant upwelling driver in both combined EOFs while offshore Ekman, the presence of cyclonic eddies, the Agulhas current and coastal trapped waves also counted as contributing factors in stronger and weaker upwelling events. As an overall this study confirms that the Agulhas current remains the primary upwelling driver during the mean state but through the lens of a different temporal scale (individual case studies and combined EOFs), it is likely that a combination of one or more forcing mechanisms (upwelling favorable winds, cyclonic eddy, Agulhas current, coastal trapped waves) will trigger an upwelling event. Shedding more light on this topic and its main drivers allows oceanographers to focus more attention on this upwelling in the future and this could reinforce policymakers to consider Port Alfred upwelling region as a future Marine Protected Area.

Keywords : Port Alfred,Agulhas current, upwelling, cyclonic eddy, Natal pulses, CROCO